

DIFFUSION ASSISTED SYNTHESIS OF METAL NANOTUBES

Von der Fakultät Chemie der Universität Stuttgart
zur Erlangung der Würde eines

Doktors der Naturwissenschaft

(Dr. rer. nat.) genehmigte Abhandlung

Vorgelegt von

Semanur Baylan

aus Kelkit, Türkei

Hauptberichter: Prof. Dr. Guido Schmitz

Mitberichter: Prof. Dr. Eugen Rabkin

Prüfungsvorsitzender: Prof. Dr. Peer Fischer

Tag der Einreichung: 20.12.2016

Tag der mündliche Prüfung: 09.02.2017

Max-Planck-Institut für Intelligente Systeme
Stuttgart
2017

Erklärung über die Eigensändigkeit der Dissertation

Ich versichere, dass ich die vorliegende Arbeit mit dem Titel ' Diffusion assisted synthesis of metal nanotubes' selbständig verfasst und keine anderen als die angegebenen Quellen und Hilfsmittel benutzt habe; aus fremden Quellen entnommene Passagen und Gedanken sind als solche kenntlich gemacht.

Declaration of Authorship

I hereby certify that the dissertation entitled ' Diffusion assisted synthesis of metal nanotubes' is entirely my own work except where otherwise indicated. Passages and ideas from other sources have been clearly indicated.

Name/Name: Semanur Baylan

Unterschrift/Signed:

Datum/Date: 20.12.2016

To my family

CONTENT

ZUSAMMENFASSUNG	i
ABSTRACT	iii
<u>1 INTRODUCTION</u>	<u>1</u>
<u>2 THEORETICAL BACKGROUND</u>	<u>5</u>
2.1 PRINCIPLES OF THIN FILM GROWTH	5
2.1.1 VOLMER-WEBER (ISLAND) GROWTH	6
2.1.2 FRANK-VAN DER MERWE (LAYER) GROWTH	7
2.1.3 STRANSKI-KRASTANOV GROWTH	7
2.2 EPITAXIAL GROWTH AND CRITICAL THICKNESS	9
2.3 WHISKER GROWTH	11
2.4 INTERDIFFUSION AND KIRKENDALL EFFECT	16
<u>3 EXPERIMENTAL STUDY</u>	<u>21</u>
3.1 PHYSICAL VAPOR DEPOSITION TECHNIQUES	21
3.1.1 MAGNETRON SPUTTERING PVD	21
3.1.1.1 Sample Preparation by Magnetron Sputtering PVD	23
3.1.2 MOLECULAR BEAM EPITAXY	24
3.1.2.1 Fabrication of Core-Shell Nanowhiskers by MBE	26
3.1.2.1.1 Fabrication of Ag and Cu Nanowhiskers by MBE	26
3.1.2.1.2 Fabrication of Ag-Au, Ag-Pd, Ag-Co and Cu-Ni Core-Shell Nanowhiskers by MBE	29
3.2 FABRICATION OF METAL NANOTUBES	30
3.3 KINETIC STUDY AND THE MODEL	30
3.4 CHARACTERIZATION TECHNIQUES	30
3.4.1 CHARACTERIZATION OF THE SAMPLES BY SCANNING ELECTRON MICROSCOPE	30
3.4.2 CHARACTERIZATION OF THE SAMPLES BY TRANSMISSION ELECTRON MICROSCOPE	32
<u>4 RESULTS AND DISCUSSION</u>	<u>37</u>
4.1 CHARACTERIZATION OF AG-AU CORE-SHELL NANOWHISKERS	37
4.2 CHARACTERIZATION OF AU NANOTUBES	41
4.3 KINETIC STUDY AND THE DIFFUSION MODEL	53
4.4 CHARACTERIZATION OF AG-CO AND AG- PD NANOWHISKERS	61
4.5 CHARACTERIZATION OF CO AND PD NANOTUBES	69

4.6	CHARACTERIZATION OF CU-NI CORE-SHELL NANOWHISKERS	73
5	CONCLUSIONS	77
	REFERENCES	79
	ABBREVIATION AND SYMBOLS	85
	INDEX OF FIGURES	89
	ACKNOWLEDGEMENTS	93
	Curriculum Vitae	95

ZUSAMMENFASSUNG

Hohle metallische Nanostrukturen erwecken großes Interesse, sowohl aufgrund ihrer einzigartigen plasmonischen, katalytischen oder magnetischen Eigenschaften, als auch durch ihren Einsatz im Bereich der Nanotechnologie. Verschiedenste Methoden wurden eingesetzt um Nanostrukturen herzustellen, meist basierend auf dem s.g. Templat-Ansatz. Jedoch resultieren daraus oft polykristalline Nanostrukturen mit einer hohen Konzentration von Verunreinigungen und Defekten. Es ist schwierig den Vorgang der Porenbildung und deren Wachstum zu kontrollieren, auch ist ihre Größe und die Form durch das Templat deutlich eingeschränkt. Deshalb ist es wichtig solche Strukturen herzustellen.

In dieser Arbeit stellen wir eine neue Syntheseroute vor, um perfekte einkristalline, defektfreie und freistehende metallische Nanoröhrchen (englisch „Nanotube“, NT) ausgehend von metallischen Nanowhiskern (NW) herzustellen. Dabei dienen die NW als Matrize und werden nach Beschichten durch Korngrenzendiffusion aufgelöst.

Es wurden einkristalline Ag und Cu NW auf kohlebeschichteten Si/SiO₂/Si₃N₄ Substraten bei 650°C mit Molekularstrahepitaxie (Durchmesser:100-150 nm und Längen: 4-30 µm) synthetisiert. Verschiedene Materialien (Au, Pd, Co) wurden als Hülle auf den Ag NW bei Raumtemperatur aufgewachsen. Auf den Cu NW wurde dagegen Ni wurde als Hülle abgeschieden. Auf den Ag NW wuchsen die Materialien (Au, Pd, Co) als einkristalline heteroepitaktische Lagen auf. Auch das Ni bildete eine einkristalline Hülle auf den Cu NW. Im Gegensatz dazu entwickelten die Materialien polykristalline Filme auf dem Substrat. Die Nanoröhrchen wurden durch auslagern dieser Kern-Hüllen Komposite bei Temperaturen unterhalb 200°C für Ag-Pd und Ag-Au und 350°C für Ag-Co gewonnen. Bei diesen Temperaturen ist die Volumendiffusion nicht aktiv. Die niedrigere Diffusionsrate für Co bedingt die höhere Auslagertemperatur für diesen Prozess.

Die hohlen Nanowhisker wurden durch Rasterelektronenmikroskopie (englisch „Scanning Electron Microscope“ SEM) charakterisiert. Die Ergebnisse zeigten eine Abnahme des Ag-Gehaltes in dem Nanowhisker, im Gegenzug erhöhte sich der Ag-Gehalt im polykristallinen Film. Beides deutet auf die Diffusion von Ag-Atomen in

den Film. Nach der Herstellung wurde eine kinetische Studie für das Ag-Au System durchgeführt und ein Diffusionsmodell formuliert. Es beinhaltet, dass Ag-Atome entlang der Au-C Grenzfläche diffundieren und nicht durch Interdiffusion durch die Au Hülle auf dem Nanowhisker. Die Ag-Atome bewegen sich dann durch die Korngrenzen des polykristallinen Au Films und werden durch Oberflächendiffusion abtransportiert. Die kinetische Untersuchung ergab den Zusammenhang zwischen der Zeit die benötigt wird um eine vollständige Aushöhlung zu erreichen und der Größe des Nanowhiskers. Das Resultat war, dass dünnere Strukturen schneller aushöhlen.

Als Zusammenfassung lässt sich feststellen: einkristalline, defektfreie und freistehende Nanoröhrchen (Au, Pd und Co) wurden erfolgreich durch Kurzschlussdiffusion hergestellt. Dies stellt eine alternative und neue Methode dar hohle metallische Nanostrukturen zu produzieren. Ihre Defektfreiheit mag einige neue Anwendungen ermöglichen. Die Nanostrukturen wurden durch hochauflösende Rasterelektronenmikroskopie welches mit einem energiedispersiven Röntgenspektrometer und konventionelle Transmissionselektronenmikroskopie untersucht. Das formulierte Diffusionsmodell kann auf verschiedene Materialsysteme mit gleicher Gefügestruktur angewendet werden.

ABSTRACT

Hollow metal nanostructures are of great interest because of their unique plasmonic, catalytic and magnetic properties and their usage in the field of nanotechnology. Various methods have been employed to produce nanostructures mostly based on the template approach, which often result in polycrystalline nanostructures with a high concentration of impurities and defects. The process of pores nucleation and growth is difficult to control and their size and shape are limited since they are greatly dependent on the template. Thus, it becomes an important issue to produce these structures.

Here, we introduce a new route to synthesis perfectly single crystalline, defect free and freestanding metal nanotubes (NTs) from a metal nanowhisker (NW) template by the dissolution of the core material by the grain boundary diffusion.

With this aim, single crystalline Ag and Cu nanowhiskers (diameter: 100-150 nm and length: 4-30 μ m) were synthesized on a carbon-coated Si/SiO₂/Si₃N₄ substrate at 650 °C by molecular beam epitaxy (MBE). Different materials (Au, Pd, Co) were grown as shell on the Ag NWs at room temperature and Ni shell was grown on the Cu NWs. The metals (Au, Pd, Co), which were deposited as shell on the Ag NWs, grew as single crystalline heteroepitaxial layer on the Ag whiskers. Ni shell also grew as single crystalline shell on the Cu NWs. In contrast the shell materials formed polycrystalline films on the substrate. The metal nanotubes were obtained via annealing of these core-shell structures at temperatures below 200 °C for Ag-Pd and Ag-Au nanowhiskers and 350 °C for Ag-Co. At these annealing temperatures the bulk diffusion is not active. The lower diffusion rate in Co required a higher temperature for the process.

The hollow nanowhiskers were characterized by scanning electron microscope (SEM) and the result showed a decrease of Ag content in the nanowhisker, whereas significant increase of Ag content in the polycrystalline film clearly indicated the diffusion of the Ag atoms into the film. After the fabrication of the Au nanotubes, a kinetic study was performed for the Ag-Au system and a diffusion model was formulated. It implies that Ag atoms diffused along the Au-C interface instead of interdiffusion with the Au whisker shell. The Ag atoms then entered into the grain

boundaries of the polycrystalline Au film and diffused away by the surface diffusion. The kinetic study also showed the relationship between the time for the full hollowing and the size of the nanowhisker. It was found that the thinner whiskers hollow faster.

In conclusion, single crystalline, defect free and free standing metal nanotubes (Au, Pd and Co) are successfully produced via short-circuit diffusion process which represents an alternative new route of producing of hollow metal nanostructures. Their defect-free microstructure may open a way for a number of new applications. The nanostructures are characterized by high-resolution scanning electron microscope (HRSEM) equipped with an energy-dispersive X-ray spectrometer (EDS) and conventional transmission electron microscope (TEM). The diffusion model is formulated which can be used for different material systems of similar microstructure.

1 INTRODUCTION

Nanotechnology has become important in recent years with a wide range of disciplines and technologies all over the world. Even though it started developing in the last decades, it actually has a long history. One of the first trace of nanotechnology can be seen in the Lycurgus cup that was made of glass by the Romans [1]. The cup has different colors when it is illuminated, depending on whether the light is reflected or transmitted. This is because of the surface plasmons of the gold and silver nanoparticles embedded in the glass.



Figure 1: The Lycurgus cup made by Romans [1]

However, nanotechnology became one of the biggest research subject only in the last 30 years. After the discovery of carbon nanotubes by Iijima in 1991 [2], the nanotubes have excited great interest due to their hollow structure which can provide more surface area and some other functional properties such as high photocatalytic efficiency, more electroactive site, etc.

Metal nanotubes attracted somewhat lower interest than their carbon counterparts. In recent years there is a surge in research on metal nanotubes because of their potential applications such as electronic or magnetic devices, in catalysis, imaging, sensors, drug delivery, etc. [3-5]. For instance gold nanotubes are of interest mostly because of their plasmonic, electrical, catalytic and optical properties, besides having lower

toxicity and a remarkable resistance to oxidation [6, 7]. Ferromagnetic Ni and Co nanotubes are being investigated due to their possible applications in perpendicular magnetic recording, cell separation, magnetic resonance imaging for detection [8]. Pd nanotubes have attracted growing interest thanks to their catalytic activity and good stability [5]. However, the available fabrication methods of metal nanotubes allow only limited control of their geometry and microstructure. Therefore, there is an urgent need for an alternative fabrication routes.

The reported fabrication process for hollow nanostructures are mainly chemical etching, galvanic replacement reactions and many other method based on the template approach such as electrochemical deposition, sol-gel, chemical vapor deposition and electroless plating [6, 9]. All of these fabrication processes exhibit some disadvantages such as i) the fabrication processes are complicated because of the etching procedure of anodic aluminum oxide template ii) it introduces impurities in the nanotubes iii) the control on the alignment of the nanotubes is limited v) the produced nanostructures are polycrystalline with a high concentration of defects vi) the control over the size and shape is limited because of the used templates [3, 10-12].

The Kirkendall effect, which is a classical phenomenon in metallurgy based on the diffusion (12), was recently applied to produce nanotubes from core-shell nanostructures [13, 14]. A significant advantage of the Kirkendall effect-based methods of synthesis of hollow nanostructures over the alternative chemistry-based methods is in the possibility of “fine tuning” of the size of the pores. Indeed, since the atomic diffusion in the solid state is relatively slow, the size control can be simply achieved by a proper selection of the annealing/reaction time. Yet this method requires relatively high homological temperatures at which the bulk interdiffusion is active. Since surface diffusion is much faster than bulk diffusion, the morphological stability of complex nanostructures becomes problematic at such high temperatures. Indeed, recent atomistic molecular dynamic simulations revealed that the hollow core in a cylindrical nanotube formed by the Kirkendall effect loses its stability and breaks down into an array of nanopores in a process similar to Rayleigh instability of rods [15]. Moreover, a prolonged annealing leads to the closure of the pore and full homogenization of the particle [16].

In this thesis, a new route is used to produce metal nanotubes that relies on the carbon-mediated synthesis of core-shell metal nanowhiskers employing the molecular beam epitaxy technique. For the Ag-Au core-shell nanowhiskers the outer Au layer covers epitaxially the single crystalline Ag whiskers, but is nanocrystalline on the substrate surface between the whiskers. Annealing of this system at 170°C, at which no bulk interdiffusion between Au and Ag occurs, resulted in hollowing of the core-shell nanowhiskers and formation of Au nanotubes [17]. It was suggested that the Ag atoms of the core diffuse along the grain boundaries (GBs) of the polycrystalline Au film, thus hollowing the core of the composite Au/Ag whiskers and leading to the formation of perfect single crystalline hollow core Au nanotubes. This mechanism is different from the bulk Kirkendall effect mechanism discussed earlier [13], and bears many similarities with the classical lost-wax metal casting process known for millennia. This method has all the advantages of the methods based on the bulk Kirkendall effect proposed earlier [13] and, in addition, rather than relying on a random pore nucleation process, it allows “sculpturing” the shape, size and morphology of internal porosity by the original “core” nanostructure. After formulating the diffusion model for Ag-Au systems, the same model was applied to describe the hollowing process of different (Pd, Co and Ni) metal nanotubes.

The aims of this work were fabricating metal (Au, Pd, Co and Ni) nanotubes, studying the kinetics of core-shell nanowhiskers hollowing, developing the kinetic theory of the hollowing process, and identifying the atomic processes which control the hollowing kinetics.

2 THEORETICAL BACKGROUND

2.1 Principles of Thin Film Growth

Thin film growth is the process of producing a film from the bulk material by extracting its atoms, molecules, or ions. The basis of thin film growth, which involves the process of nucleation and growth, will be discussed in this section. There are several steps for thin film formation as described in the followings.

One of the most important parameter describing the arrival of atom at the substrate is the deposition rate (R) [18].

The nucleation rate describes how many nuclei form on a unit area of the substrate per unit of time. Nuclei can grow through direct impingement of gas phase atoms when the nuclei are placed far from each other. The rate at which nuclei grow depends on the rate at which adatoms attach to it. The energetic adatoms can also desorb directly when they reach to the surface if the substrate temperature is too high. Their residence time on the substrate, τ_s , is given by;

$$\tau_s = \frac{1}{\nu} \exp \frac{E_{des}}{kT} \quad (1)$$

where the ν is the vibrational frequency of the adatom on the surface and E_{des} is the required energy for the desorption.

When the adatoms first reach the surface they can diffuse along the surface and the diffusion length is given by:

$$X = \sqrt{2D_s\tau_s} \quad (2)$$

where D_s is the surface diffusion coefficient and is given by:

$$D_s = \left(\frac{1}{2}\right) a_0^2 \nu \exp\left(-\frac{E_s}{kT}\right) \quad (3)$$

where E_s is the activation energy for surface diffusion a_0 is the distance of a jump. Therefore,

$$X = a_0 \exp \frac{E_{des} - E_s}{2kT} \quad (4)$$

The adatoms during the surface diffusion can form pairs with other adatoms, or attach to larger atomic cluster or nuclei. The substrate temperature (T) is the most important parameter for the atomic migration on the surface. It is mostly kept lower than the temperature of the vapor source and the melting point of the material to lower the re-evaporation of the arrived atoms. The temperature for the growth is usually around $0.65T_m$ for the crystal formation, where T_m is the melting point of the deposited material. When the atoms arrive to the surface of the substrate, they diffuse along the surface due to the substrate's thermal energy. During surface diffusion, they collide and form clusters which results in stable nucleus when they reach certain size. Additional atoms can then attach to that stable nucleus and form a thin film.

The deposition rate and the substrate temperature play an important role in the morphology and structure of the deposited films. It was found that smoother films could be obtained at higher temperature or lower deposition rate [19]. The temperature has an effect on the mobility of the atoms. If the temperature is relatively low, the arrived atoms will not have enough mobility to diffuse on the surface and the nuclei will start to grow at their arrival sites on the substrate. If the substrate temperature is relatively high, it will allow the arriving atoms to diffuse further and faster to search for the lowest energy nucleation site, which will lead to fewer nucleation sites and to larger the grains in the thin film [20]. On the other side, if the temperature is too high, the desorption rate will be higher. Also, the deposition rate affects the sample roughness. Increasing the deposition rate merges the neighboring atoms together and it leads to a rough surface. For example, if the substrate temperature is low and the deposition rate is high compared with the diffusion rate, it will lead to the formation of amorphous film [18].

The system always wants to go in to the direction of minimizing the total energy so that the surface free energies and the interface energy are very important since they define the mode of growth, if the growth is not controlled by kinetics. There are three different growth modes explained in the next sections.

2.1.1 Volmer-Weber (Island) Growth

In the island growth mode, atoms arriving at the substrate nucleate with 3D island shape shown in Figure 2. Once the nuclei are formed, other atoms reach them via

surface diffusion. This type of growth occurs when atoms or molecules of the deposited materials are more strongly bound to each other than to the substrate. It is because these two materials have different chemical properties or a large lattice mismatch between them.

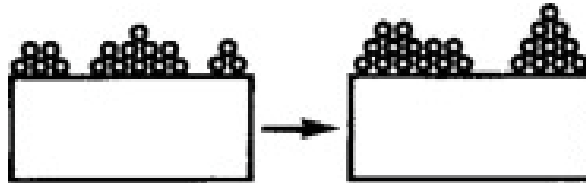


Figure 2: Island growth mode [21]

2.1.2 Frank-van der Merwe (Layer) Growth

This is a growth mode in which atoms form 2D continuous layers on the substrate as shown in Figure 3. This mode is also known layer-by-layer growth. This growth mode occurs when the deposited material is the same as the substrate, when they have the same crystal structure with similar lattice constants. This growth mode allows achieving atomically flat thin films, fabricating superlattices and heterostructure devices. This mode is very different from the island growth mode in terms of the bounding between the deposited materials and the substrate. The atoms are more strongly bound to the substrate than to each other.



Figure 3: Layer growth mode [21]

2.1.3 Stranski-Krastanov Growth

This is a “layer plus island” growth mechanism which is a combination of the previous two modes. After the formation of one or more monolayers, island growth becomes more favorable. The transition from 2D to 3D can occur from any disturbing factor. For example, the relaxation of the strain energy, which accumulates in the

growing film, may trigger island formation. The schematic illustration is shown in Figure 4.

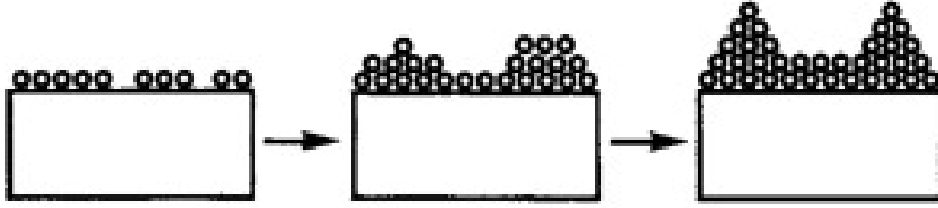


Figure 4: Stranski-Krastanov growth mode [21]

To determine which one of these growth modes will occur, considering a simple droplet model is useful (see in Figure 5 [22]).

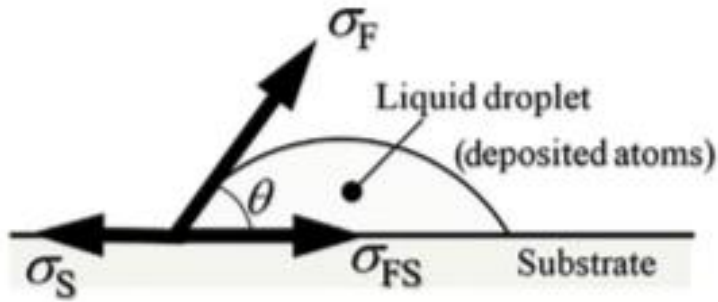


Figure 5: Schematic illustration of the liquid drop model [22]

The following Young equation gives us the relationship between the surface energies of the droplet (σ_F), the substrate (σ_S) and the energy at the interface between the droplet and the substrate (σ_{FS}).

$$\sigma_F \cos \theta + \sigma_{FS} = \sigma_S \quad (5)$$

For an island growth, $\theta > 0$, and therefore

$$\sigma_F + \sigma_{FS} > \sigma_S \quad (6)$$

Since the sum of the surface energy of the film and the interface energy is bigger than the surface energy of the substrate, the energy of the system decreases by decreasing the interface area, which results in island growth.

For layer growth, $\theta=0$, and therefore

$$\sigma_F + \sigma_{FS} < \sigma_S \quad (7)$$

This means that the sum of the surface energy of the film and the interface energy is smaller than the surface energy of the substrate, and vapor deposited material expands over the entire surface resulting in layered growth.

If there is a substantial lattice mismatch between the substrate and the film, σ_{FS} becomes large because it contains contributions from the strain energy. Then the growth mode will be determined after the first monolayer formation. The growth mode will change from layer to the island growth.

2.2 Epitaxial Growth and Critical Thickness

There are two types of epitaxy that are homoepitaxy and heteroepitaxy. In the case of homoepitaxy, the film and substrate are the same material, while the film and substrate are different materials in the case of heteroepitaxy that is more common phenomenon.

When the film and the substrate are identical, the growth is called homoepitaxial and there is no strain in the film since the lattice parameters are matched perfectly. But when the lattice parameters are different, then there is a lattice mismatch between the film and the substrate, which can be calculated from the following equation.

$$f_m = \frac{a_f - a_{sub}}{a_{sub}} \quad (8)$$

Where a_f and a_{sub} are the lattice constant of the film and the lattice constant of the substrate, respectively. Depending on the lattice mismatch, two different cases can be considered. If the lattice mismatch is very small, the film material will be homogeneously strained. If there is a slightly larger lattice mismatch between the film and the substrate, the misfit strain will be relaxed by introducing of interface dislocations into the structure. The differences between the different cases are shown in Figure 6.

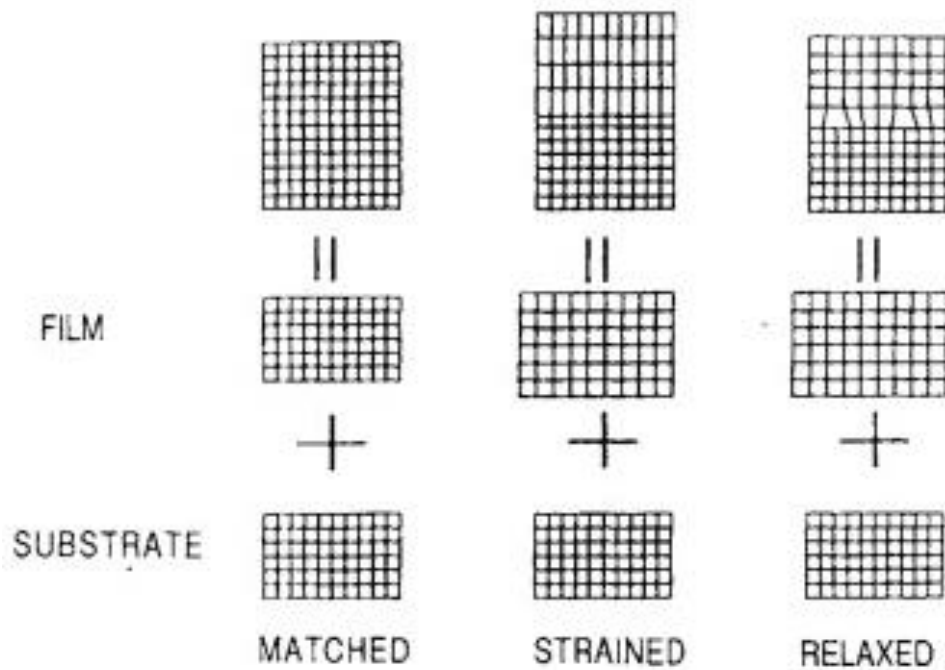


Figure 6: Schematic illustration of the structure depending on the lattice parameters [21]

The lattice mismatch can be accommodated without any introduction of dislocations even though it is large, depending on the film thickness. During the growth process the first few layers are deposited coherently with the matrix and the film lattice is distorted because of the strain. By increasing the film thickness, dislocations start to nucleate to relax the strain generated by the lattice mismatch. This thickness at which the strain relaxation occurs is called a critical thickness. The critical thickness calculated for Co/Cu system in the literature is shown in the Figure 7 [23].

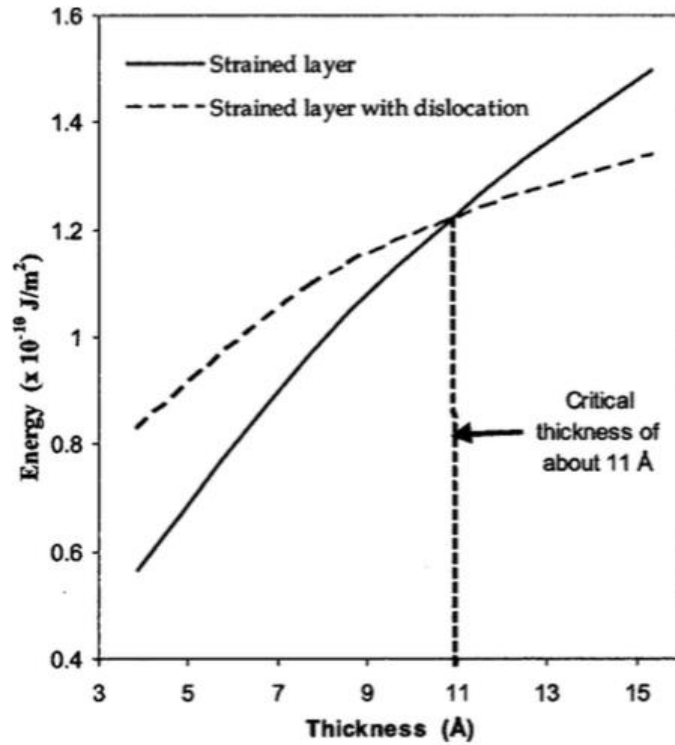


Figure 7: Calculation of the critical thickness for the Co/Cu system by FEM simulation [23]

The energy of the system per unit area of interface is increasing with increasing film thickness. The reduction of the energy due to nucleation of misfit dislocations can be seen from the graph. The dislocations became energetically favorable after the critical thickness value of the film is exceeded. Thus, if the film thickness is kept under the critical thickness then the dislocations can be avoided also in the structures with large lattice mismatch [23].

2.3 Whisker Growth

Single crystalline metal nanowhiskers have been under investigation for their mechanical [24], ferromagnetic [25], and plasmonic [26] properties. The whisker growth is generally considered as a filamentary growth of single crystal on a solid surface.

The first observation of the growth of crystalline whiskers from the vapor phase was with mercury, reported in 1953 by Sears [27]. The whiskers were presumed to be perfect except for a single axial screw dislocation, which was explained by the Frank's mechanism [28]. According to Frank, a screw dislocation emerging at the

crystal surface provides a permanent growth steps (see Figure 8). The spiral step around the dislocation core provides energetically favored sites where atoms can nucleate. This mechanism was soon accepted. However most of the whiskers were dislocation-free.

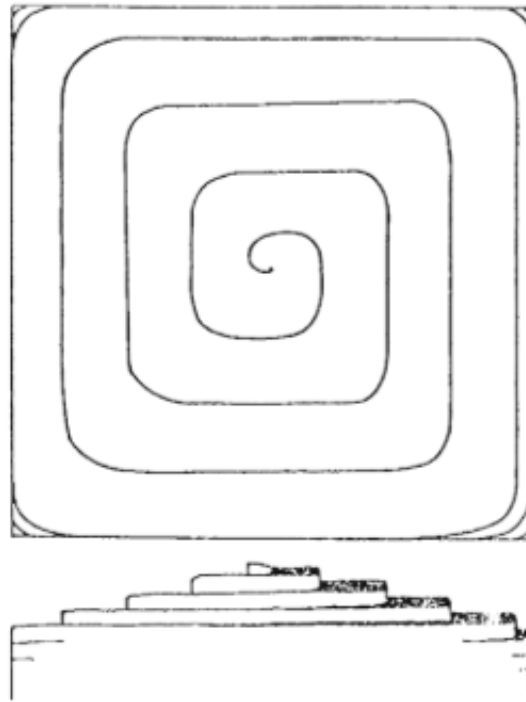


Figure 8: Emerging screw dislocation proposed by Frank [29]

The whiskers were found with a metallic spheres attached to their tips. This metallic spheres were ignored in the old times. After, the metallic spheres were identified for a new whisker growth model. They might have the same phenomena with the vapor liquid solid model (VLS) proposed by Ellis and Wagner [30]. The metallic spheres are called catalyst, which are used in VLS. The method of VLS whisker growth is illustrated in Figure 9. The metal catalyst nucleated on the substrate is heated and produce a liquid droplet. This catalytic liquid phase becomes supersaturated by adsorbing the vapor and the whisker begin to grow at the liquid solid interface.

Metallic whiskers have also been grown by reduction of metal halogenides and condensing the metal vapor on suitable metal substrates [28, 31, 32]. A large variety of metallic whiskers (Ag, Cu, Co, Fe, Au, Pt, Pd, and Ni) were grown by reduction of their salts in different atmospheres as well as by deposition from the pure vapor phase

[32]. These whiskers were single crystalline with a several micrometers diameter and centimeter lengths [33].

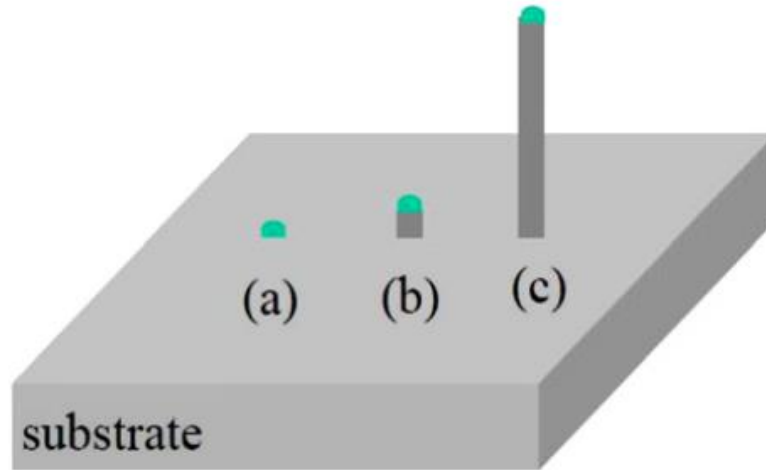


Figure 9: Schematic of the VLS growth mechanism (a) catalytic liquid alloy (b, c) whisker growth [34]

Recently, Richter et al. reported a new route to fabricate single crystalline metal nanowhiskers (NWs) with a high aspect ratio and no defects [35]. Their strength are close to the theoretical upper limits. The fabrication of different metal nanowhiskers on a C coated oxidized and nonoxidized Si (100), (110), and (111) substrates under ultra high vacuum (UHV) condition by molecular beam epitaxy was shown. It was claimed that the C layer is necessary and the temperature for the whisker growth should be on the order of $0.65 T_m$, where T_m is the melting temperature of the material. The SEM images of two Cu samples with nominal thicknesses of 45 and 200 nm are shown in Figure 10. The nanowhisker were free standing and straight with a maximum angle of 30° to the substrate normal. Although the diameter of the nanowhiskers, which are shown in the image (Figure 10a), vary between 30 and 100 nm and their maximum length is 10 μm , it was stated that the fabrication of whiskers of 20 nm in diameter and of 320 μm in length was possible with the same method. They also showed that the fabrication of larger whisker lengths and diameters with larger nominal thicknesses could be obtained (Figure 10b). The whisker did not grow on a substrate without C layer or on a substrate where C layer more was thicker than 40 nm. But they did not observe any relationship between the whisker dimension and the thickness of C layer.

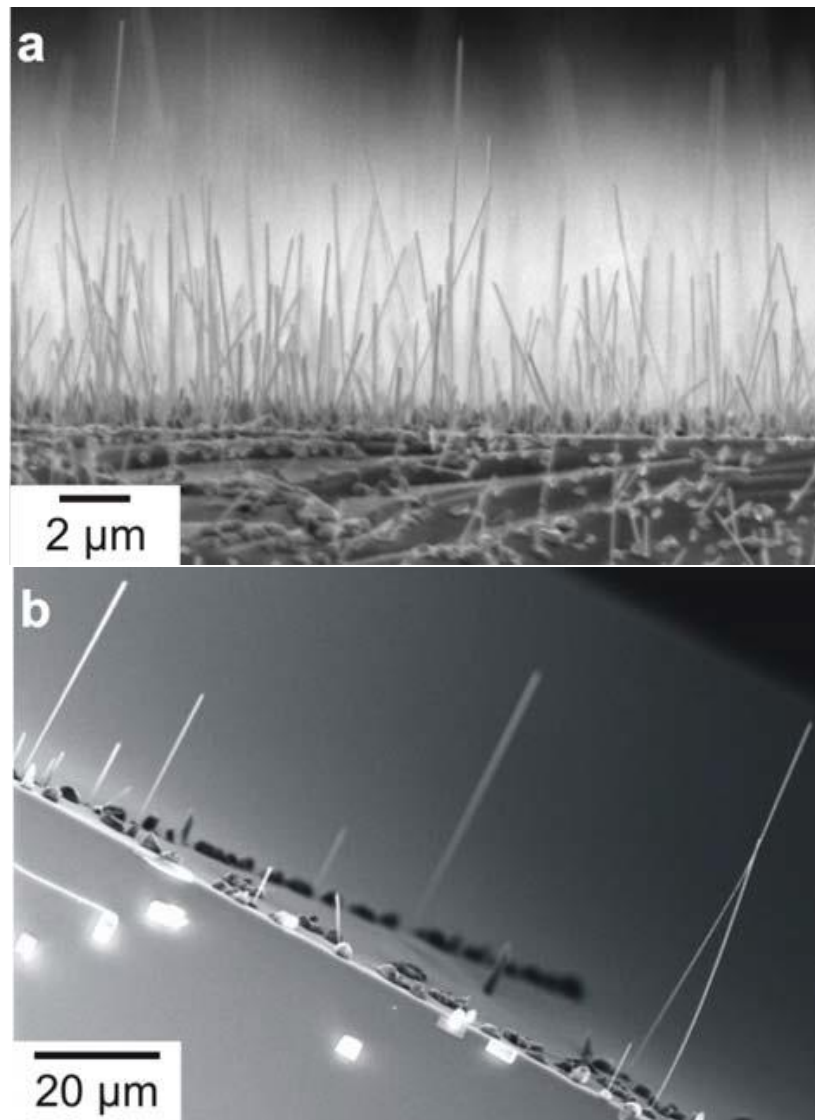


Figure 10: SEM images of Cu nanowhiskers. Nominal thicknesses of a) 45nm Cu and b) 200 nm Cu [35]

They have characterized a Cu whisker by transmission electron microscopy (shown in Figure 11). The nanowhiskers grew in the direction of $\langle 110 \rangle$. No defects as grain boundary, or dislocations, and especially classical screw dislocations were observed in the nanowhiskers, which disproves the classical growth models. The faceting of the nanowhisker is shown. The surface energy plays an important role in whisker formation. They have showed the formation of $\{111\}$ and $\{100\}$ crystal planes. The same results were obtained for the whiskers grown from other materials (Ag, Au, Al, Si). All material systems have demonstrated similar high aspect ratios. The density, diameter and length of the whiskers depend on the material. All grown whiskers were single crystalline.

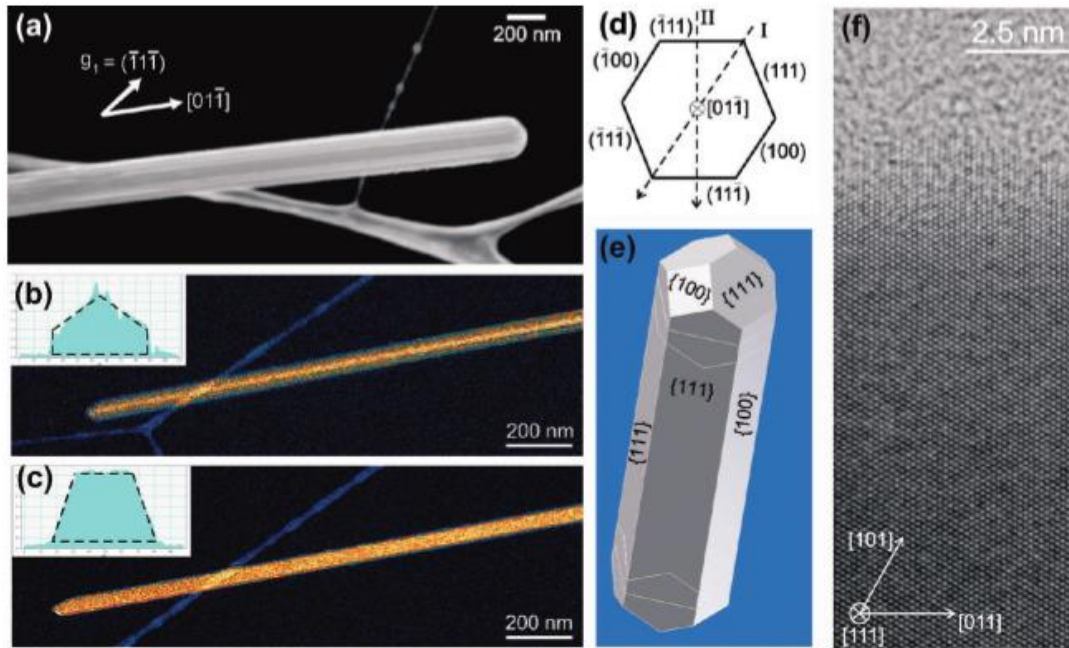


Figure 11: a) Dark-field TEM image b) Energy filtered TEM micrographs c) The whisker shown in (b) is rotated by 30° along the whisker axis d) Ideal whisker shape calculated by Cu free surface energies using the Wulff plot e) Cu whisker shape model based on Wulff plot f) High resolution TEM in $[111]$ zone axis [35]

The two of the growth mechanism mentioned earlier were ruled out, since no screw dislocation was observed or no catalyst was found on the tip of the whisker. They have mentioned the importance of C layer and related the growth with the interface energies. The nuclei formed on the opening in the C layer. Since the interfacial energy between Cu and C is high, it is energetically favorable for nuclei to grow vertically. Therefore, after the formation of the nuclei, their growth occurs by diffusion of Cu adatoms on the C layer to the formed nuclei and incorporation in it.

According to the whisker growth theory proposed by Ruth and Hirth [36], the atoms originating from two different sources are incorporated into the whiskers. One is the atom from the metal vapor. They impinge on the side of the whiskers, diffuse to the tip or to the root of the whisker. The other is the adatoms on the substrate. The adatoms diffuse along the surface due to the substrate temperature. They diffuse either to the root of the whisker or to the side facets. The ones diffusing to the side facets might have contribution either to the tip or to the root of the whisker again.

Richter et al. also established a growth model and rules for the nanowhisker growth according to their results and to the theory of Ruth and Hirth [37]: i) The metal atoms

have to condense on a suitable substrate with suitable substrate temperature to enhance the surface diffusion. ii) The substrate with two different surface areas (small and large) with different surface energies has to be used for whisker growth. Where, the small area is the one having higher surface energy, and having lower interface energy after the deposition of metal. iii) Due to the second rule, the metal adatoms on the larger area, diffuse to the small area. The metal adatoms reach to the small area either by direct impingement or by surface diffusion to form nucleus and grow. iv) Both direct impingement of the atoms on the side facets and diffusion of adatoms from the larger area, contribute to the whisker length. v) Using relatively higher growth rate leads to the formation of the nucleus on the side facets, which leads to the additional lateral growth of the nanowhiskers.

2.4 Interdiffusion and Kirkendall Effect

Diffusion process plays an important role in Material Science. After the discovery of the gold diffusion in solid lead in 1896 [38, 39], the atomic diffusion in metals was believed to take place by a direct exchange or ring mechanism as it is shown in the Figure 12. Interdiffusion between two solids has been studied for years and many studies of interdiffusion in bulk samples were reported. The Kirkendall effect was discovered in bulk diffusion couples of copper and zinc in a copper/brass system [40, 41]. The experimental data reported by Smigelskas and Kirkendall supported a vacancy exchange mechanism of bulk interdiffusion (see Figure 12c).

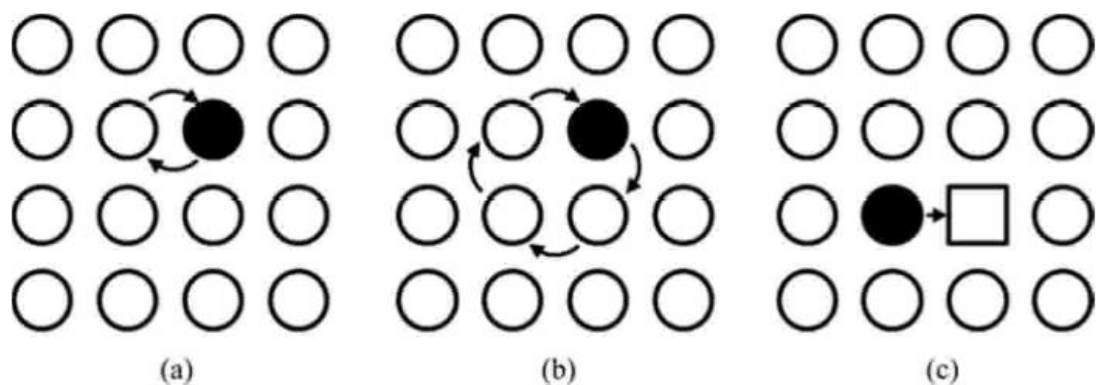


Figure 12: Atomic diffusion mechanism: a) Direct exchange mechanism; b) Ring mechanism; c) Vacancy mechanism [40]

In general there are two different diffusion coefficients in the two component system; D_A^1 and D_B^1 , which depend on the concentration. The subscripts A and B refer to the two different materials, A and B. Kirkendall explored the motion of the interface

between the two metals caused by an unbalanced diffusion. This effect is schematically shown in Figure 13. According to the Kirkendall effect, the initial interface between the metals moves during the annealing process because of the difference of diffusion coefficients of A and B atoms. Lets assume that the atoms of metal A diffuse in metal B faster than the atoms of metal B diffuse in metal A. This will lead to the formation of vacancies at the interface, on the side of metal A. This can be expressed by the inequality of atomic fluxes;

$$J_{A/B} > J_{B/A} \quad (9)$$

where $J_{A/B}$ and $J_{B/A}$ are the fluxes of atoms migrating from metal A to metal B and metal B to metal A, respectively. The vacancies will be absorbed by the sinks which may lead to the shrinkage of the lattice on the side of metal A, whereas the new atomic planes will be built in the region of metal B. This will lead to the lattice drift from B to A. The schematic illustration for these different stages, which occurs at the interface of the two metals are shown in the Figure 13.

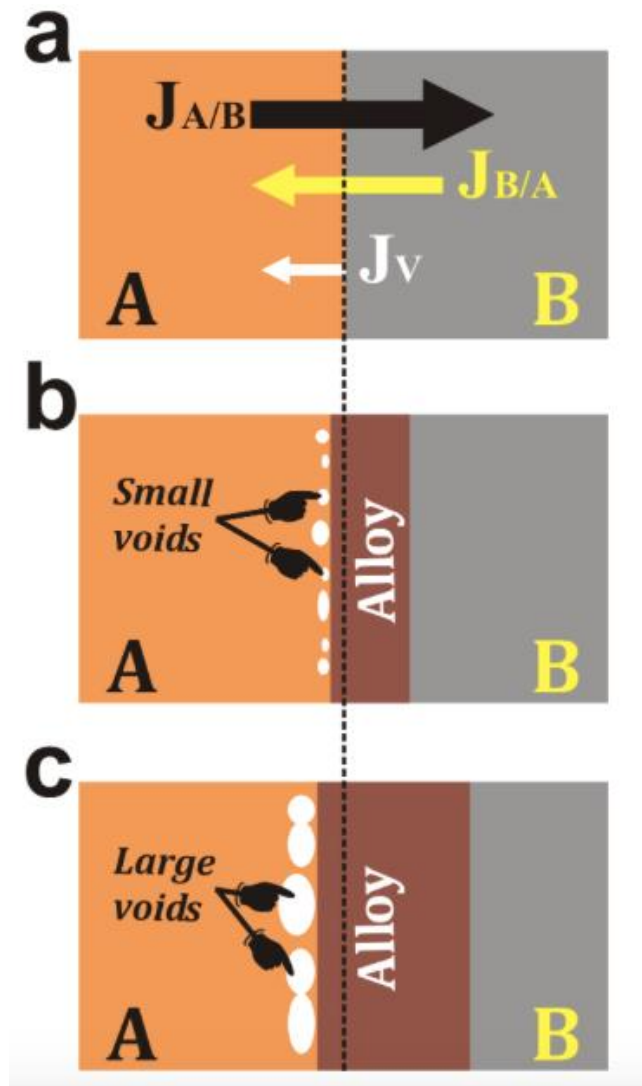


Figure 13: The interface between the metals according to the Kirkendall effect a) before annealing b) formation of small voids c) formation of large voids [42]

Under some circumstances the vacancies nucleated at the interface due to the different diffusion rates can merge together and form small voids. For longer times, the annealing process will lead to the coarsening of small voids into the large voids.

The Kirkendall effect was considered as a big problem because of the void formation. The studies were focused on the solutions to that problem. But recently, this effect has been employed as a useful tool in nanotechnology to produce hollow nanostructures [12, 13].

The formation of hollow nanoparticles was first reported by Yin et al. in 2004 [12]. They demonstrate that the formation of cobalt sulfide on the surface of cobalt nanoparticles exposed to sulfur-containing solution leads to the formation of hollow

cobalt sulfide nanoparticles. They observed the direct impact of the annealing temperature and the annealing time on the transformation kinetics of the nanoparticles from solid Co into hollow CoS. Since then, the Kirkendall effect has been applied to hollow a wide range of nanoparticles made of different materials, including metals [14-17].

The nucleation of pores in the interior of the particles was attributed to the Kirkendall porosity: the much faster outward diffusion of Co in the cobalt sulfide shell than the inward diffusion of S toward the center of the cobalt particle leads to an uncompensated vacancy flux toward the particle center. In bulk systems with abundant vacancy sources/sinks this flux results in lattice drift [18]. In metals, this drift proceeds by the climb of edge dislocations acting as vacancy sources/sinks [18]. Yet the nanoparticles are often free of dislocations, since any preexisting dislocation in the interior of nanoparticle would be attracted to the free surface by the strong image forces and annihilate there. This paucity of vacancy sinks leads to the supersaturation of vacancies in the center of the particle followed by the nucleation of a pore. The diffusion-induced Kirkendall porosity was utilized for the synthesis of hollow nanostructures in a number of systems [10, 20, 21]. The stages of the hollowing process vary according to the selected materials. For example Nakamura et al. found that the shape of the resulting hollow particles was asymmetric with a nonuniform shell thickness when oxidizing nickel nanospheres [43]. This effect was observed also in other couples [44-46]. The vacancies migrate and accumulate into a single void at the interface of Ni and NiO on one side of the nanoparticle, while the oxidizing process proceeds. It was reported that the NiO grew preferentially at the adjacent side of the void. Thus, the shell is thinner on one side and larger on the other side. A single large void was formed instead of smaller voids because the formation of a single large void is more favorable than the formation of small voids because of the surface energies. Li and Penner were the first ones who showed the feasibility of the Kirkendall effect to the fabrication of nanotubes [47]. They synthesized CdS nanotubes by high temperature sulfidation of Cd nanowires which were prepared by electrochemical step-edge decoration on graphite electrode surfaces. Since the nanowires were in contact with the graphite surface, the S diffusion was partially blocked, hemicylindrical CdS nanotubes were formed instead of cylindrical ones. In 2006, Fan et al synthesized monocrystalline spinel $ZnAl_2O_4$ nanotubes using

Kirkendall effect [48]. In this case, the nanotubes were formed by the two initial compounds, which were the core and the shell. The voids occurred at the interface within the ZnO, which diffuse faster in this case. Kirkendall effect has been employed in many other studies reported recently to synthesize hollowed nanostructured of different shapes. However, it requires relatively high bulk diffusivities and this can be achieved either at high homological temperatures [49], or due to high concentration of defects [50]. Its instability might lead to a string of voids instead of hollow cylinder [14]. In principle, the nanostructure produced by Kirkendall effect are unstable and they might collapse [51].

3 EXPERIMENTAL STUDY

The experimental studies that were conducted for producing metal nanotubes (Au, Pd, and Co) by using metal nanowhisker templates are described in this chapter. Metal nanotubes were produced via annealing of core-shell nanostructures, which were grown in two steps (see details in section 3.1.2.1) in the form of nanowhiskers on a carbon coated Si/SiO₂/Si₃N₄ substrates by molecular beam epitaxy (MBE). First attempts were performed on Ag-Au core-shell nanowhiskers to fabricate Au nanotubes. After successful growth of the Au nanotubes, a kinetic study was carried out for the Ag-Au core-shell material system and a diffusion model was formulated. The model has been then tested on the different material systems Pd, Co and Ni nanotubes. The nanostructures were characterized by using scanning electron microscope (SEM), high resolution scanning electron microscope (HRSEM) equipped with an energy-dispersive X-ray spectrometer (EDX), scanning transmission electron microscope (STEM) and conventional transmission electron microscope (TEM).

3.1 Physical Vapor Deposition Techniques

The deposition methods are basically divided into two main groups, which are physical vapor deposition (PVD) and chemical vapor deposition (CVD). Physical vapor deposition is a process in which atoms or molecules of a material are vaporized or sputtered from a solid and deposited on a substrate. The coatings, which were produced by Faraday in 1850s via evaporating the metals in the vacuum, are considered as the first application of PVD techniques [52].

In this study, two different PVD techniques, which were used to produce the samples, will be described. These are Molecular Beam Epitaxy (MBE) and Magnetron Sputtering PVD. The deposition of the amorphous C layer on the Si/ SiO₂/Si₃N₄ substrates were performed via Magnetron Sputtering PVD. The Ag and Cu whiskers and the metal shells on these whiskers (Au, Co, and Pd on the Ag whiskers and Ni on Cu whiskers) were grown via MBE.

3.1.1 Magnetron Sputtering PVD

Magnetron sputtering is a PVD method in which the target material is bombarded by energetic ions to eject the atoms by momentum transfer and the deposition is carried

out under high vacuum condition. The ions are accelerated from a plasma ignited close to the target. The plasma is generated by the electrons colliding with the gas atoms, while the electrons are accelerated from cathode to the anode. The cathode is the target material and the anode is not used in most of the magnetron sputtering systems, since the wall of the chamber act as an anode. The cathode is also used as electrode in DC sputtering system to sustain the glow discharge.

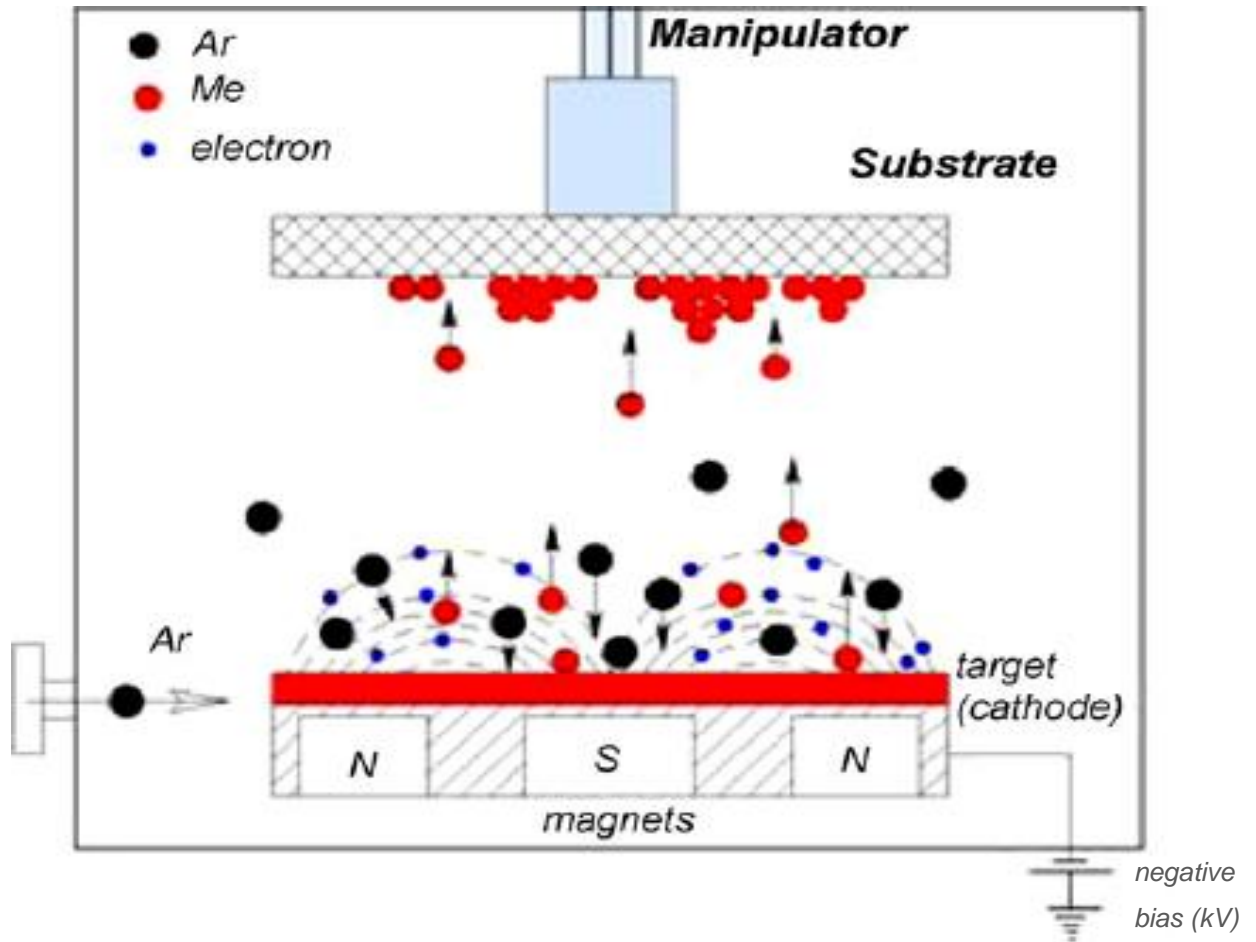


Figure 14: Schematic illustration of magnetron sputtering [53]

The electrons do not reach to the anode but remain in the vicinity of the target by applying a magnetic field oriented parallel to the target. The electrons are trapped near the target to enhance the ionizing efficiency there [54]. The increase in the ionizing efficiency leads to a denser plasma in the target region. The yield will be higher if the plasma is created close to the target surface and this is assured by magnets, which are placed behind the target. The ratio between the numbers of emitted particles per incident particle gives the sputter yield. The schematic illustration of the magnetron sputtering system is shown in Figure 14. The

sustainability of the plasma is ensured by the secondary electrons, which are generated during the bombardment of the surface of the target by the ions. Magnetron sputtering is one of the most commonly used PVD techniques. The reason for that is its high deposition rates, controlled and uniform deposition. To achieve dense films low pressures are needed.

3.1.1.1 Sample Preparation by Magnetron Sputtering PVD

Si/SiO₂/Si₃N₄ substrates which were commercially supplied from Crystec GMBH, were prepared by cutting the wafers into 1 cm*1 cm size. The substrates were cleaned in the ultrasonic bath with acetone and isopropyl alcohol for 10 min, respectively.

The substrates were coated with 30 nm amorphous C layer by magnetron sputtering PVD technique. The substrate was placed at the distance of 8 cm from the target material. The base pressure was 10⁻⁷ mbar. Magnetron sputtering was employed using the power of 100 Watt DC and the Ar pressure was kept at 10⁻³ mbar. The deposition carried out at room temperature and the deposition rate was 3,71 nm/min.

The morphology of the substrate was investigated by atomic force microscopy (AFM). In Figure 15, AFM image of a carbon deposited Si/SiO₂/Si₃N₄ substrate is presented. It was found that the roughness is important for the whisker growth as it is known that defects are needed as a nucleation site (see detail in [55]). That was the reason, why carbon was deposited on the silicon nitride wafers. Afterwards, the substrate with 30 nm C layer was transferred into the MBE chamber, which is in UHV condition, for whisker growth.

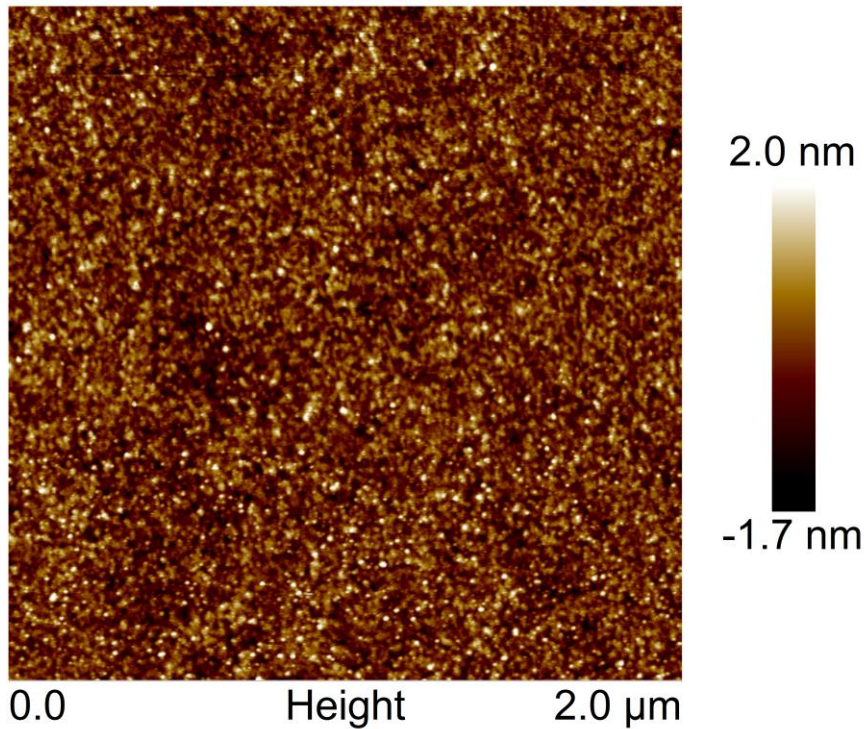


Figure 15: AFM image of the C deposited Si/SiO₂/Si₃N₄ substrate

3.1.2 Molecular Beam Epitaxy

Molecular beam epitaxy (MBE) is a method in which the epitaxial film is deposited onto single crystal substrates by using atomic or molecular beams produced from effusion cells (or Knudsen cells). The deposition is carried out in ultra high vacuum conditions. A load lock loading chamber for rapid change of substrates without breaking the vacuum helps to keep the depositing chamber in UHV condition. In UHV environment the atoms or molecules travel all the way to the substrate almost without collision. Very early example of the MBE growth was in the mid-1960s by Joyce and Bradley. They grew homoepitaxial silicon films from molecular beams of monosilane (SiH₄) [56]. It is equipped with in-situ monitoring systems, which allow us to control the growth thickness on the magnitude of 1 monolayer. These equipments are reflection high-energy electron diffraction (RHEED), quadrupole mass spectrometry (QMS), etc. The typical MBE system is shown in Figure 16.

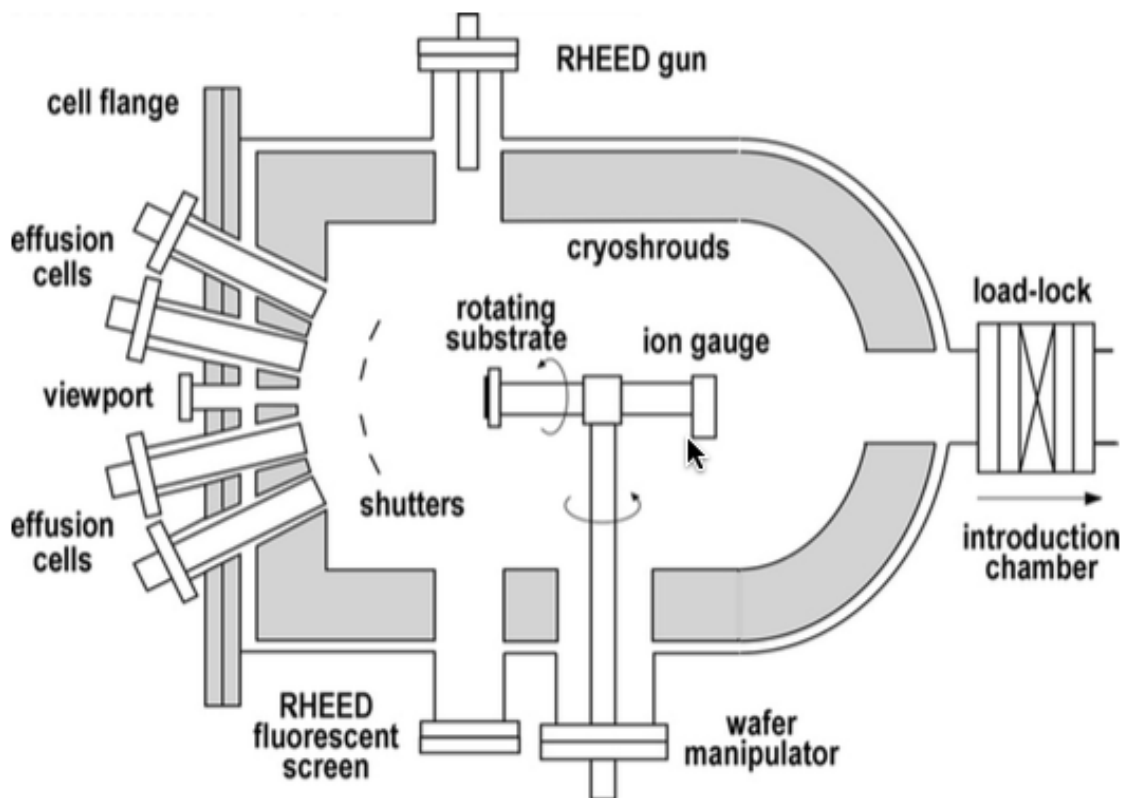


Figure 16: Schematic illustration of an MBE growth chamber [57]

The depositing materials are placed in the effusion cells, which are resistant to high temperatures. Typically, 10 effusion cells exist in the MBE chamber with mechanical shutters in front of them to switch on or off the molecular beams. Homo, hetero, and multilayer films can be fabricated via this method. The molecular or atomic beams are produced via heating these cells up and directing them on a substrate. The materials with higher melting point can be evaporated via e-beam. The substrate can be heated up to the elevated temperatures in order to obtain the desired epitaxial film. This temperature provides sufficient thermal energy to the atoms to migrate over the surface when they arrive at the substrate surface. It is easy to grow multilayer structures with different chemical composition within an atomic layer since the growth rates are typically of the order of $1 \text{ monolayer s}^{-1}$ [58]. The substrate holder is faced to the cells and mounted on a manipulator, which can rotate around the axis perpendicular to the axis of the cells. A thermocouple is placed behind the holder to read the substrate temperature. The homogeneity of the films can be improved by rotating the samples.

MBE system may also have a chamber equipped with surface characterization techniques such as Auger electron spectrometer, secondary ion mass spectrometry, electron spectroscopy for chemical analysis, or x-ray photoelectron spectroscopy.

3.1.2.1 Fabrication of Core-Shell Nanowhiskers by MBE

The core-shell nanowhiskers were produced in two steps. Firstly, single crystalline metal nanowhiskers were fabricated by molecular beam epitaxy. The method which is used for the fabrication of whiskers was developed by Gunther Richter [35]. Later, single crystalline metal shells were grown on the metal nanowhiskers again by molecular beam epitaxy. The details are given in the sections below.

3.1.2.1.1 Fabrication of Ag and Cu Nanowhiskers by MBE

The schematic illustration of the fabrication process is shown in Figure 17. The Si/SiO₂/Si₃N₄ substrates with 30 nm amorphous carbon layer were prepared as described in section 3.1.1.1. Afterwards, it was transferred into the MBE chamber for the deposition of the core materials. MBE is a technique, which is employed in ultra high vacuum condition. The base pressure in the chamber was 10⁻⁹ mbar. The samples were heated and it is assumed that defects were created on the carbon layer by heating the sample up. These defects served as nucleation sites for the metal adatoms. The holder with the substrate was rotated during the deposition process. Effusion cells were used to heat and evaporate the metals, which have a lower melting point and electron beam evaporation source was used for the metals, which have a higher melting point. An oscillating crystal measures the deposition rate and the nominal film thickness. The metals were heated up over the melting point, till it was reached to the rate, which was needed for the growth.

Two different nanowhisiker core fabricated in this study were Ag and Cu. Effusion cells were used to heat and evaporate the metals in the case of Ag and Cu deposition. The substrate temperature was 650 °C in both cases. The rate for the deposition was 0.05 nm/s for both metals. The duration for the deposition was 60 min and the nominal layer thickness was 180 nm both for Ag and Cu, since the same rate was used for both metals.

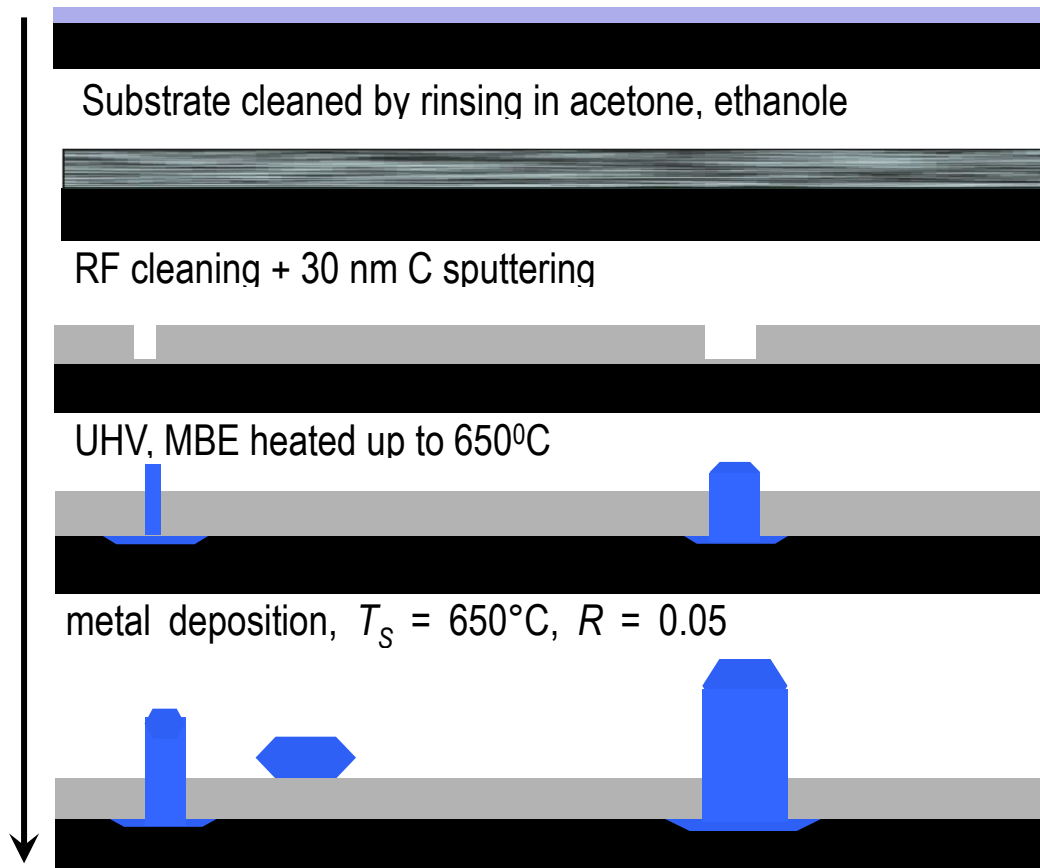


Figure 17: The schematic illustration of the fabrication process for the nanowhisker growth

The density of the whiskers can be controlled by the MBE deposition parameters (temperature, rate) since the substrate temperature and the deposition rate are the most important parameters, which have a high impact on the growth mechanism. The deposition was performed with different parameters to check the effect of the deposition rate and the deposition temperature on the growth and to find the suitable deposition parameters for the desired density of the whisker. The corresponding SEM images are shown in Figure 18. Two different temperatures and two different rates were used for this purpose. Using the higher rate at the same temperature (different rates at 650°C) resulted in a high island density and the higher temperature with the same rate (with the rate of 0.25nm/s) led to the formation of lower density. The deposition performed at 800 °C resulted in lower island density because of the high substrate temperature, which leads to higher adatom desorption. The deposition performed at 650 °C with the higher rate resulted in high island density because of the short diffusion distance of the adatoms.

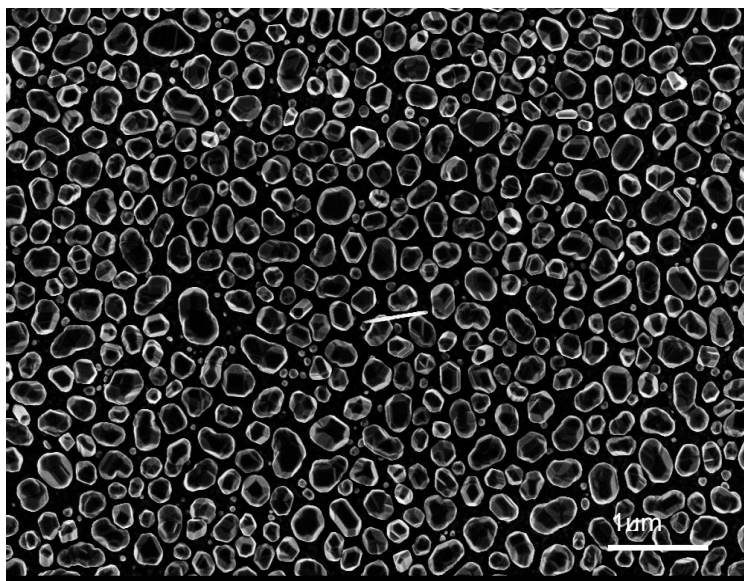
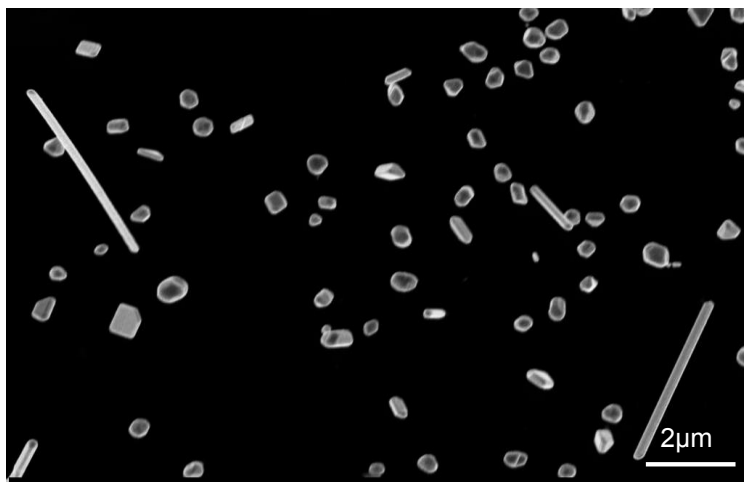


Figure 18: SEM images of Ag nanowhiskers produced at different temperatures and rates; a) 800°C, 0.25nm/s b) 650°C, 0.05nm/s c) 650°C, 0.25nm/s

3.1.2.1.2 Fabrication of Ag-Au, Ag-Pd, Ag-Co and Cu-Ni Core-Shell Nanowhiskers by MBE

Single-crystalline Ag-Au, Ag-Co, Ag-Pd and Cu-Ni core-shell nanowhiskers were fabricated employing the same method. Firstly single crystalline Ag and Cu metal nanowhiskers (Ag in the case of Ag-Au, Ag-Co, Ag-Pd and Cu in the case of Cu-Ni) were grown on a Si/SiO₂/Si₃N₄ substrate coated with a 30 nm thick layer of carbon as it was described above. Ag and Cu were deposited with the rate of 0.05nm/s. The deposition with this low rate resulted in single crystalline nanowhiskers, islands and plates on the substrate. The samples were kept inside the chamber and cooled down to the room temperature. Afterwards, different metals were deposited as shell upon the Ag and Cu nanowhiskers in the same MBE chamber at room temperature. The shell metals were deposited with the rate of 0.01 nm/s by MBE and the holder were rotated during the shell deposition as well. The illustration in Figure 19 shows core-shell fabrication process. Au, Pd, Co were deposited as shell on the Ag NWs. They grew as single crystalline shell on the Ag whiskers and as polycrystalline film on the substrate between the whiskers. The Ni was deposited as shell on the Cu NWs in the same chamber at room temperature with the rate of 0.01 nm/s by MBE. In this case too the Ni shell was single crystalline and the Ni layer on the substrate was polycrystalline. Au and Pd were evaporated by effusion cells. Ni and Co were evaporated by electron beam evaporation since they have higher melting point. All depositing materials were supplied commercially from the Lesker Company. The purity of the metals was 99,99 at. % .

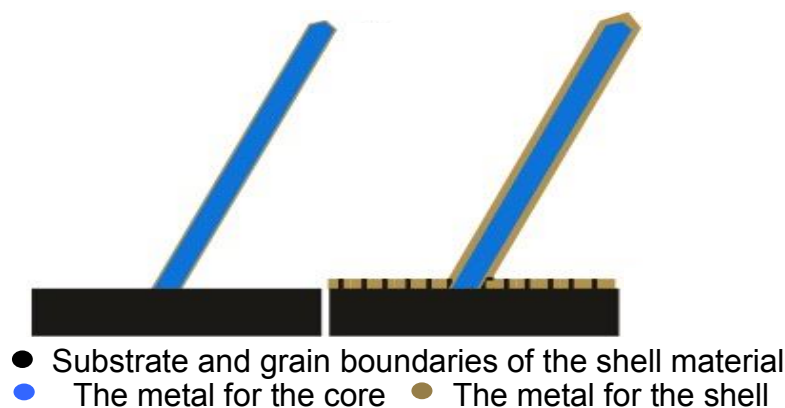


Figure 19: Schematic illustration of the fabrication process for the core-shell nanowhiskers

3.2 Fabrication of Metal Nanotubes

Au, Pd and Co nanotubes were obtained via annealing of corresponding core-shell nanostructures at 170 °C for Ag-Pd and Ag-Au nanowhiskers, and 350 °C for Ag-Co nanowhiskers in a rapid thermal annealing furnace (RTA; Ulvac-Riko, Model MILA-5000) for different times in the range of 5-30 min in Ar-10% H₂ gas flow of 150 sccm at 1 atm. The heating and cooling rates were 10 and 4 °C s⁻¹, respectively. The annealing temperatures were kept at the range where bulk diffusion is not active. The same result could be reached via annealing of these core-shell nanowhiskers in vacuum. However, hollowing process was slower in this case. The annealing in a tube resistance furnace in vacuum resulted in full hollowing only after 3 days. Annealing procedure was applied to Cu-Ni core-shell structures as well. Different temperatures and different annealing times were used but hollowing was not observed (see the results in section 4.6).

3.3 Kinetic Study and the Model

After the fabrication of the Au nanotubes, the kinetic study was done for the Ag-Au system (23 individual nanowhiskers were studied) and a diffusion model was formulated. This diffusion model was employed as a guideline in producing of Pd and Co nanotubes. The hollowing process in the Cu-Ni core-shell nanowhiskers did not occur. This is in agreement with the model, as will be explained in the results.

3.4 Characterization Techniques

The two electron microscopy techniques, which were used in this study to characterize the samples, will be outlined here. These are transmission electron microscopy and scanning electron microscopy.

3.4.1 Characterization of the Samples by Scanning Electron Microscope

Scanning electron microscopy (SEM) is most widely used characterization technique for thin films. The sample is scanned by a focused electron beam. Its main components are electron gun, electron column, scanning system, secondary electron detector, backscattered electron detector, display, vacuum system and electronics console. A schematic of a typical SEM is shown in Figure 20. The electrons, which are emitted from thermionic or field emission electron guns are accelerated through

the column and focused by the lenses. The spot size is generally less than 10 nm in SEM.

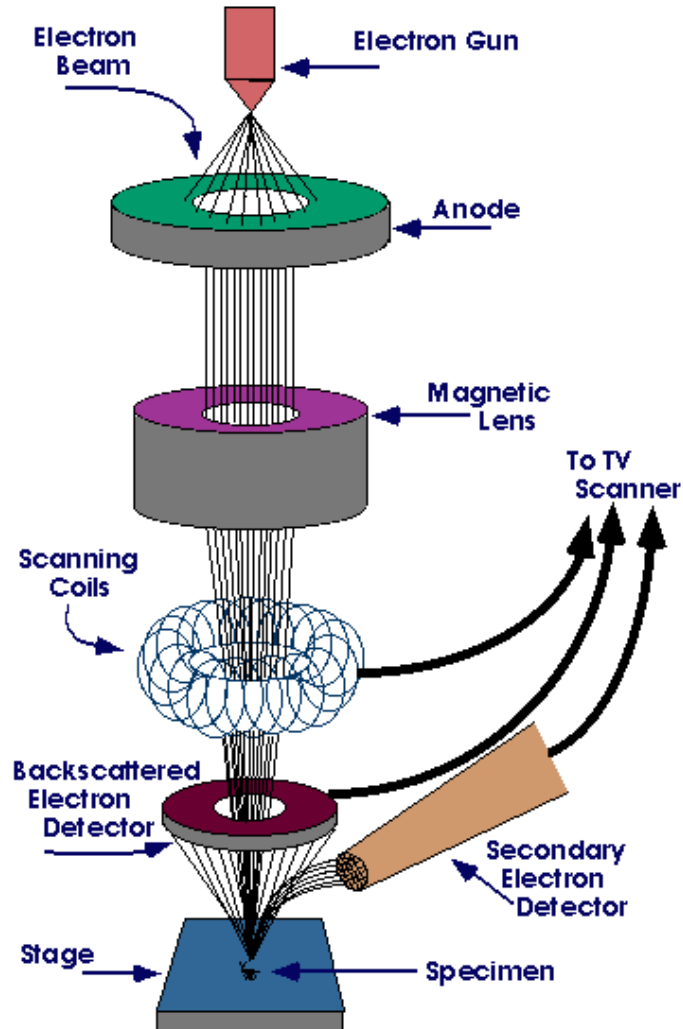


Figure 20: Schematic illustration of SEM [59]

The electrons hit the sample and penetrate to the depths scaling with their energy. Various signals are generated through this interaction between the electron and the sample, which contains information about the sample topography and composition, such as secondary electrons, backscattered electrons and X-rays (Figure 21).

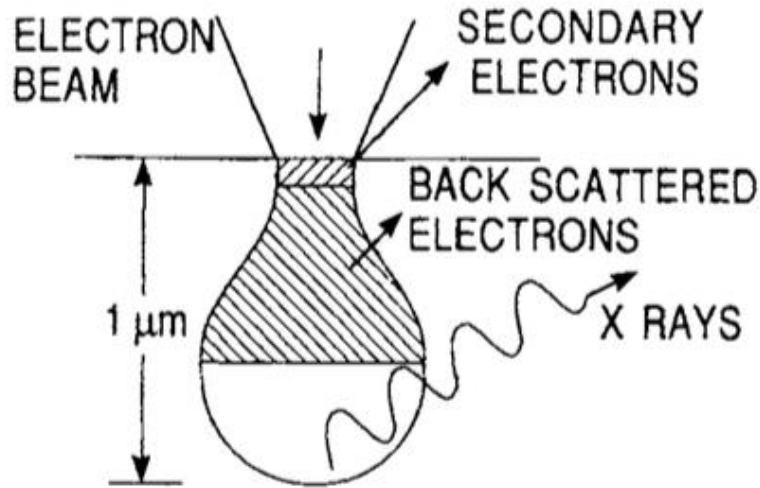


Figure 21: The signals generated by electron sample interactions in SEM [21]

Secondary electrons (SE) are the most commonly collected signals in SEM. They are generated within about the first 10 nm of the sample surface by the primary electron beam. The interaction volume increases with the increasing acceleration voltage. Secondary electrons are low energy electrons. They are used to produce topographic images with high resolution. Backscattered electrons are high-energy electrons, which are elastically scattered. They are used to show the contrast associated with the differences in chemical composition due to the atomic number of the sample. This is because the heavier elements scatter the electrons more efficiently than lighter elements. Characteristic X-rays are used for elemental analysis in the SEM.

The characterization of the samples was performed by different microscopy techniques. SEM images were acquired using field emission scanning electron microscope (Zeiss Leo) operated at an accelerating voltage of 3-10kV in secondary electron detection mode. HRSEM images were taken using high-resolution scanning electron microscope (Zeiss Ultra Plus) equipped with an energy-dispersive X-ray spectrometer (EDX) with a take off angle of 35° . HRSEM micrographs were acquired at acceleration voltage of 4-10kV in both secondary and back-scattered electron detection mode.

3.4.2 Characterization of the Samples by Transmission Electron Microscope

Material characterization in the electron microscope is based on the interaction of the electrons with the specimen. Transmission electron microscopy is used to characterize the samples, which are thin enough to transmit electrons. A broad electron beam

passes through a thin sample and produces an image, which is magnified by electromagnetic lenses. The image can be seen on a photographic film or CCD camera.

Thermionic and field emission guns are the two main methods to generate electrons. Thermionic guns (W or LaB₆) produces electrons (less monochromatic) by heating and the field emission guns (W) produce electrons (more monochromatic) by applying a large electric potential. The generated electrons are accelerated through a selected potential difference through the TEM column. The suitable electrons energy depends on the purpose or the specimen. For example, higher electron energies will be required if the specimen is thick or high resolution is needed. Thus, for some purposes medium (300-400 kV) and high (600-3000 kV) voltage microscopes have been developed. But the characterization in the microscopes with the lower electron energy has been improved by better lenses and better specimen preparations.

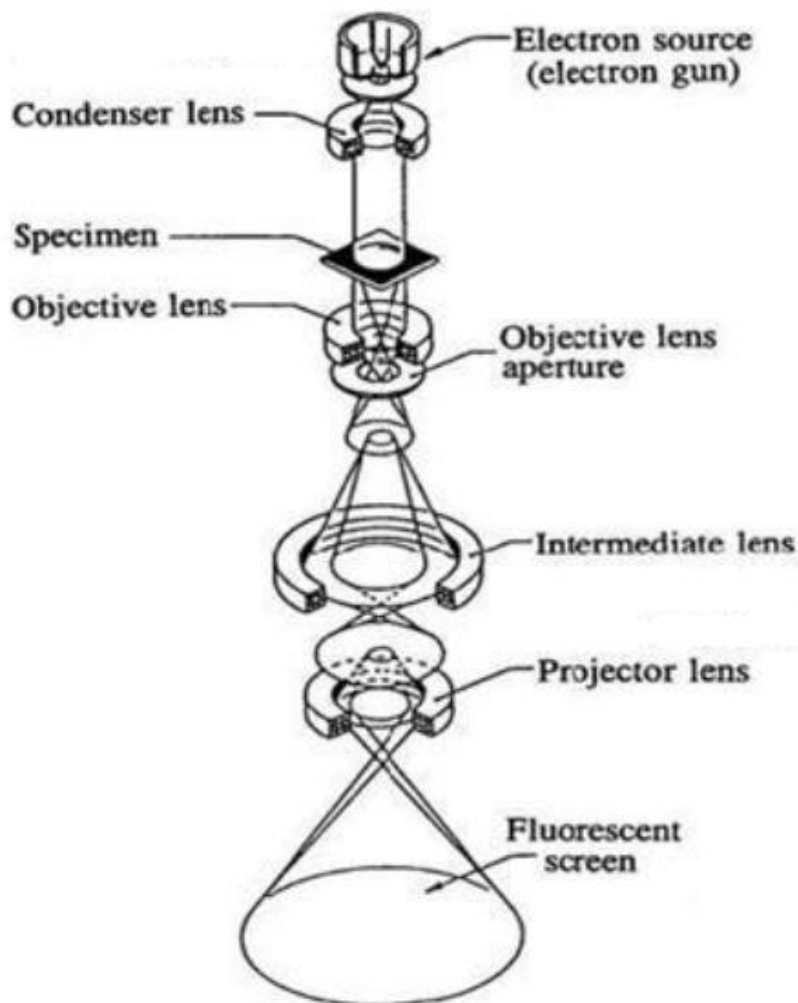


Figure 22: Schematic illustration of TEM [60]

A schematic of TEM microscope is given in the Figure 22. The electrons are accelerated towards the sample using a positive electric potential. The electron beam, which travels through the microscope column, is focused by the condenser lens and the electrons with the higher angles than specific angle value are blocked by the condenser apertures. The electrons, which are allowed to pass through, interact with the sample which is thin enough to let them pass through without losing too much energy. Then the objective lens focuses the transmitted electrons and forms an image. The electrons, which will contribute to the image, can be selected via objective aperture. The image produced on the back focal plane of the objective lens leads to the formation of either magnified images or diffraction patterns. The image can be formed in dark field or bright field mode by choosing the diffracted beam (magnifying a single beam) or the direct beam, respectively.

Different structural information can be derived from different electron interactions with the sample. The possible signals generated when the electrons interact with the specimen are given in Figure 23. Although the most probable route for the electrons is a passage through the thin sample without any interactions, they can be scattered by the nuclei or orbiting electrons elastically or inelastically. Each of the produced signals is used for different techniques to provide chemical information or many other details about the specimens.

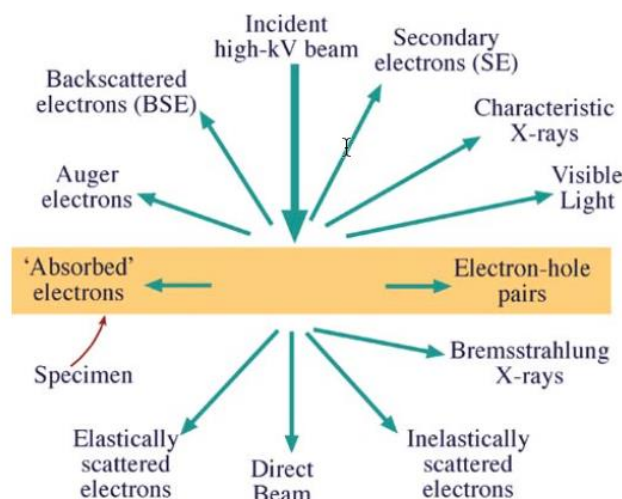


Figure 23: The signals generated from the electron sample interactions [61]

In order to prepare the samples for transmission electron microscopy, peel off technique was used. According to the technique, substrates were scratched by TEM

grid and the whiskers were collected on the grid. Nanowhiskers were lying on the different TEM grid after scratching the whiskers from the substrate. For the microstructure characterization of the nanowhiskers, Philips CM 200 transmission electron microscope was used. The acceleration voltage was 200 kV.

For the scanning transmission electron microscope characterization of the nanotubes, focused ion beam were used to prepare the samples in Eugen Rabkin`s group (Technion, Israel). The samples were prepared by the lift-out method in a dual beam focused ion beam (FEI Strate 400-S). The focused ion beam (FIB) lamellae were cut perpendicular to the projected nanowhisker axis, and positioned on a Ti grid. Final thinning was done by low-kV milling using Ar⁺ ions at an energy of 350 eV (linda GentleMill3). Scanning transmission electron microscopy images of the FIB prepared cross-section nanotubes were obtained on a FEI Titan 80-300 keV S7TEM.

4 RESULTS AND DISCUSSION

4.1 Characterization of Ag-Au Core-Shell Nanowhiskers

The typical morphologies of as produced Ag-Au core-shell nanowhiskers are presented in Figure 24. The samples are composed of whiskers, islands and platelets. Further observation reveals that the core-shell nanowhiskers have diameter of approximately 100 nm. The length of the whiskers varies from 4 μm to 20 μm . The size of the whiskers can be controlled with the duration of the deposition. For this sample, the thickness of the deposited layers was 180 nm for Ag and 20 nm for Au. The density of the whiskers can be controlled by the MBE deposition parameters (temperature, rate). For example lower density could be obtained, when preparing the samples at higher temperature with the same rate, or with lower rate at the same temperature. The sample, which is shown in the image, was grown at 650⁰ C (substrate temperature) and with the rate of 0.05 nm/s.

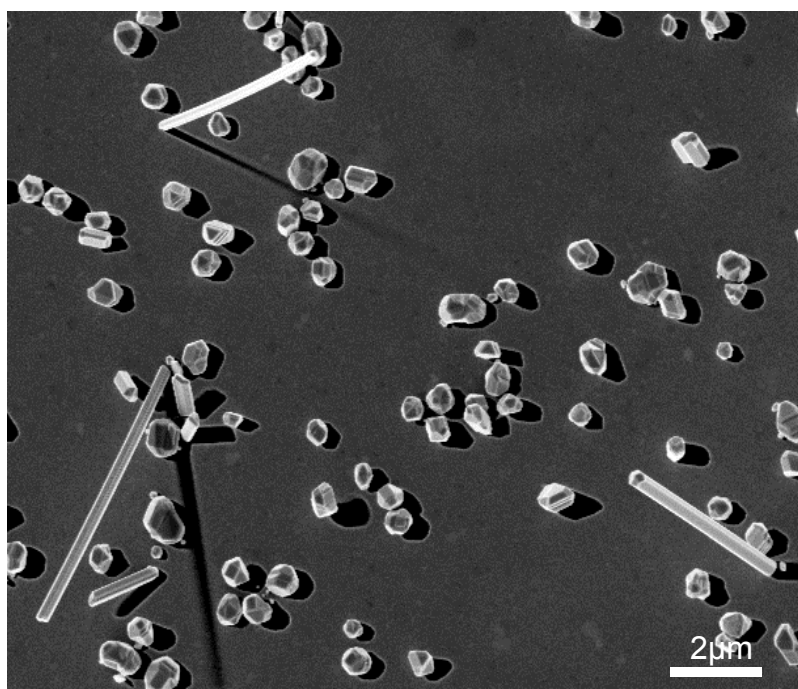


Figure 24: SEM images of Ag-Au core-shell nanowhiskers

Moreover, the whiskers have been further characterized by EDX, which shows the elemental analysis. Two typical Ag-Au core-shell nanowhiskers are presented in the Figure 25. The diameters of these nanowhiskers are 180 nm and 260 nm, respectively. They are composed of Ag and Au. They do not exhibit any compositional contrast

along the whisker and the corresponding Ag content is in the range of 50–55 at. % Ag. From the EDX result it was also observed that the film on the substrate does not contain any Ag. There is only Au film on top of the carbon layer. It can also be clearly seen that the Au film on the substrate is polycrystalline. Nanowhiskers are faceted and the facets can be also seen in the image.

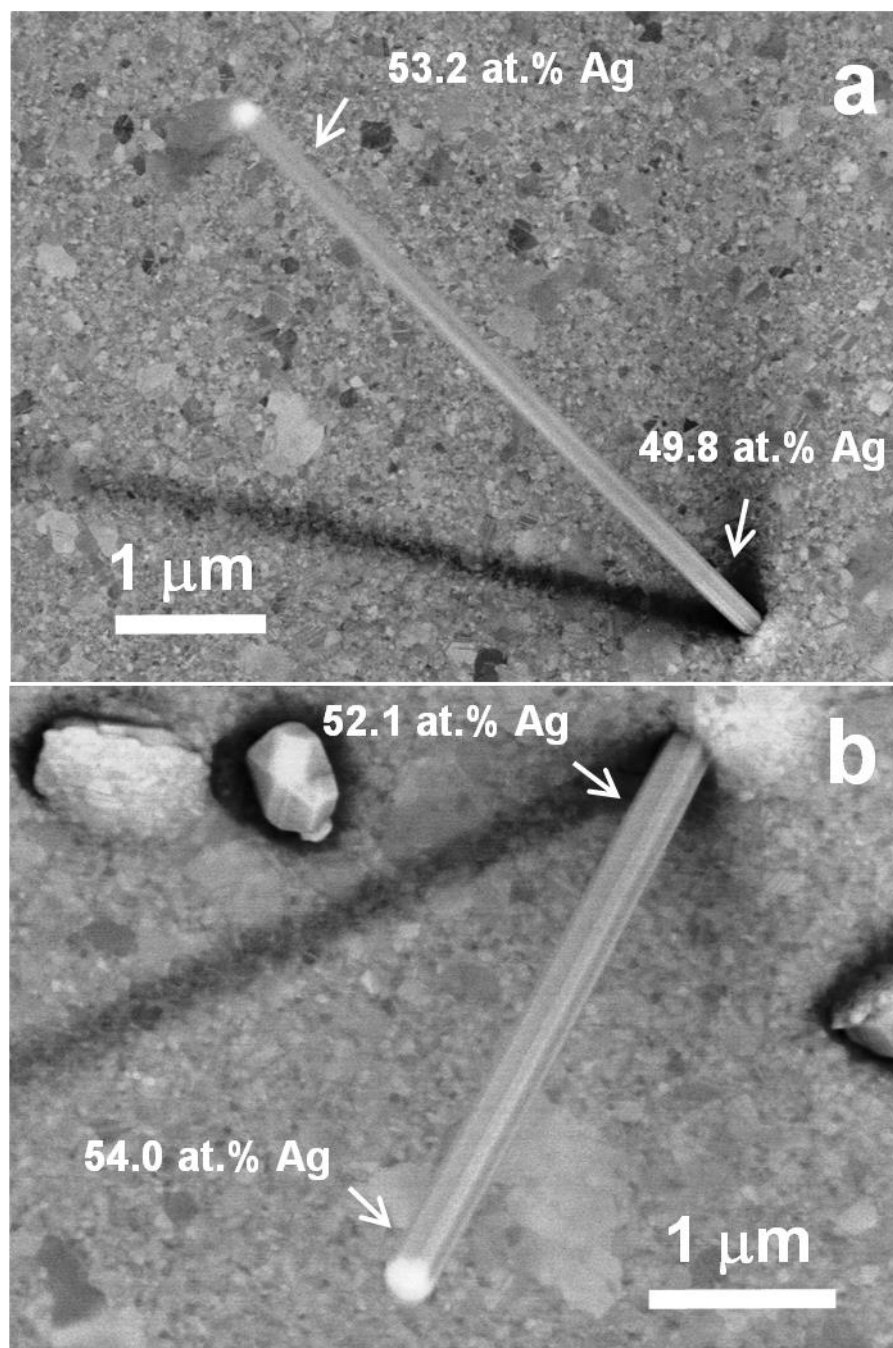


Figure 25: HRSEM images of two typical Ag-Au core-shell nanowhiskers with the average Ag contents, which were determined from EDS spectra

One single Ag-Au core-shell nanowhisker and its morphology were further studied with TEM. The similar features can be observed in the TEM image as shown in

Figure 26. The bright and dark field image shows that the nanowhisker is straight with the diameter of about 100 nm. The surface of the nanowhisker is atomically smooth. A very thin layer can be seen in the dark field image. It does not show the shell completely, but it indicates the edge of the Au shell on the whisker. There are no defects as grain boundaries or dislocations. The figure also shows a selected area electron diffraction (SAED) pattern where the single crystalline nature of the whiskers is seen. According to the literature data, one of the important conditions to obtain the epitaxial growth of heterogeneous shells in core-shell nanostructures is to assure less than 5% lattice mismatch between the two metals, which is the case in this material system [62]. The diffraction pattern can be indexed to face centered cubic (fcc) Ag and Au in the [111] zone axis. Au and Ag are chemically very similar and they both crystallize in the face centered- cubic (fcc) lattice structure with almost identical lattice constant, with very small lattice mismatch ($\sim 0,2\%$), so that the spots are overlapped in the diffraction pattern. As it can be seen, the sample is composed of single crystalline Ag-Au core-shell nanowhiskers and polycrystalline Au film on the carbon coated substrate. The composition of the whisker is studied with the aid of EDX acquired in TEM (see Figure 27). The spectra support the previous result that the core-shell nanowhiskers are composed of Ag and Au. The Cu sign arises from the Cu grid, which was used in TEM.

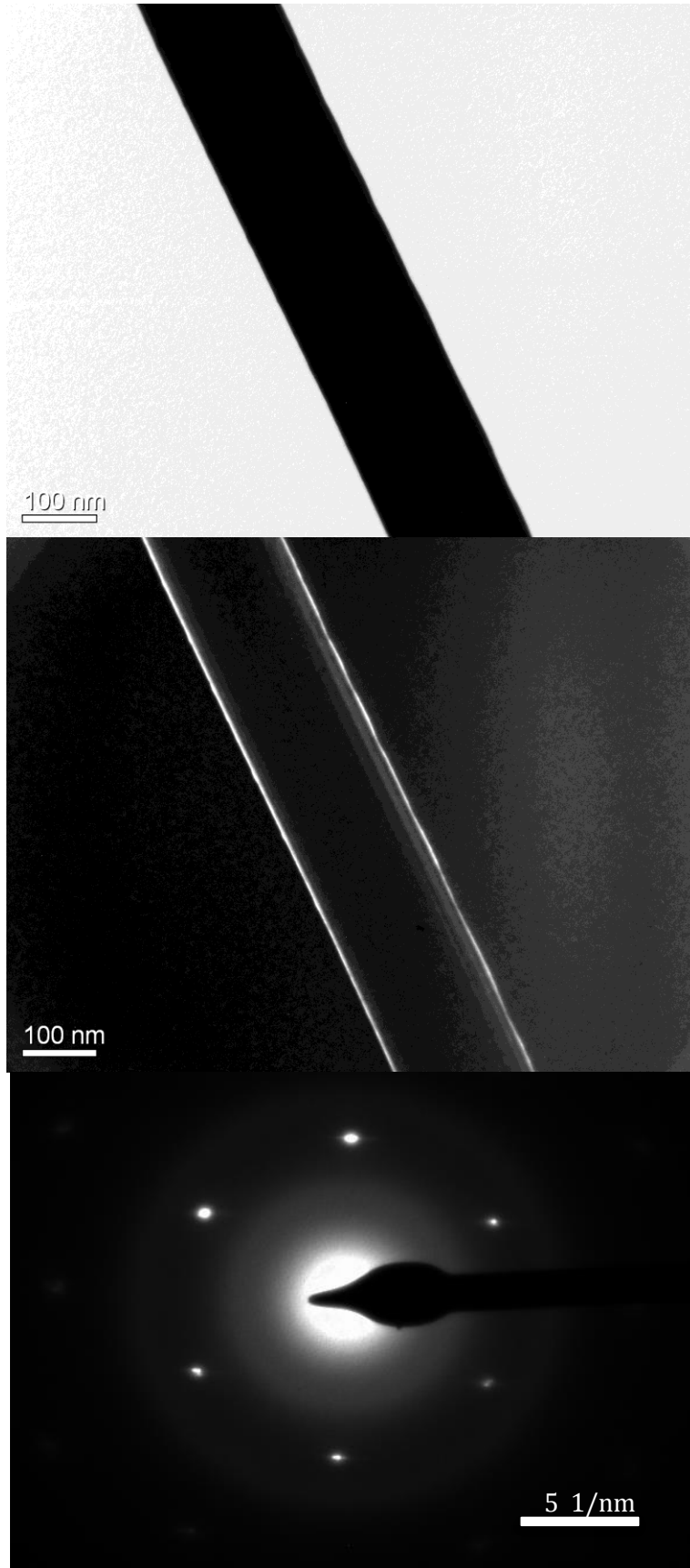


Figure 26: TEM images and the SAED diffraction pattern of the Ag-Au core shell nanowhisker

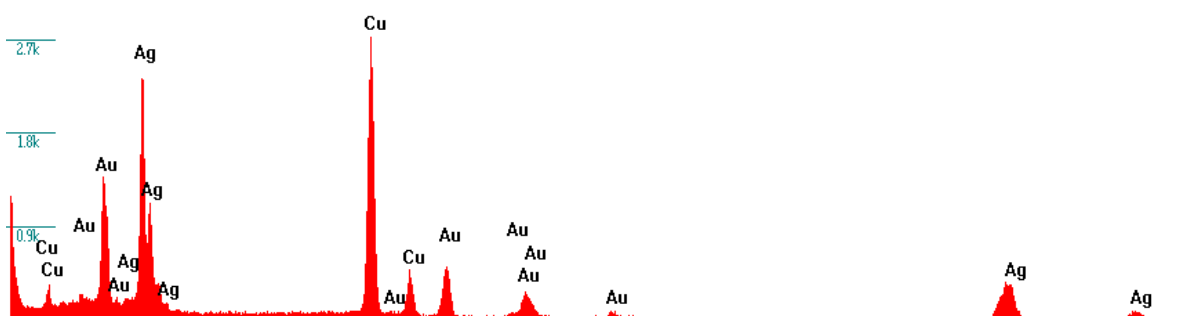


Figure 27: EDX spectrum of the Ag-Au core-shell nanowhisker in Figure 26

4.2 Characterization of Au Nanotubes

The analysis of hollow nanowhiskers obtained via annealing of Ag-Au core-shell structures showed a decrease of Ag content in the nanowhiskers and significant increase of Ag content on the polycrystalline film, which clearly indicates the diffusion of the Ag atoms from the whiskers into the film. The typical morphology of the nanotubes is shown in Figure 28 and the hollow structure can be seen in the image. The whisker, which is shown in the image, was annealed at 170⁰C for 30 min. The darker and the brighter regions represent the original cores-shell and the hollow regions, respectively. The diameter of the nanowhisker is 265 nm and the inclination angle to the substrate is 43⁰. The true length of the hollowed part of the nanowhiskers was 3.8 μ m and the details of the calculation method will be described later.

The bulk Kirkendall effect can result in formation of porous structure along the whole length of the nanowhisker because of rate of Ag diffusion in Au is faster than that of Au in Ag [14]. But it was not the case during the hollowing process studied in this work. The Ag content in the annealed nanowhiskers was measured in several spots chosen along the whiskers and the corresponding datas are shown in Figure 28. The Ag content in the lighter part of the whisker is around 10 at% Ag, while it is around 50 at% Ag in the darker part. Thus, the EDX analysis proves that Ag signal in the nanowhiskers decrease close to their root after annealing. This observation indicates that the nanowhiskers are starting to hollow at the root, and that Ag diffuses away from the nanowhiskers through their root.

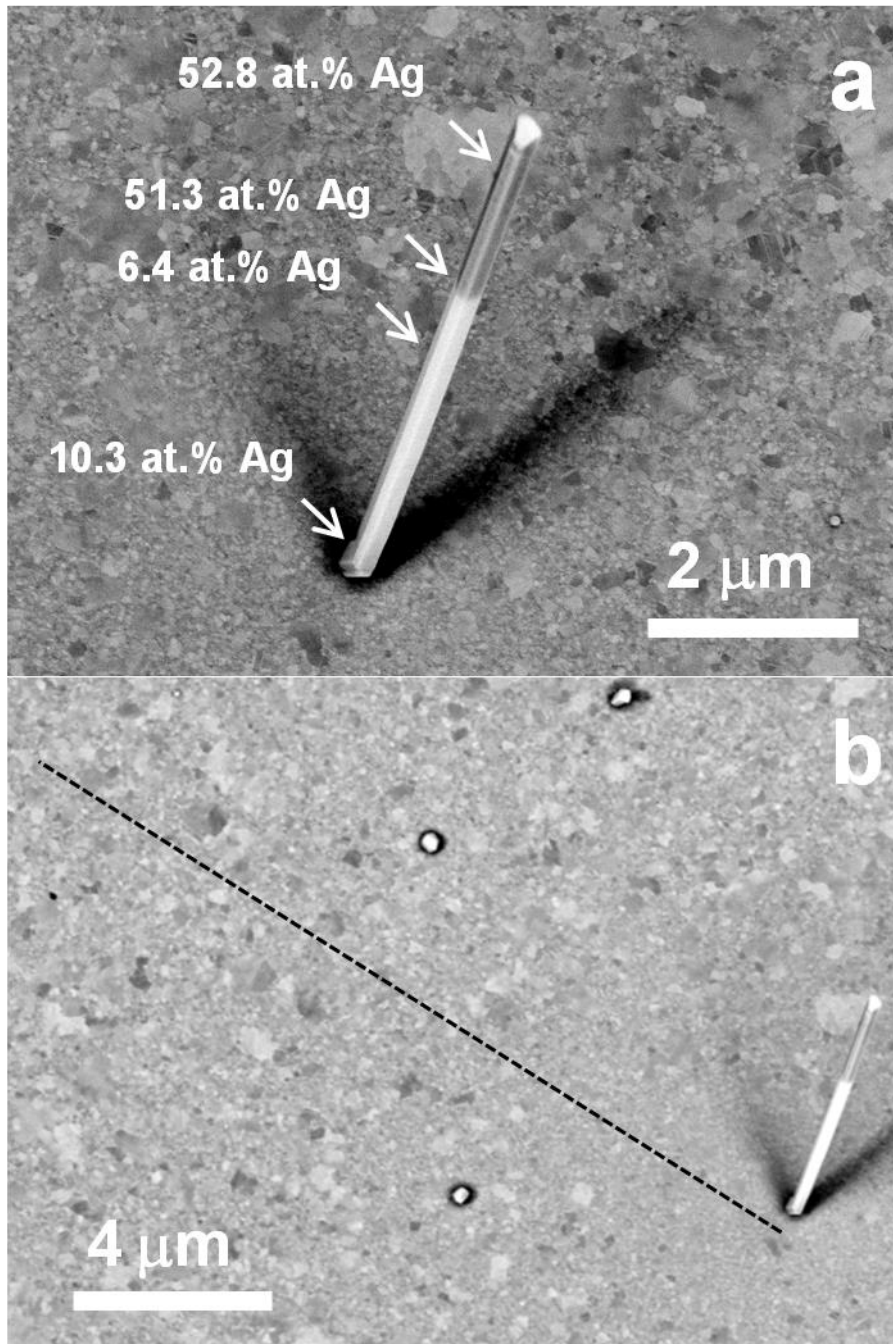


Figure 28: a) HRSEM image of the Ag-Au nanowhisker after annealing b) The Ag contents in the film, determined from the EDS spectra acquired at 10 kV

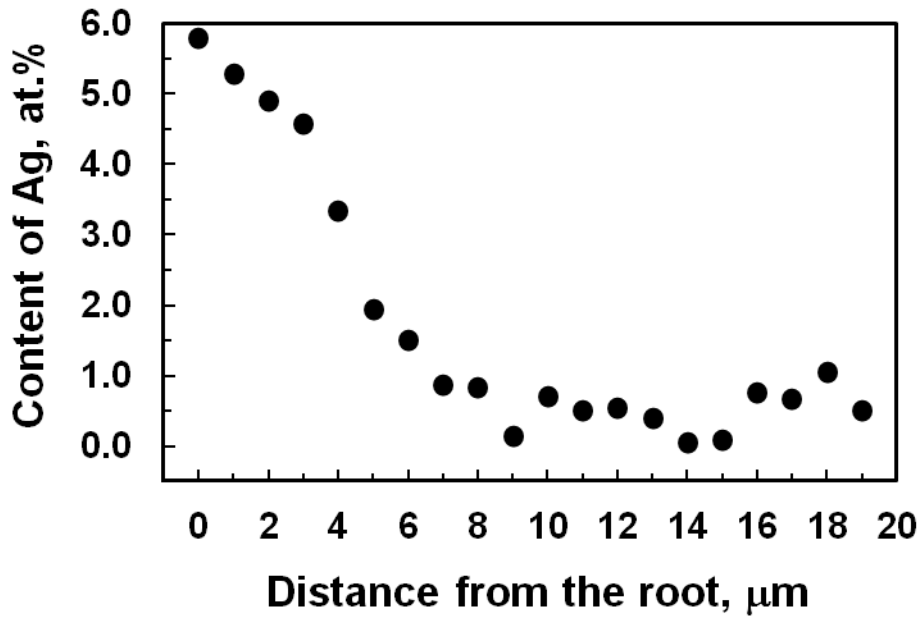


Figure 29: EDS concentration profile of the partially hollowed nanowhisker shown in Figure 28, acquired at 10 kV

It was observed that Ag signal appears in the film on the substrate after annealing, which indicates that Ag diffuses into the polycrystalline Au film. We performed the EDS analysis of the Ag distribution in the film. The concentration profile was taken along the film on the substrate in the vicinity of a whisker. It shows that the concentration of Ag decreases with increasing distance from the whisker root. The Ag concentration decreases approximately from 5at. % near the nanowhisker root to the 1at.% at a distance of 7 μm from the root. This means that Ag atoms are remaining in the vicinity of the nanowhisker root. It can be also seen that the average grain size in the Au film increases (seen in Figure 28b) with the increasing distance from the nanowhisker root, which also indicates the diffusion of Ag into the Au film. EDS line concentration profile taken along the nanowhisker and the HRSEM image of this partly hollowed nanowhisker are shown in Figure 30. The contrast difference in this hollowed nanowhisker is not as strong as the one in Figure 28. The partial hollowing of this whisker is confirmed by the quantitative EDS line profile analysis. The projected length of the hollowed section of the nanowhisker and its diameter are 2.3 μm and 275 nm, respectively.

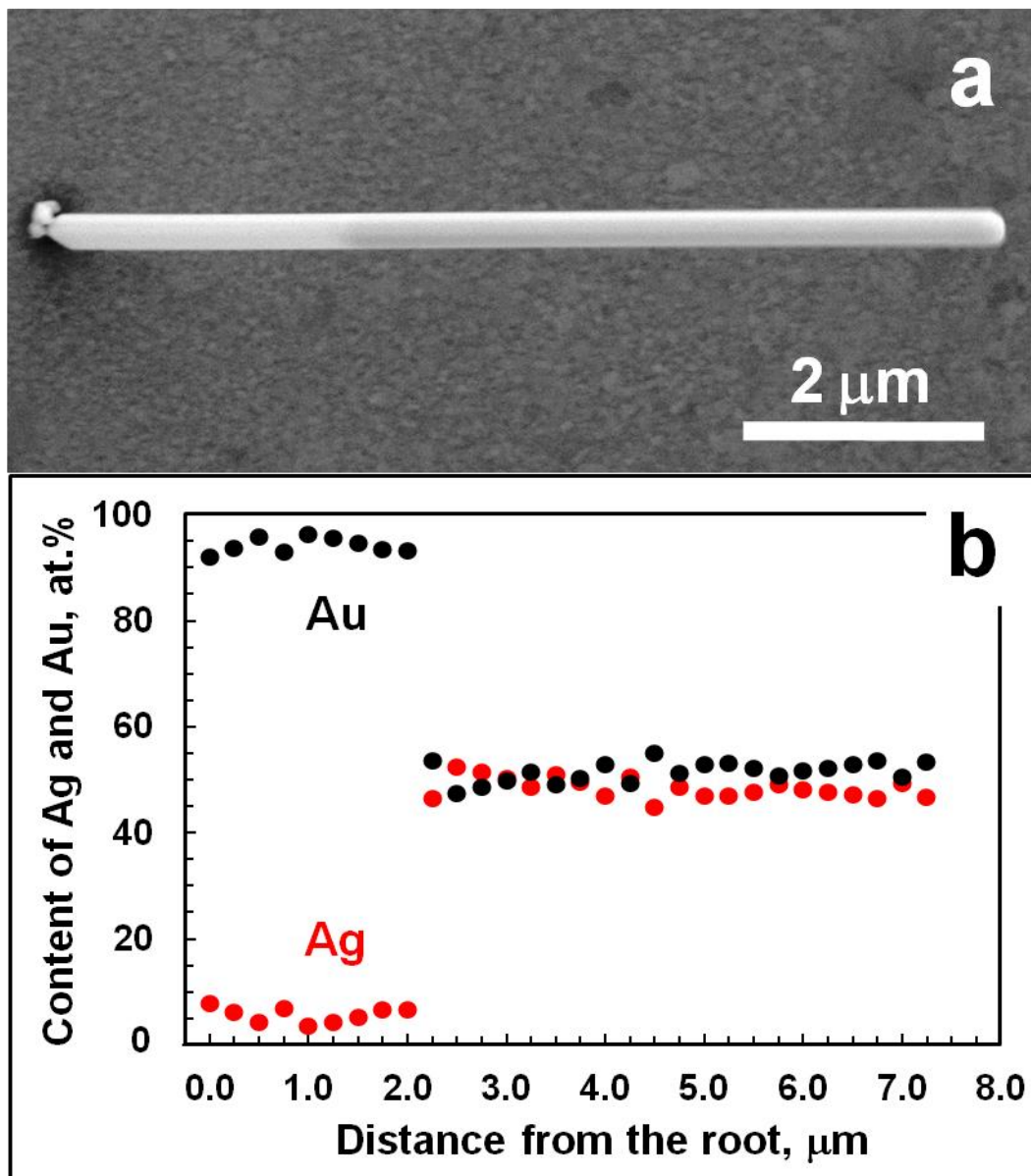


Figure 30: a) HRSEM image of Ag-Au nanowhisker after annealing at 170°C for 30 min b) EDS line profile taken along the nanowhisker at 10 kV

When the contrast differences between the filled and hollowed part of the nanowhisker is very weak because of the imaging conditions, the determination on the hollowing can be made via elemental EDS map. This is illustrated by another partly hollowed nanowhisker shown in Figure 31, which was annealed at 170°C for 20 min. The image in Figure 31a is the HRSEM image of the hollowed nanowhisker whereas Figure 31 b,c and d show the elemental map of Au, C and Ag respectively. As it is seen from the images, the whisker and the substrate is completely covered with Au (Figure 31b). The nanowhisker is partly hollowed since there is a Ag free part in the

Figure 31d. The bright mark which is seen in Figure 31d on the substrate arises due to the Ag diffusion into the polycrystalline Au film.

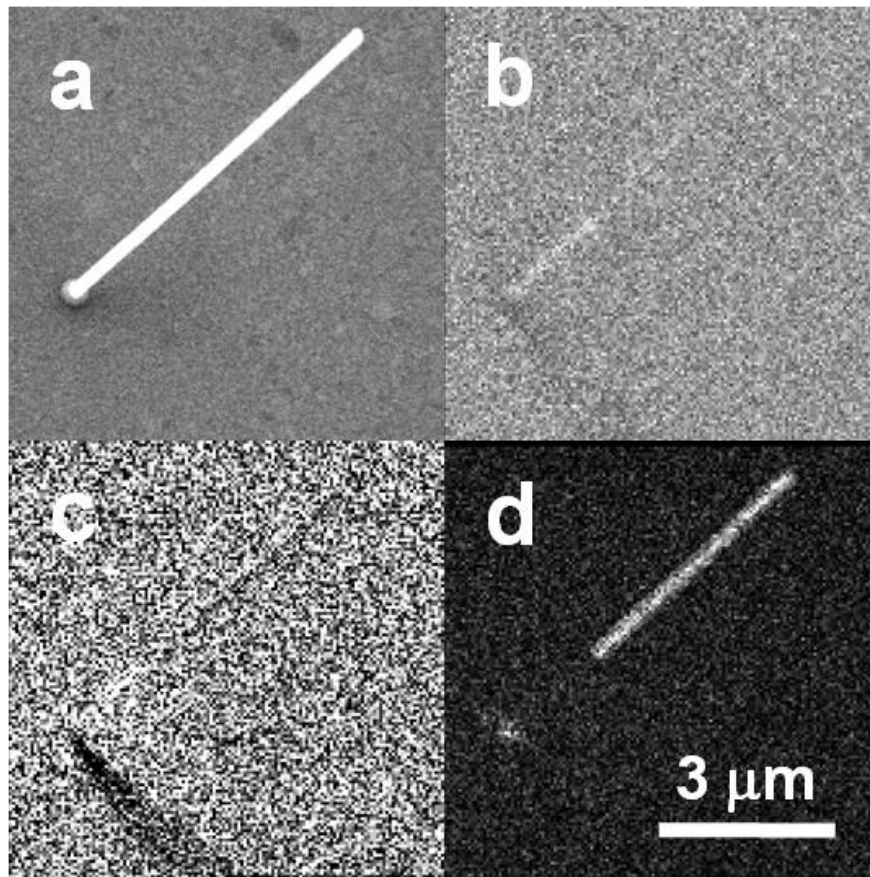


Figure 31: a) HRSEM image of partly hollowed nanowhisker after annealing at 170°C for 20 min, and the EDS elemental distribution maps acquired with b) AuM_{α1}, c) CK_{α1}, and d) AgL_{α1} X-ray radiation

To perform a quantitative analysis of hollowing kinetics of the Ag-Au nanowhiskers, the true length of the hollowed part of each analyzed nanowhisker (23 nanowhiskers), L , was calculated according to $L = L_p/\sin(\alpha)$. L_p is the projected length of the hollowed part, which can be determined either from the HRSEM images or by analyzing the EDS data. α is the inclination angle of the nanowhisker axis with respect to the surface normal. By taking into account the EDS composition maps (Figure 31 and Figure 32), a special procedure shown in Figure 33 was developed to estimate the inclination angle α .

During the measurement of the EDS composition maps of Au and Si, X-ray radiation arriving from the film to the detector is partially blocked by the nanowhiskers. Therefore, a characteristic shadow is created on the film which is marked as “3” in the

Figure 32. There is another shadow arising due to the physical shadowing during the deposition, which is marked as “2” in the same figure. This shadow is created during the Au shell deposition on the Ag core because of the shadowing effect of the Ag nanowhisker.

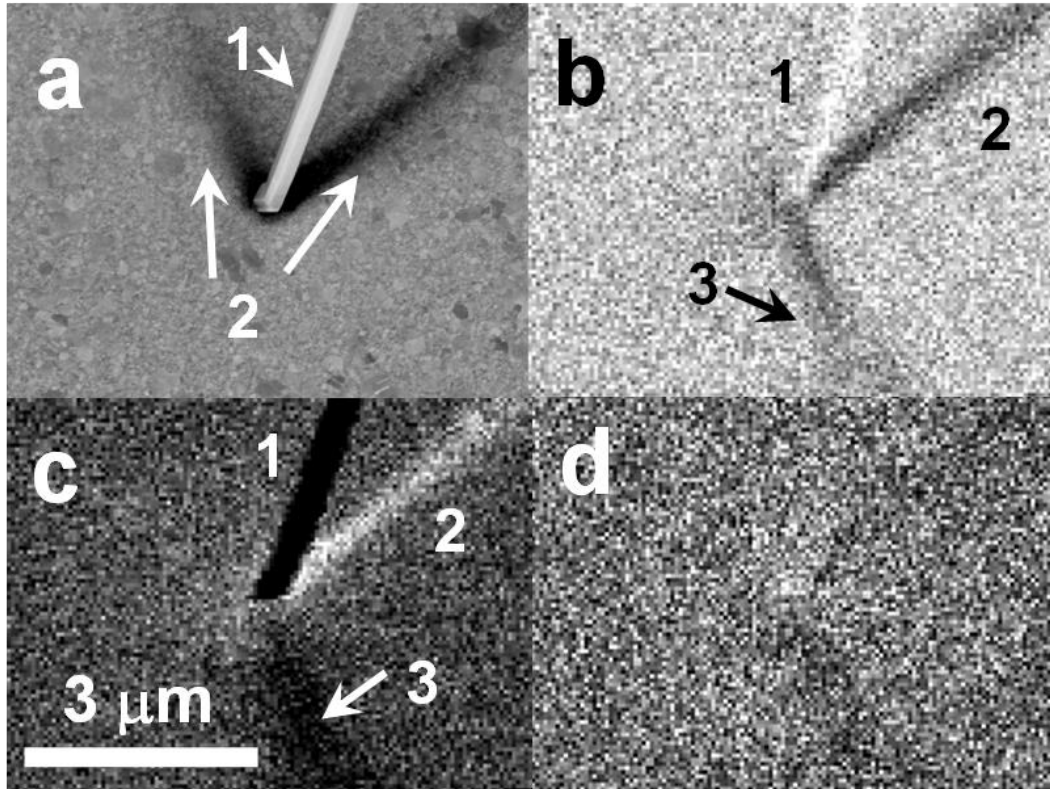


Figure 32: a) HRSEM image and EDS elemental maps acquired with b) $\text{AuM}_{\alpha 1}$, c) $\text{SiK}_{\alpha 1}$, and d) $\text{AgL}_{\alpha 1}$ radiation for the hollowed section of the nanowhisker annealed at 170°C for 30 min.: 1 – SE (a) and EDS (b-c) projection of the nanowhisker, 2 – Shadows of the nanowhisker formed during Au deposition by MBE, 3 – X-rays shadows formed due to a nanowhisker shadowing effect on the X ray radiation emitted by the substrate

The EDS shadow of each nanowhisker on the corresponding EDS elemental map and its projected image were used to determine the inclination angle α by using the following equation:

$$\alpha = \cot^{-1} \left(\frac{AB}{OA} \times \tan 35^{\circ} \right) \quad (10)$$

The take off angle of the X-ray radiation arriving at the EDS detector is 35° , that is why it is used in the equation. For example, the inclination angle, α , and the true length of the hollowed part, L , were calculated from the EDS and HRSEM data for

the nanowhiskers, which are shown in Figure 28 and Figure 31 (annealed for 30 and 20 min). The inclination angle and the true length for the nanowhisker were 43° and $3.8 \mu\text{m}$ for the one in Figure 28, and 44° and $2.6 \mu\text{m}$ for the one in Figure 31. The error of calculation of α was less than 3° , whereas the error of calculation of the true length of the hollowed part of the nanowhiskers was less than 10%.

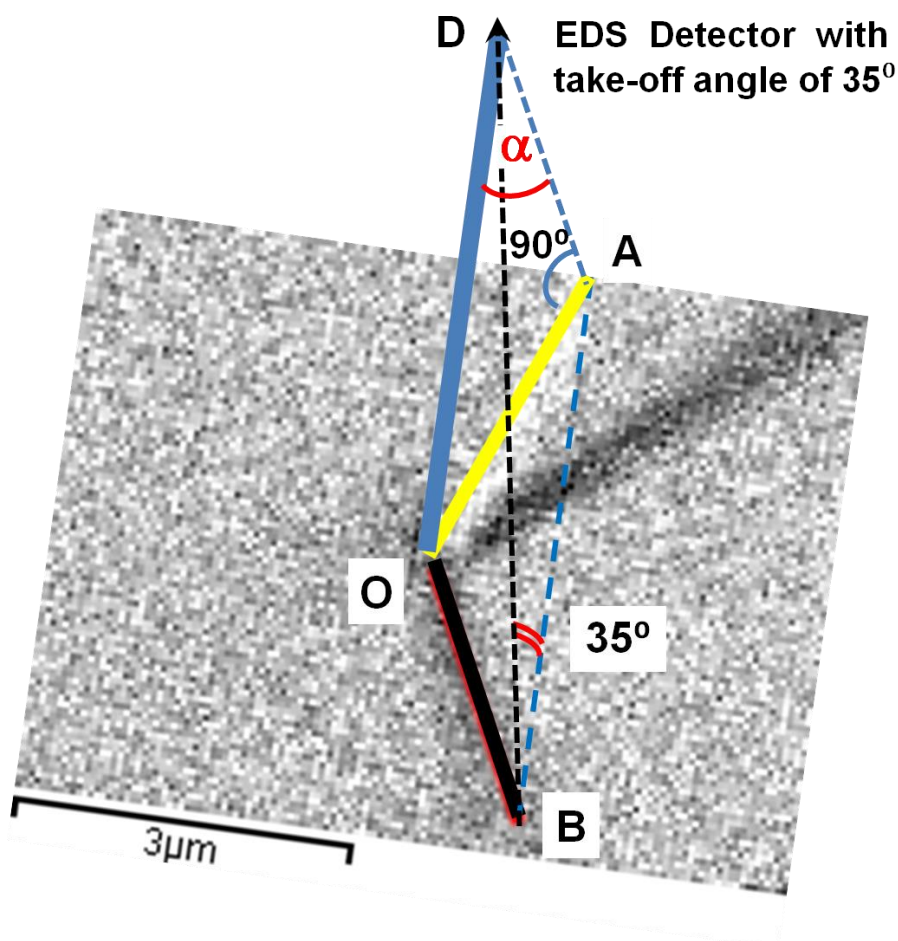


Figure 33: Schematic illustrating for the calculation of the inclination angle, α , of the Ag-Au nanowhisker with respect to the surface normal based on $\text{AuM}_{\alpha 1}$ EDS mapping: OD is a partially hollow nanowhisker with the inclination angle α with respect to the surface normal AD; OA its projected image acquired by backscattered electrons; OB is the nanowhisker shadow in $\text{AuM}_{\alpha 1}$ -radiation emitted by the film towards the EDS detector; AB is a substrate projection of the X-rays emitted from the film towards the EDS detector (D)

The dependence of the product of the true length of the hollowed part, L , and the internal radius of the nanowhisker, r , on annealing time is shown in Figure 34. The radius of the studied nanowhiskers varied from 65 to 185 nm (calculated based on the 35 nm Au wall thickness). This graph shows that the nanowhiskers hollow with a

constant rate. There is an inverse dependence of the hollowing rate on the nanowhisker radius.

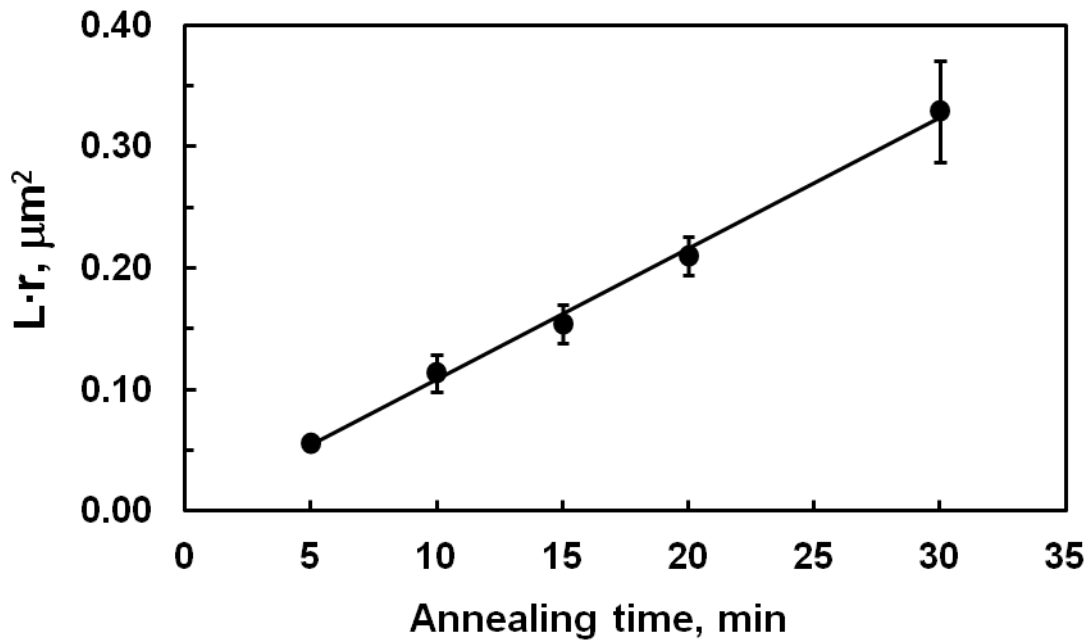


Figure 34: The dependence of the length of the hollowed region and the whisker radius of the product on annealing time

A cross sectional study of the hollowed nanowhisker which was annealed for 30 min and the substrate underneath of the nanowhisker was performed with the aid of STEM, see in Figure 35. The marks 1, 2 and 3 represent the Ag-free Au shell, layers of Si(100)/SiO₂/Si₃N₄/Carbon/Au(Ag) and Pt film around the nanowhisker which was deposited during FIB sample preparation. The layer, which is shown in the figure is Au film nearby the nanowhisker root. Therefore, there is also Ag because of the Ag out diffusion during the annealing.

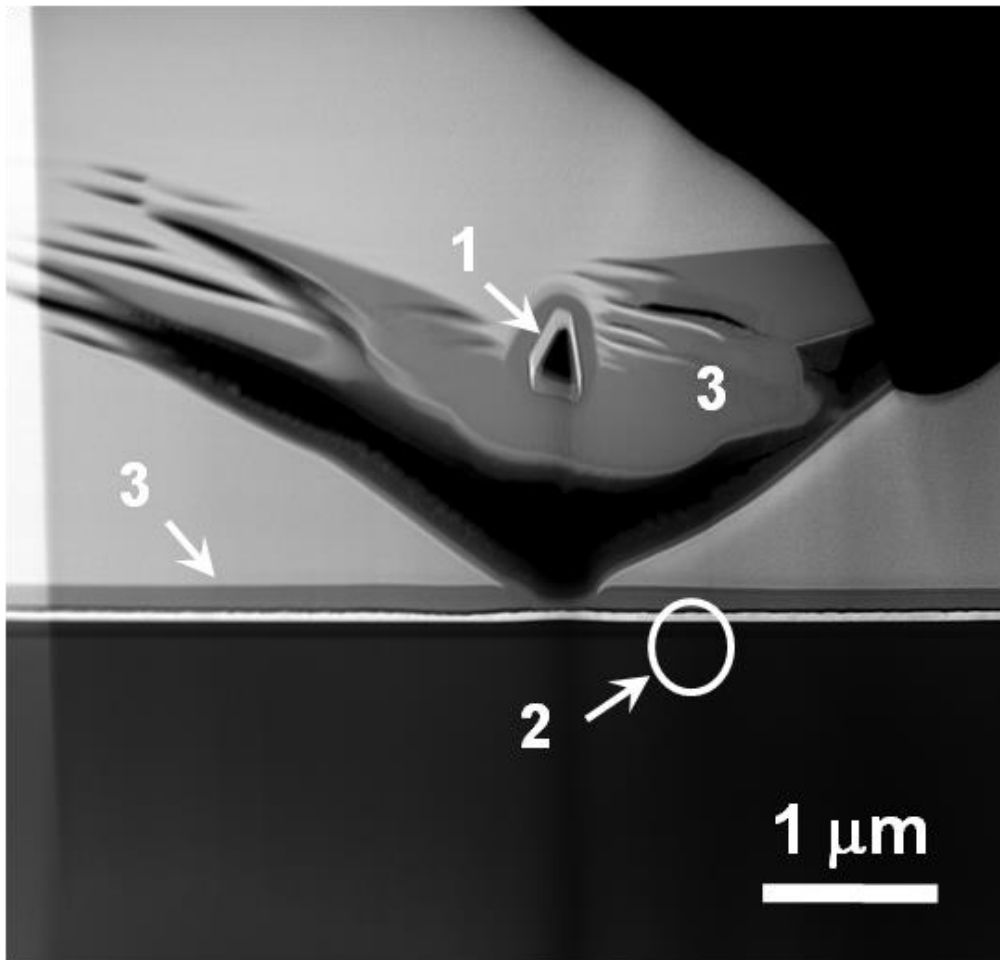


Figure 35: Cross-sectional high angle annular dark field (HAADF) STEM image of the partially hollowed nanowisker and of the nearby region of Au thin film

The higher magnification STEM cross-sectional micrograph of the hollowed nanowisker is presented in Figure 36. It can be clearly seen that the Au shell is faceted and has a uniform thickness. Thus it can be concluded that the hollowing process described in this thesis leads to the formation of stable and uniform Au nanotubes.

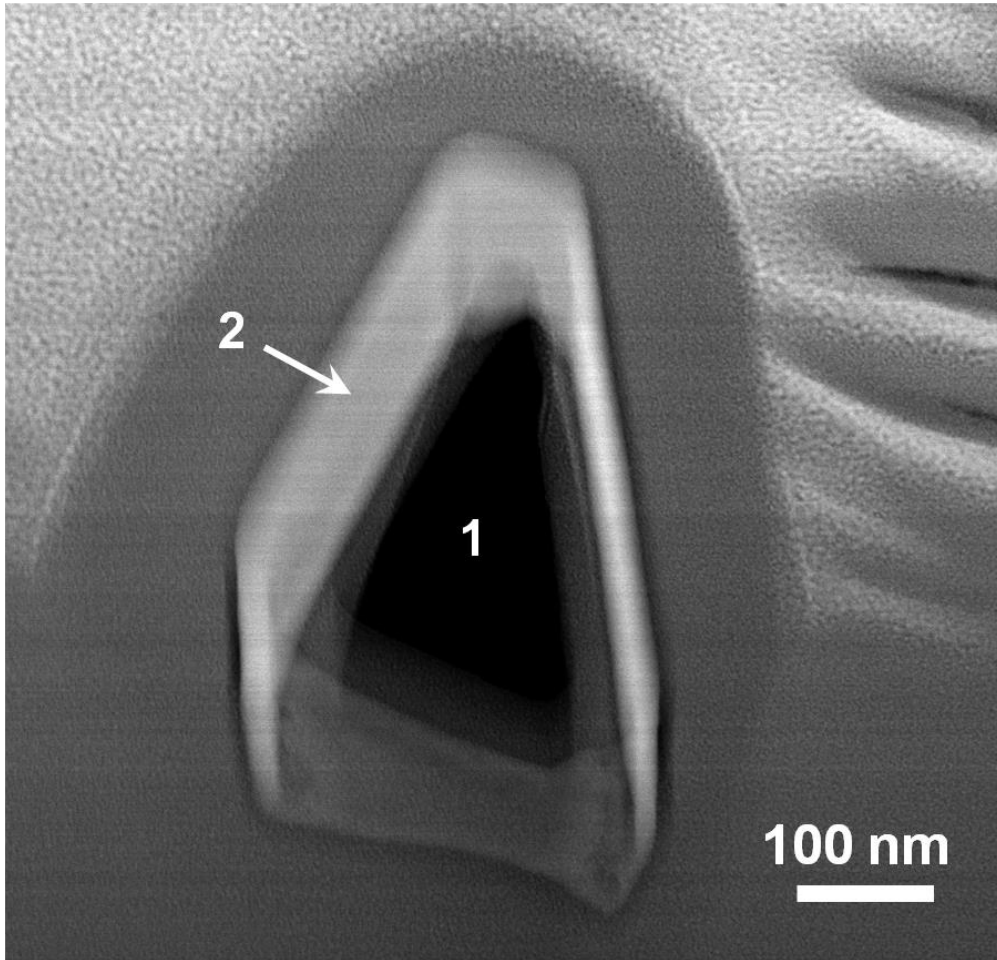


Figure 36: Cross-sectional HAADF STEM image of the hollowed nanowisker shown in Figure 35: 1-hollow Ag-free internal part of the nanowisker, 2 – Au all-around shell

The morphology of the Au(Ag) thin film in the close vicinity of the partially hollowed nanowisker is shown in Figure 37. The marks of 1, 2, 3 and 4 represents the 50 nm thick layer of SiO_2 on the Si(100) substrate, 50 nm thick layer of Si_3N_4 , 10 nm thick layer of amorphous carbon and 50-60 nm thick Au(Ag) film. The grain diameter varies in the range of 50-60 nm.

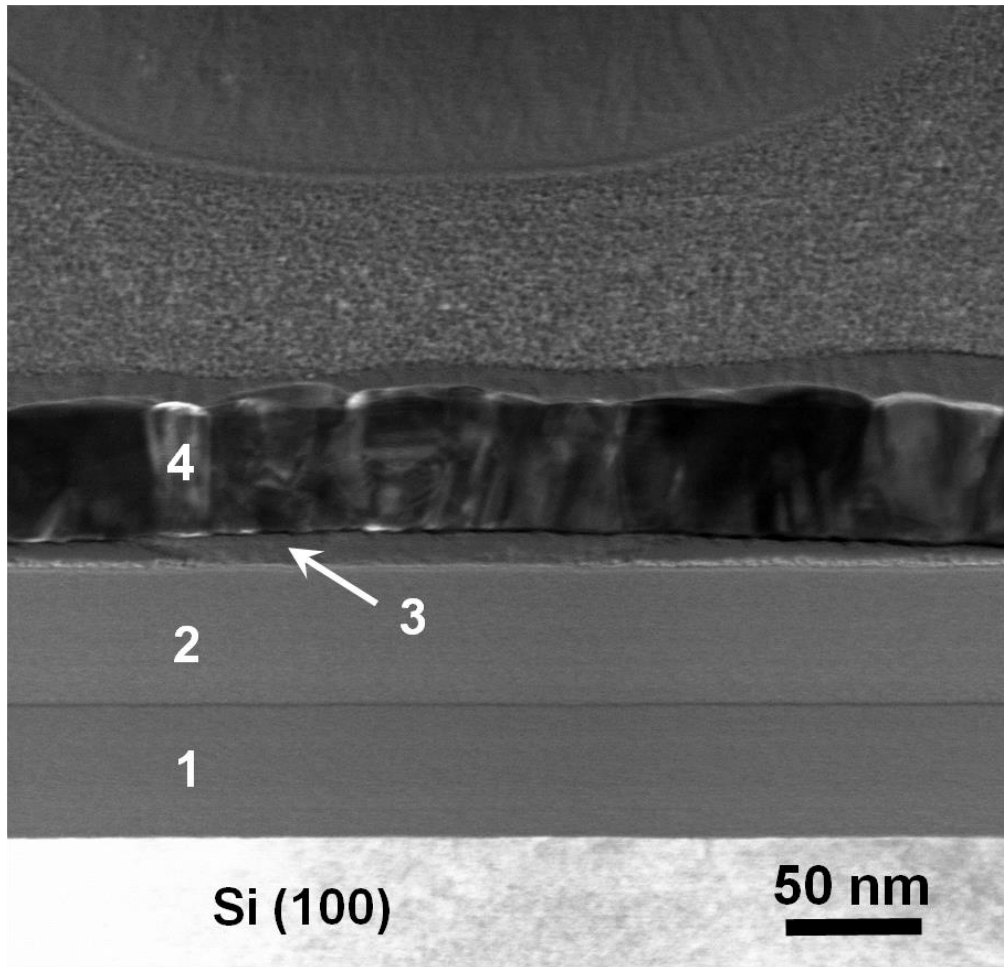


Figure 37: Cross-sectional bright field STEM image of the Au film in the vicinity of the nanowhisker shown in Fig. 9

The EDS compositional depth profile of the Au(Ag) thin film in the close vicinity of the same annealed nanowhisker is presented in Figure 38. The measurements were performed in the STEM/TEM mode across the film, which is shown in the cross-sectional bright field STEM image in Figure 37. The depth profiles were acquired at the distance of 1.5, 2.5 and 3.5 μm from the nanowhisker root. Peaks of Ag concentration can be clearly seen at the surface of the Au (Ag) film and at the film-carbon interface in the first depth profile taken at the distance of 1.5 μm from the nanowhisker. The surface peak of Ag concentration can be still seen at the distance of 2.5 μm from the nanowhisker, but not at the distance of 3.5 μm . Thus, the following conclusions can be drawn:

- i) The Ag content increases at the surface of the Au film and at the film-carbon interface which confirms the preferential short-circuit diffusion of Ag along the carbon-Au interface and along the Au surface.

ii) There is no significant bulk diffusion of Ag in the Au thin film.

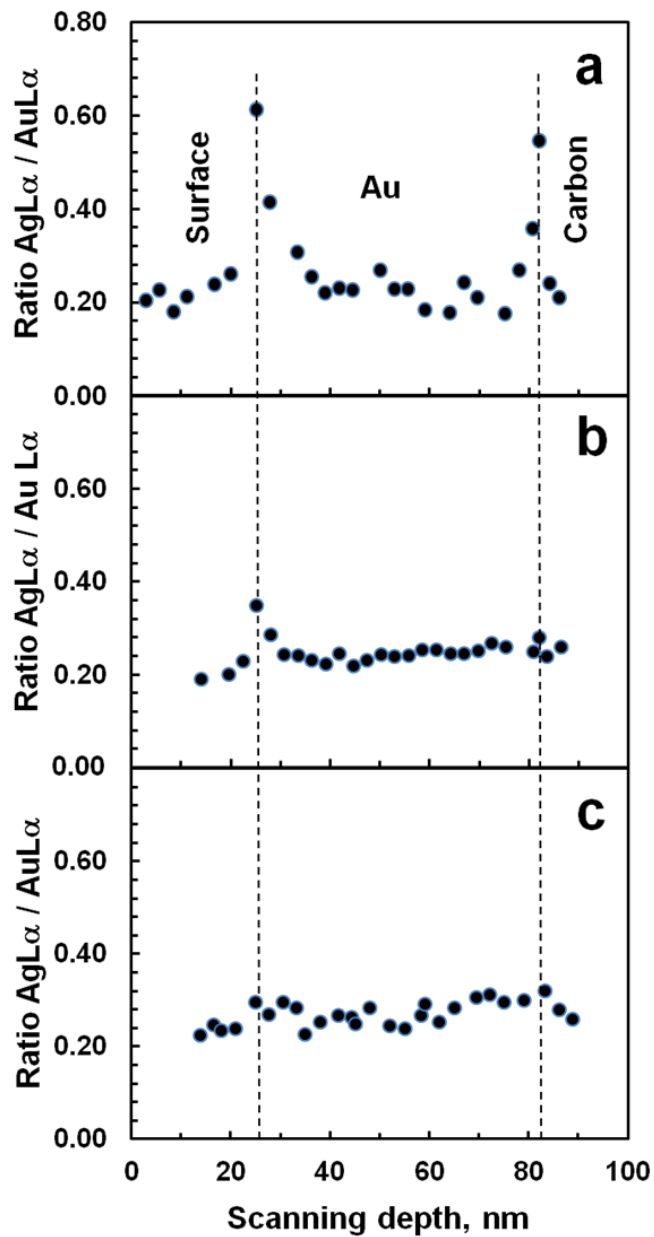


Figure 38: Depth profiles of AgL α and AuL α intensity ratios based on STEM measurements of the Au film at the distances of a) 1.5 μm , b) 2.5 μm , and c) 3.5 μm from the nanowhisker

No definite conclusion concerning GB diffusion can be drawn based on these profiles because the GBs in the cross-section TEM specimen are generally not in an edge-on position.

4.3 Kinetic Study and The Diffusion Model

The kinetic model of hollowing of the Au-Au core shell nanowhiskers was adapted from the paper published in 2014 [63].

According to present experimental results, the following model of nanowhiskers hollowing process, which is illustrated in the Figure 39, was formulated. The Ag atoms, from filled part of Ag core reach to the nanowhiskers root by diffusing along the internal surface of the growing Au nanotube. The process, which allows the transfer of Ag atoms from internal surface to the nearest grain boundaries in Au film is considered as a kinetic bottleneck. The Ag atoms which arrive at the grain boundaries in the Au film, diffuse away (in a radial direction) easily from the nanowhiskers. Since it is well known that the Ag solubility in carbon is negligible [64], Au-carbon interface can be considered as a reflection mirror for diffusing Ag atoms. Besides, the average diffusion length of Ag along the grain boundaries (GBs) in polycrystalline Au film exceeds the average grain size in the film (Figure 28 and Figure 29).

Under these conditions, the radial out-diffusion of Ag atoms along the Au film has to be understood in terms of Harrison's A-regime as a weighted average of the GB and surface diffusion [65]. The possible diffusion path between the internal surface of the growing Au nanotube and the nearest GBs in the Au film is the Au-carbon interface. The EDS analysis supports this hypothesis. A slight peak can be seen in the EDS spectra (Figure 31d and Figure 38), which indicates the Ag diffusion along the Au-carbon interface.

The diffusion process of Ag along the GBs of the Au film deserves a special attention. During the annealing procedure of the core-shell nanowhiskers, two processes occur at the same time, which are the diffusion of Ag atoms along the GBs, and the grain growth in the Au film. The average grain size in Au film in the vicinity of a nanowhisker increases with increasing distance from the nanowhisker root (see Figure 28). This is because of the reduction on the mobility of Au GBs enriched with Ag due to the solute drag effect [66]. Most of the atoms remain in the zone of fine grains of surrounding nanowhisker, as the total flux of Ag atoms is limited by the large grains region. The lateral size of this fine grain zone which is most likely formed

throughout the initial stage of hollowing, emerge as a result of an interaction between the GB diffusion and the concentration-dependent GB migration that are governed by independent kinetic constants [67].

An assumption will be made for the radius of this zone, R_0 . This radius, which will be taken as a parameter of the model, will be considered as a constant most of the times during the hollowing process. The EDS concentration profile in Figure 29 shows that most of Ag in the Au film is concentrated in the fine grain zone, which is in good agreement with the proposed hypothesis. The nanowhisker can be surrounded closely by Au-covered Ag particles or other nanowhiskers. When other structures are in the vicinity of the given whisker, the distance R_0 can be related to the average distance between the nanowhisker and neighbouring particles/nanowhiskers. The grain boundary and surface diffusion are presumed to be fast. This means that Ag atoms are distributed uniformly in the circular Au film zone of radius R_0 .

Moreover, it will be assumed that the surface self-diffusion of Ag along the meniscus of the receding Ag core and the Ag diffusion along the internal surface of the growing Au nanotube are very fast, and the corresponding gradients of chemical potentials of Ag atoms will be neglected. The reason for this is that surface diffusion is the fastest process in between all the involved diffusion types in the hollowing procedure [68]. The chemical potential μ_1 , of the Ag atoms located on the meniscus of receding Ag core is given by the following equation:

$$\mu_1 = \mu_{Ag}^0 - \frac{2\Delta\gamma}{r} \Omega \quad (11)$$

$$\Delta\gamma = \gamma_{Au} - \gamma_{int} \quad (12)$$

where γ_{Au} is the surface energy of Au and γ_{int} is the energy of coherent Au-Ag interface. μ_{Ag}^0 , Ω and r are the standard chemical potential of Ag in the bulk, the atomic volume of Ag and the internal radius of the Au nanotube, respectively. By considering the internal curvature of the Ag meniscus, Eq. (11) can be obtained when Young's equation is accepted to be valid at the triple line. The triple line is the meeting point of the internal surface of Au, Ag meniscus and Ag-Au interface. The Eq. (11) gives the average chemical potential of Ag atoms, even if Ag meniscus is faceted and Young condition is not fulfilled [69, 70]. In the approximation of an ideal

solid solution, the chemical potential of Ag atoms which enters from the Au-carbon interface to the grain boundary in the polycrystalline Au film, μ_2 , is given by:

$$\mu_2 = \mu_{b,Ag}^0 + kT \ln c_b - \gamma_{b,alloy} \omega_{Ag} \quad (13)$$

where $\mu_{b,Ag}^0$, c_b , $\gamma_{b,alloy}$ and ω_{Ag} are the standard chemical potential of Ag in the Au GB, the molar fraction of Ag in the Au GB, the energy of a GB in the Au film with a concentration c_b of Ag atoms, and the molar area of Ag atoms in the GB, respectively.

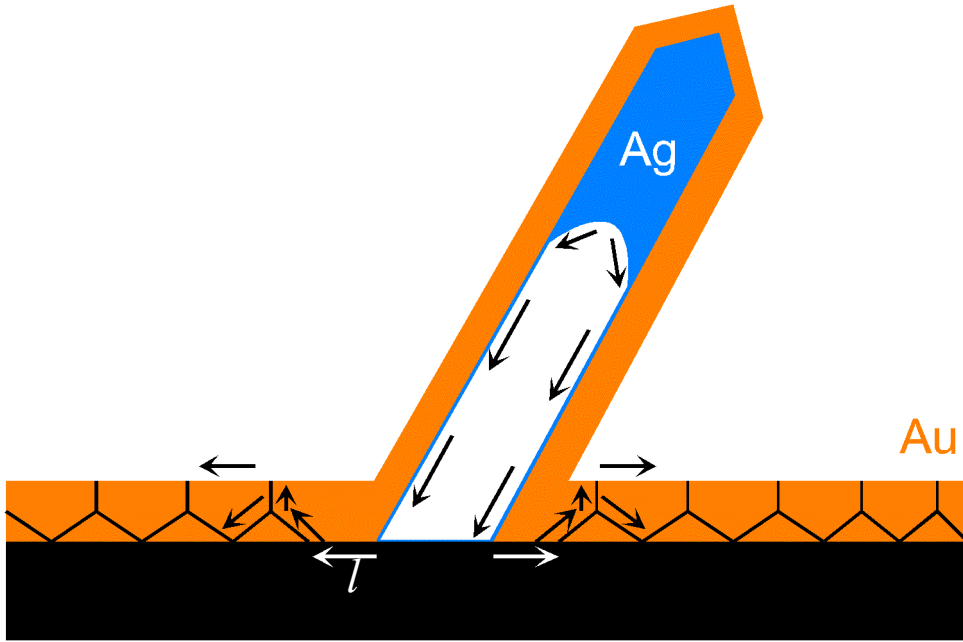


Figure 39: Schematic illustration of the Ag diffusion fluxes during the hollowing process. The Ag atoms leave the meniscus of the Ag core, diffuse along the internal walls of the growing Au nanotube, then diffuse along the Au-carbon interface and finally enter the GBs in the thin Au film. The GB diffusion of Ag is assisted by the diffusion along the film surface

The concentration c_b can be derived from the equation by using the condition of Ag mass conservation. According to this condition, the number of Ag atoms in the hollow core of Au nanotube is equal to the number of Ag atoms, which is distributed homogeneously in the GBs of Au film.

$$c_b = \frac{ur^2d}{2\delta_b R_0^2 h} - \frac{1}{2} \left[\frac{\delta_s}{\delta_b} \right] \left[\frac{d}{h} \right] c_s \quad (14)$$

where u , δ_b , d , and h are the height of the hollowed part of the nanowhisker, the thickness of the GBs in Au film (typically, 0.5 nm [68]), the average grain size in Au film and its thickness and δ_s and c_s are the thickness of the surface segregation layer and Ag concentration in it, respectively. The Ag atoms in the segregation layer on the surface of Au film are taken into account in the second part of the Eq.(14). In derivation of this equation, a simple square columnar grain morphology in the Au film was assumed, so that the volume fraction of the GB material in the Au film is $2\delta_b/d$. Then J , which is the total flux of Ag atoms along the Au-carbon interface, can be written down as follows:

$$J \approx \frac{D_i \delta}{kT\Omega} \frac{\mu_1 - \mu_2}{l} 2\pi r \quad (15)$$

where D_i is the diffusion coefficient of Ag atoms along the Au-carbon interface, and δ is the thickness of the interface diffusion layer. The diffusion distance along the Au-carbon interface is shown as the length l (in Figure 39) and it is considered to be much smaller than r , $l \ll r$. By taking the Eqs. (11) and (13) into account, the difference between μ_1 and μ_2 can be calculated only if the value for $\mu_{Ag}^0 - \mu_{b,Ag}^0$ is known. This difference of $\mu_{Ag}^0 - \mu_{b,Ag}^0$ can be estimated by considering the equilibrium segregation of Ag atoms at the GBs of an Ag-rich Au-Ag alloy ($c_b \rightarrow 1$). Also it should be accepted that atomic structure of the GB in the Au-Ag alloy is similar to the atomic structure of the GB in pure Ag.

$$\mu_{Ag}^0 - \mu_{b,Ag}^0 = -\gamma_{b,Ag} \omega_{Ag} \quad (16)$$

In this equation, $\gamma_{b,Ag}$ is the GB energy in pure Ag. The molar area of Ag atoms in the GBs was also assumed to be independent on composition. Taking into account the Eqs. of (11)-(16), the hollowing rate can be calculated by balancing the out-diffusion flux of Ag atoms with the rate of nanowhisker hollowing.

$$\frac{du}{dt} \approx \frac{2D_i \delta}{kTlr} \left\{ (\gamma_{b,alloy} - \gamma_{b,Ag}) \omega_{Ag} - \frac{2\Delta\gamma}{r} \Omega - kT \ln \left(\frac{ur^2 d}{2\delta_b R_0^2 h} - \frac{1}{2} \left(\frac{\delta_s}{\delta_b} \right) \left(\frac{d}{h} \right) c_s \right) \right\} \quad (17)$$

Estimating the first term of this equation is a difficult task since any data on the concentration dependence of the GB energy in Au-Ag alloys are lacking. A rough

estimation for $\gamma_{b,alloy} - \gamma_{b,Ag}$ can be made by $\gamma_{b,Au} - \gamma_{b,Ag}$, with $\gamma_{b,Au}$ being the GBs energy in pure Au. Since Au and Ag are chemically similar, the energies of structurally isomorphic GBs in Ag and Au are very close. According to the study of Udler and Seidman, the difference in the energies of structurally identical GBs in Au and Ag is less than 5 % [71]. It should be emphasized that $\gamma_{b,alloy}$ is the energy of the Ag-doped GB between two grains of pure Au. The main contribution to the differences $\gamma_{b,alloy} - \gamma_{b,Ag}$ is the excess energy connected with the Au-Ag interatomic bonds across the alloyed GB, which in turn scales with the mixing enthalpy of the solid Au-Ag alloys [72]. However, taking into account this contribution to the GB energy would require extending the current approach to the non-ideal (i.e. regular) solid solutions, adding the corresponding interaction terms to the RHS of Eq. (13). These two (i.e. GB energy and interaction) contributions would be added to the Eq. (13) with the opposite signs, and will most likely cancel each other. Thus, the first term in the braces on the RHS of Eq. (17) was neglected altogether in our estimations. The other two terms, which remains in the equation, present a competition between the surface/interface energy (the second term) and the entropy terms (the third term), which determines the tendency of nanowiskers for hollowing process. The entropy term represents the driving force for hollowing, while the energy term is related to the energy increase associated with the formation of a new Au surface during hollowing. The relative importance of these two terms in the experimental conditions of this study will be compared. The following parameters with the corresponding values will be used in our estimations: $r = 100$ nm, $u = 3$ μ m, $d = 50$ nm, $\delta_b = \delta_s = 0.5$ nm, $R_0 = 5$ μ m, $c_s = 1$ and $h = 50$ nm. With these values, Eq. (14) will give $c_b \approx 0.7$. It should be noted that with this GB concentration of Ag, the average bulk concentration of Ag in Au film will be somehow lower than the value determined by EDS in SEM which is ≈ 5 at.% of Ag. The explanation for this conflict can be made by additional contributions of the Ag-enriched interface layer to the EDS signal, as well as by slight GB migration during annealing which increases the effective thickness of the GBs. In any case, the estimated value of c_b can be considered as a lower bound for the Ag concentration in the GBs of Au film. The following values of surface and interface energy will be used to estimate the energy term: $\gamma_{Au} = 1.4$ J m⁻² [73] and $\gamma_{int} = 0.1$ J m⁻² [74]. By taking into account these values of parameters, the values of entropy and energy terms (at T=443 K) are calculated as

2.2×10^{-21} J per atom and 0.9×10^{-21} J per atom, respectively. This means that the entropy term dominates and the hollowing rate (i.e. the growth rate of a hollow Au nanotube at the expense of a core-shell nanowhisker) is positive. The competition between the energy and entropy terms imposes an upper limit, u_{\max} , on the length of the hollowed part of the nanowhisker:

$$u_{\max} = \frac{2\delta_b R_0^2 h}{r^2 d} \left\{ \exp\left(-\frac{2\Delta\gamma\Omega}{rkT}\right) + \frac{1}{2} \left(\frac{\delta_s}{\delta_b}\right) \left(\frac{d}{h}\right) c_s \right\} \quad (18)$$

Though the driving force loss related to the formation of a new Au surface increases with decreasing nanowhisker radius (see Eq. (11)), the entropy-related driving force gain increases too because fewer Ag atoms have to be distributed at the GBs in Au film. For the typical values of parameters mentioned above, u_{\max} changes from ≈ 3.6 to 250 μm with r decreasing from 100 to 10 nm, respectively.

Although the ordinary differential equation (Eq. (17)) is non-linear according to $u(t)$, for all values of u which are not too close to 0 and to u_{\max} the entropy term can be considered almost constant. In this case, du/dt scales as $1/r$, in accordance with experimental observations (see Figure 34). Neglecting the energy term altogether leads to the following estimation for the product of interface diffusion coefficient of Ag and the interface width:

$$D_i \delta \approx \frac{l \frac{d(ur)}{dt}}{2 \ln \left(\frac{ur^2 d}{2\delta_b R_0^2 h} - \frac{1}{2} \left(\frac{\delta_s}{\delta_b}\right) \left(\frac{d}{h}\right) c_s \right)} \quad (19)$$

Assuming $l = 35$ nm and employing the experimentally determined value of $d(ur)/dt \approx 1.75 \times 10^{-16} \text{ m}^2 \text{ s}^{-1}$ yields $D_i \delta \approx 8.5 \times 10^{-24} \text{ m}^3 \text{ s}^{-1}$ for the temperature of 170 $^\circ\text{C}$, which is close to the extrapolated product of radiotracer diffusion coefficient of Ag along the GBs in Au and the GB width at the same temperature [75]. Therefore, it can be concluded that either the diffusivity of the Au-carbon interface is similar to that of large-angle GBs in Au, or some of the GBs in the Au film grow through the epitaxial

Au layer on the Ag nanowhisker and reach to the Ag core. Moreover, some defects near the root of Ag nanowhiskers [17] may help the formation of a GB which is contacting to the Ag core during the deposition of Au film. In this case, these GBs play a role of kinetic “bottleneck” of the hollowing reaction, while the effective diffusivity of the Au film is dominated by the diffusion of Ag on the surface of the Au film. Unfortunately, the diffusion properties of metal–carbon and metal–ceramic interfaces are largely unknown, with available indirect estimations of the metal self-diffusion coefficient ranging from two orders of magnitude below the GB diffusivity for the Cu–SiC interface [76], to the values exceeding the surface diffusivity at the respective temperature for the Ni–sapphire interface [77]. Therefore, the conclusion about the similarity of diffusion properties of the GBs in Au and the Au–carbon interface is not unreasonable.

The effective diffusivity, D_{eff} ; can be roughly estimated based on the relationship $\sqrt{D_{eff}t} \approx R_0$, $D_{eff} \approx 1.4 \times 10^{-14} \text{ m}^2 \text{ s}^{-1}$, or $D_{eff}\delta \approx 7.0 \times 10^{-24} \text{ m}^3 \text{ s}^{-1}$. This value is close to the value of interface diffusivity $D_i\delta \approx 8.5 \times 10^{-24} \text{ m}^3 \text{ s}^{-1}$ obtained by using the Eq. (19). We believed that this is a pure coincidence, because the corresponding concentration profile along the film in Figure 29 is very different from the classical solution of the two-dimensional diffusion equation with cylindrical symmetry [78]. In addition, a simple mass balance based on this square-root estimation would yield the following kinetic law of hollowing: $\frac{du}{dt} \approx \frac{D_{eff}h}{r^2}$. In this case, the hollowing rate scales with the nanowhisker radius as $1/r^2$. This does not agree with the experimental result of $\frac{du}{dt} \propto \frac{1}{r}$. The latter law implies the presence of kinetic bottleneck at the root of the core–shell nanowhisker, i.e. of a single interface (either the Au–carbon interface or a large angle GB in Au) through which all the material from the nanowhisker core should be “squeezed” before fast spreading in the nanocrystalline Au film. The Ag-enriched zone of radius R_0 forms in the latter during the initial stages of annealing, and because of the contribution of surface diffusion, spreading of Ag in this zone is very fast.

The formation of hollow nanostructures leads to the increase in the total energy of all surfaces and interfaces in the system. This increase in energy is offset either by the chemical reaction at the surface [13], or by the formation of the solid solution in the bulk of the nanostructure [49]. The hollowing of Ag–Au core–shell nanowhiskers

observed in the present work occurred at a temperature (170 °C) at which any bulk interdiffusion in the Au–Ag system can be safely ruled out. Moreover, we even observed partial hollowing of the thinnest nanowhiskers in samples stored at room temperature for ≈ 3 months. This, together with the lack of any reactive components in the studied system, confirms the earlier hypothesis [17] that the Ag diffusion into the GBs of the Au film and the formation of the Au–Ag solid solution in the GBs is a driving force of the hollowing process. Though the role of surface, interface and GB diffusion in the formation of hollow nanostructures was acknowledged in the past [79], it was done merely in the context of mass transport paths to the reaction sites. The Au–Ag nanowhiskers studied in the present work is the first example of a system for which the formation of a two dimensional solid solution in the GBs is the driving force for the hollowing process. A kinetic model of hollowing was formulated based on the assumption that the outdiffusion of Ag atoms along the Au–carbon interface is the slowest link in the chain of kinetic processes responsible for hollowing. The model predicted that in the wide range of system parameters the rate of hollowing is constant and scales with nanowhisiker radius as $1/r$. This conclusion was in a good agreement with the experimental data. We would like to emphasize that the system microstructure in the vicinity of the nanowhisiker root is of critical importance. For example, if one or more fast-diffusivity GBs in the Au film directly connected the Ag core and the surface of the Au film, a direct fast outdiffusion path for Ag atoms would become available. This would make the interface diffusion unnecessary and accelerate the hollowing rate. It is possible that the nanowhiskers exhibiting some hollowing at room temperature belonged to this category.

In our analysis leading to Eq. (17) we did not take into account any elastic strain energy contribution to the chemical potential of atoms at the GBs. An influx of Ag atoms in the GBs of Au film should generate high bi-axial compressive stresses in the Au film and slow down the hollowing process to a full stop. Taking into account the diffusion of Au atoms in the direction opposite to the Ag diffusion flux (GB Kirkendall effect [80, 81] does not solve the problem because the number of Au atoms arriving at the nanowhisiker should be obviously smaller than the number of Ag atoms leaving it (in the opposite case the core–shell nanowhisiker would transform into Au nanowhisiker rather than into Au nanotube). We can roughly estimate the maximum biaxial elastic strain in the Au thin film due to hollowing, ε , assuming that

all Ag atoms from the nanowhisker core are incorporated in the GBs and employing the mass conservation condition:

$$\varepsilon \approx \frac{r^2 u}{2R_0^2 h} \quad (20)$$

which with the values of parameters employed in previous estimates yields $\varepsilon \approx 1.2\%$. This is a very high strain corresponding, for Au, to a bi-axial stress exceeding 800 MPa. Yet the same process of GB diffusion which drains Ag atoms from the nanowhiskers can also relax the bi-axial compressive stress in the Au film via outdiffusion of excess Au and Ag atoms to the surface of the film (wedge-like GB diffusion [82]). Again, a simple estimate based on mass conservation implies that the Au film thickness increase, Δh , which would accommodate all material, rejected by the nanowhisker and relax any compressive stresses building up in the film, is

$$\Delta h = \frac{r^2 u}{R_0^2} \quad (21)$$

which with parameters employed above yields $\Delta h \approx 1.2$ nm. This approximately corresponds to the film thickness increase of five monolayers. It should be emphasized that the characteristic length scale associated with stress relaxation corresponds to the film thickness, whereas the length scale related to the hollowing process is R_0 . Since $h \ll R_0$, the stress relaxation rate is much faster than the rate of stress build-up due to hollowing. Thus, it can be concluded that the hollowing process does not lead to any stress build-up in the Au film, and neglecting the contribution of elastic stresses in derivation of Eq. (17) was justified.

4.4 Characterization of Ag-Co and Ag- Pd nanowhiskers

Ag-Co and Ag-Pd core-shell nanowhiskers, which were produced by molecular beam epitaxy as described in the experimental section, were characterized by SEM, and the typical micrographies of these as grown samples are presented in Figure 40. It can be seen that the samples are very similar to the as-grown Ag-Au core-shell nanowhiskers. They are also composed of whiskers, islands and platelets. The diameter of the core-shell nanowhiskers is around 100 nm because the same Ag nanowhiskers were used as a template in all three material systems. The length of the nanowhiskers varies in the same range (between 4-25 μm) as in the case of Ag-Au

core-shell nanowhiskers. EDS elemental analysis confirmed that the whiskers are composed of Ag and Co in Ag-Co system, and of Ag and Pd in the Ag-Pd system, and there is no Ag in the film on the substrate in both material systems as expected.

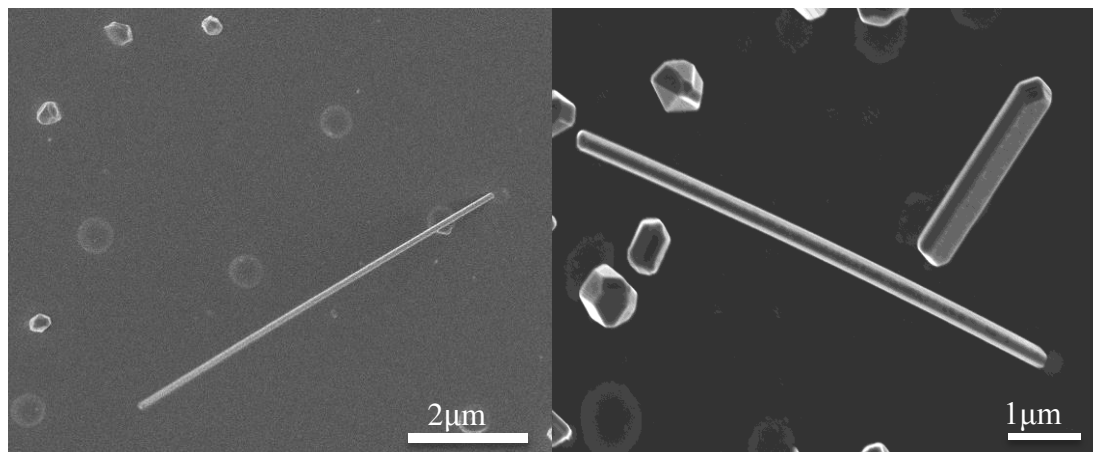


Figure 40: SEM images of a) Ag-Co and b) Ag-Pd core-shell nanowhiskers

Further characterization for the core-shell structures have been made by TEM and the result showed that they have the same microstructure as Ag-Au nanowhiskers. The nanowhiskers are perfect single crystals in both material systems as it was in Ag-Au core-shell nanostructures.

The bright field and the dark field images for Ag-Co nanowhiskers are shown in Figure 41. The nanowhiskers are straight and have a uniform diameter of approximately 100 nm. The diffraction pattern of Ag-Co nanowhisker is also seen in Figure 42. Based on the selected area electron diffraction (SAED) pattern of a single Ag-Co core-shell nanowhisker, it can be concluded that the Ag-Co core-shell nanowhiskers are single crystalline, whereas the Co film on the substrate between the whiskers is polycrystalline. The diffraction pattern can be indexed as face centered cubic (fcc) Ag and Co in [111] zone axis. In spite of a large lattice mismatch between Ag and Co (about 14 %), Co shell has grown epitaxially on Ag core. This is an exceptional epitaxial growth, which has been also reported in the literature for different metals which has a large lattice mismatch [83, 84]. It is known that if the thickness of the shell is below the critical thickness, the epitaxial growth is possible without the formation of dislocations (explained in section 2.2).

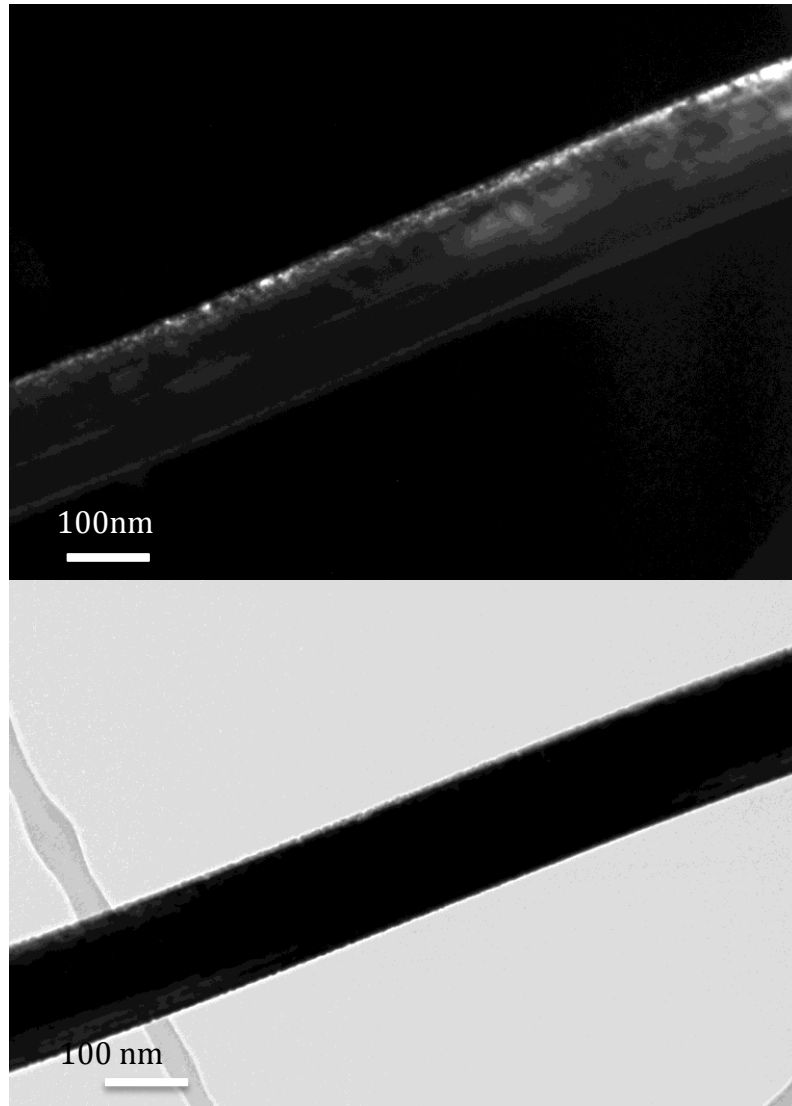


Figure 41: TEM images of the Ag-Co core shell nanowhisker

The diffraction spots arising from both materials are seen separately due to the large lattice mismatch. The spots in the blue circle represent the Ag core while the red circles stands for Co shell in the diffraction pattern. The theoretical indexing for fcc Co is also shown in Figure 42, which is fitting to the diffraction pattern. The spots in the middle are the forbidden reflections. Besides, some extra diffraction spots also appeared which are related to the oxide layer on top of the Co shell, which can be seen in the TEM images as well. The EDX spectrum of Ag-Co nanowhiskers taken by TEM confirms that the nanowhiskers are composed of Ag and Co, and the Cu signals arises from the grid, which was used as a TEM specimen holder.

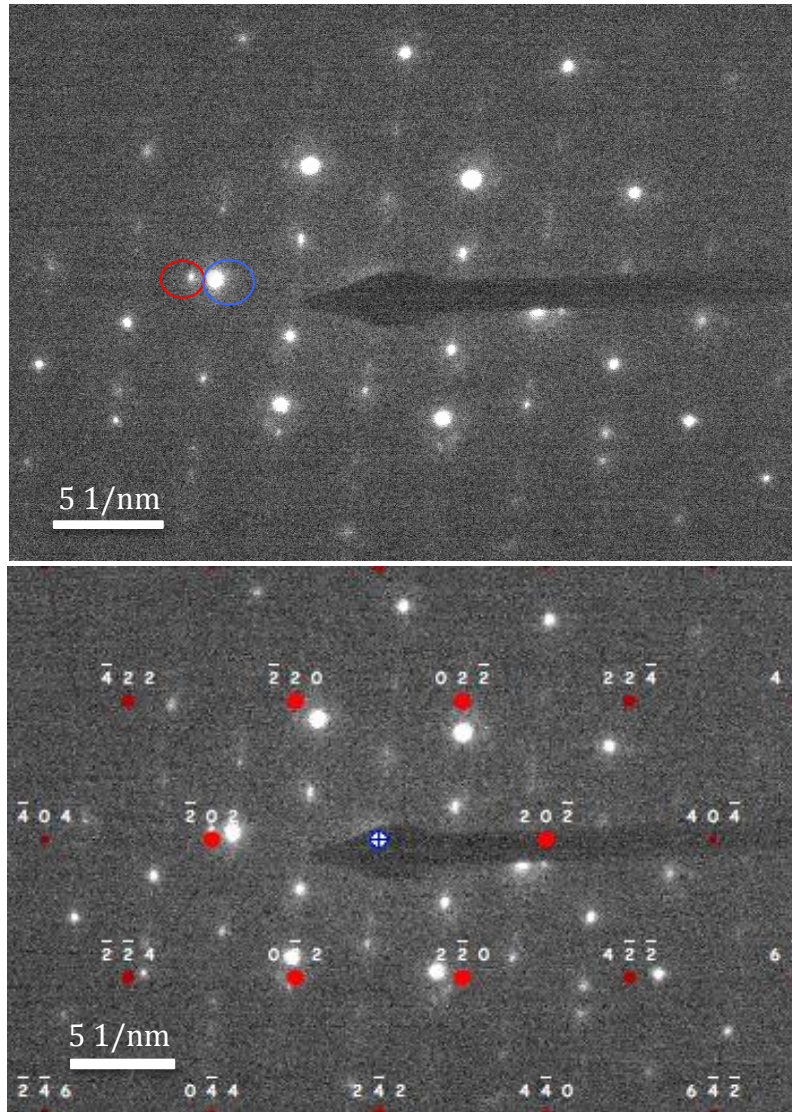


Figure 42: The SAED diffraction pattern and corresponding indexing of the Ag-Co core-shell nanowhisker

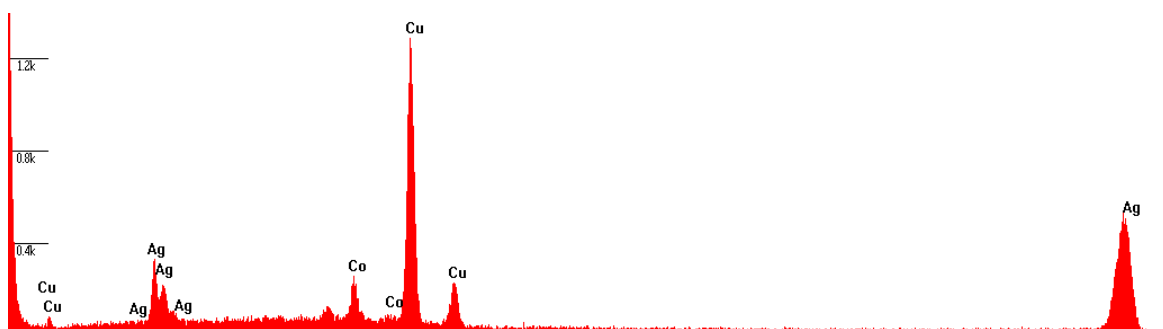


Figure 43: EDX spectrum of Ag-Co core-shell nanowhisker

Several studies have revealed that fine particles show different phase stability from their bulk specimens [85, 86]. It was found that the stable structure for Co at room

temperature depends on the grain size. When the grain size is very small (less than 30 nm) [87], then high temperature fcc phase for Co film remains stable at room temperature. Thus, the reason why Co shell has face centered cubic (fcc) crystal structure might also be related to the size effect.

Therefore, Co film in between the whiskers is also characterized by electron diffraction pattern of TEM. The TEM image and the corresponding diffraction pattern are seen in the Figure 44. The polycrystalline film has an average grain size of 20 nm. The presence of continuous diffraction rings is seen in the pattern, which shows the polycrystalline nature of the Co film. The strong diffraction rings correspond to the set of three rings. These are (01-10), (0002) and (01-11) planes, which show that the film is hexagonal close packed (hcp) phase of cobalt. The diffraction pattern shows also the presence of CoO. Since the film is hcp, the size effect does not play a role here. Thus, the fcc phase of Co shell would associated with the epitaxial relationship between the Ag and Co. A perfect alignment between the Co and Ag spots also supports the epitaxial growth.

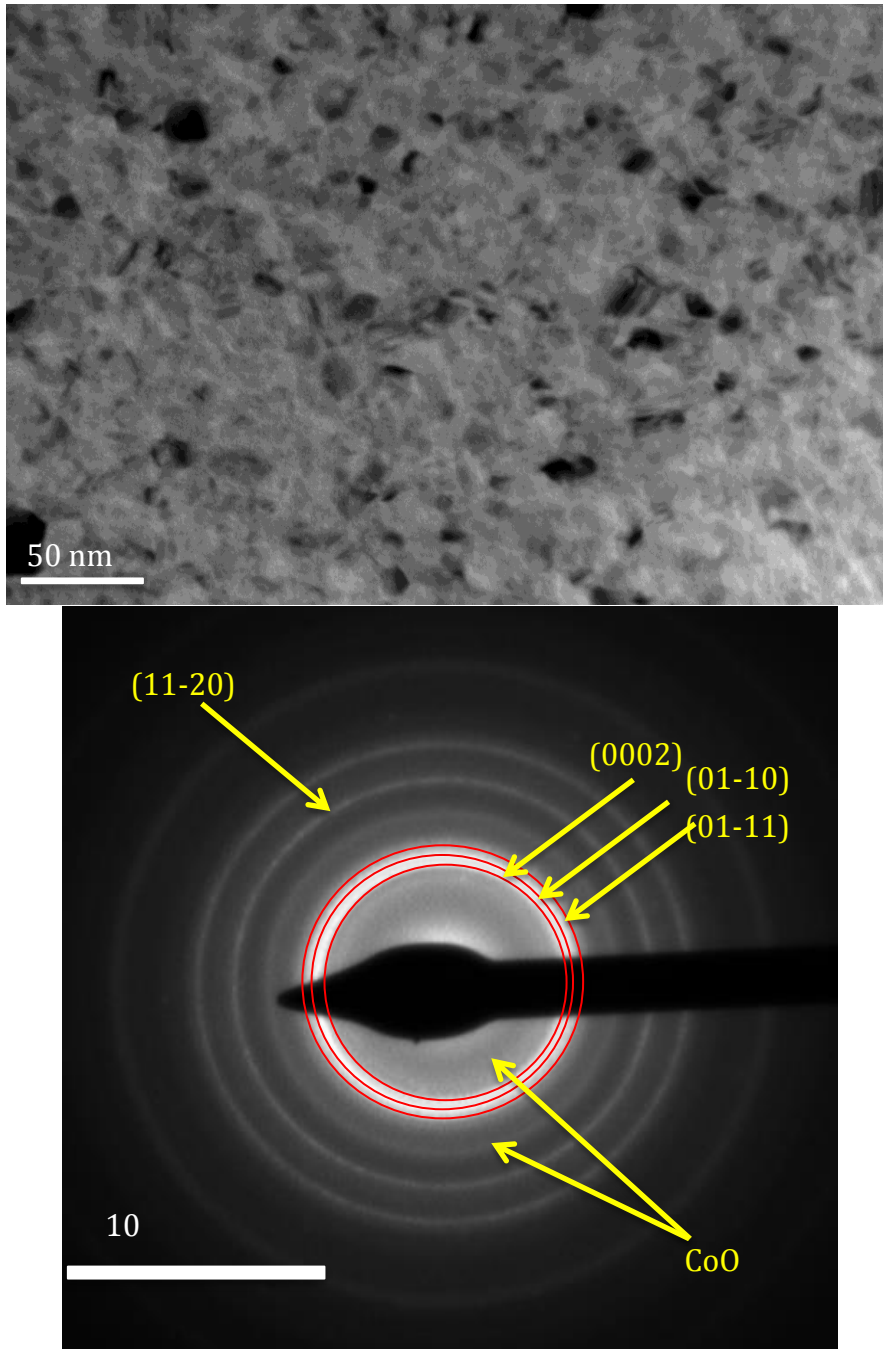


Figure 44: The TEM image and the diffraction pattern of the Co film

Further characterization has been made for Ag-Pd core-shell nanowhiskers as well. A single Ag-Pd nanowhisker was analyzed by TEM. The bright and dark field images with the corresponding selected area diffraction pattern are shown in Figure 45.

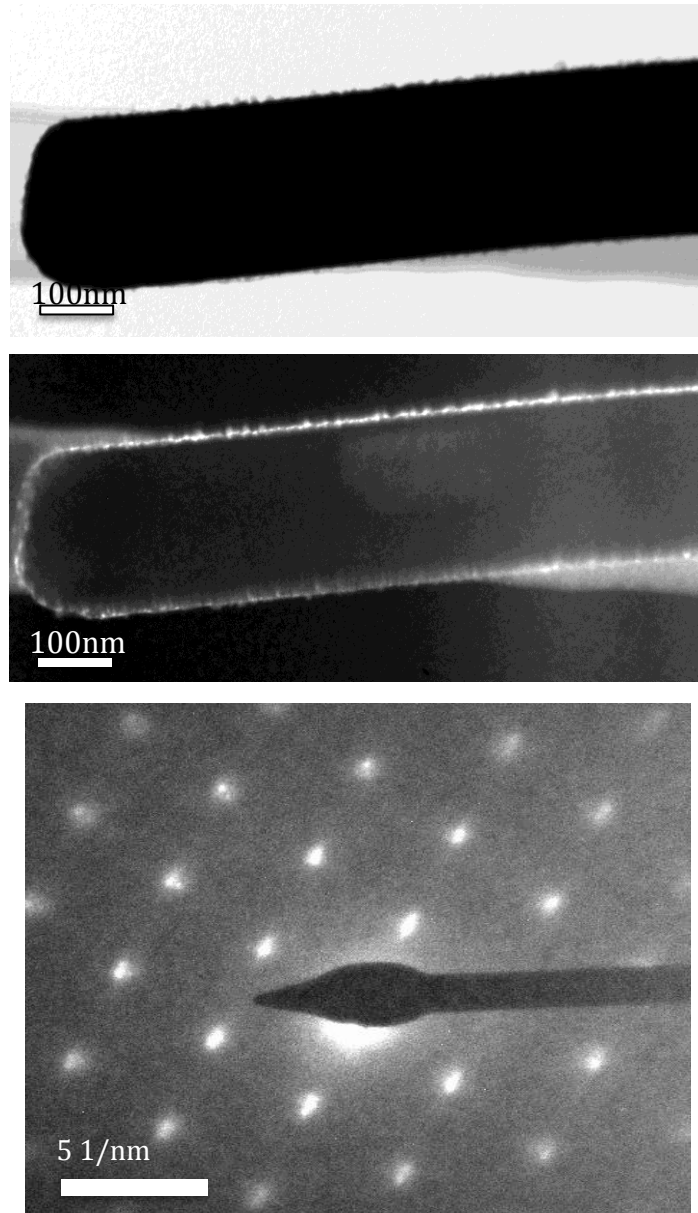


Figure 45: TEM images and the SAED diffraction pattern of the Ag-Pd core shell nanowhisker

The whiskers are straight with the diameter of about 200 nm. The single crystalline nature of Ag- Pd nanowhiskers is seen in the SAED diffraction pattern. The diffraction pattern can be indexed as face centered cubic (fcc) Ag and Pd in the [011] zone axis.. The lattice mismatch between the two metal is around 4%. The results from the diffraction pattern indicate that the Pd shell was formed epitaxially on the Ag core and the spots are overlapped.

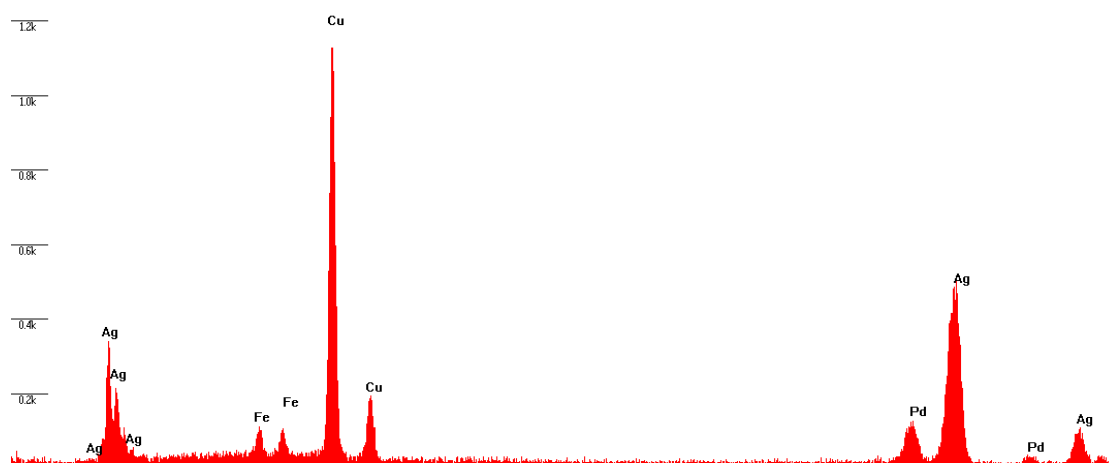


Figure 46: EDX spectrum of Ag-Pd core-shell nanowhisker

The EDX spectrum (Figure 46) taken by TEM shows that the nanowhiskers are composed of Ag and Pd. According to the results, the as-grown samples are formed by single crystalline Ag-Pd nanowhiskers and polycrystalline Pd film in between. According to our diffusion model this means that the hollowing is possible in these systems.

4.5 Characterization of Co and Pd Nanotubes

As it was already discussed, the two material systems of Ag-Co and Ag-Pd exhibit the microstructures identical to those of Ag-Au. Thus, according to our model the hollowing is possible in these systems, too.

The Ag-Co core-shell nanowhiskers were annealed at 350⁰ C for 30 min. The HRSEM image of the annealed Ag-Co nanowhisker is seen in the Figure 47 with the corresponding EDX data. The result indicates that the nanowhisker is partially hollowed. The contrast differences between the filled and the hollowed part of the whiskers can be seen in the image. The Ag content measured from the two spots on the nanowhisker by EDX shows lower Ag concentration in the root.

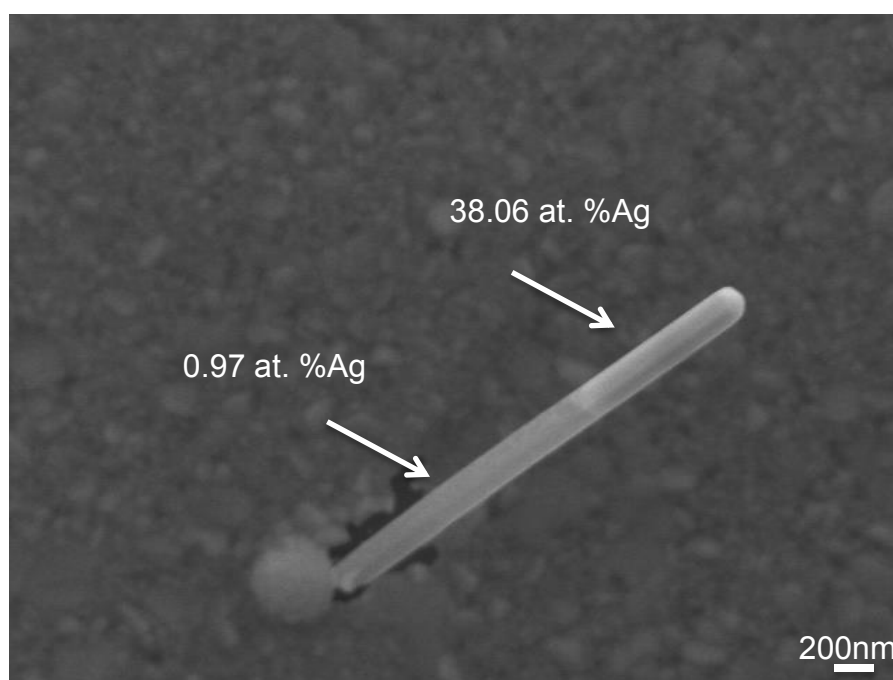


Figure 47: The SEM images of the hollowed Ag-Co nanowhisker

We adapted the diffusion model formulated for the Ag-Au core-shell structures to the Ag-Co core-shell system, in order to compare the hollowing rates. The concentration of Ag in the Co grain boundary will be calculated from the Eq.(14), with all the parameters employed for Co.

The following parameters were estimated in order to calculate the concentration: $r = 100 \text{ nm}$, $u = 3 \text{ }\mu\text{m}$, $d=20 \text{ nm}$, $\delta_b=\delta_s=0.5 \text{ nm}$, $R_0=5 \text{ }\mu\text{m}$, $c_s =1$ and $h = 50 \text{ nm}$. The Ag

concentration in the segregation layer, c_s is assumed to be 1, since the surface energy of Co (2.5 J/m^2) is much higher than the surface energy of Ag (1.2 J/m^2) [88]. With these values, c_b will be 0.7.

The rate of Co nanowisker hollowing will be calculated with the Eq. (17). In this equation, D_i is the diffusion coefficient of Ag atoms along the Co-carbon interface. Unfortunately, the diffusion properties of Co-carbon interface are unknown, therefore we used the result which was found in our model for Ag-Co material system. This result tells us that the diffusivity of Au-carbon interface is similar to that of the GBs in Au film. Thus, D_i is accepted as the diffusion coefficient of Ag along the GBs in Co, instead of the diffusion coefficient of Ag along the Co-carbon interface. It is given as follow [89];

$$D_i = 1 \times 10^{-8} e^{\left(-\frac{0.46 \text{ eV}}{kT}\right)} \quad (22)$$

which yields to $1.89 \times 10^{-16} \text{ m}^2/\text{s}$ for the temperature of $350 \text{ }^\circ\text{C}$. The interface width was accepted as 0.5 nm , so that;

$$D_i \delta = 9.5 \times 10^{-26} \text{ m}^3/\text{s} \quad (23)$$

The term $\Delta\gamma$ in here is given as;

$$\Delta\gamma = \gamma_{Co} - \gamma_{int} \quad (24)$$

Where the γ_{Co} and γ_{int} are the surface energy of Co and the interface energy of Co-Ag, respectively. The following values will be used for these parameters: $\gamma_{Co} = 2.5 \text{ J/m}^2$ and $\gamma_{int} = 0.6 \text{ J/m}^2$ [88, 90]. Although there might be oxide layer on the Co film, this almost does not change the rate. Thus the surface energy of Co is used for calculation.

The first term, $\gamma_{b,alloy} - \gamma_{b,Ag}$ is very difficult to estimate as it was mentioned. It was neglected on our model for Au nanotubes, since Ag and Au are chemically quite similar and their grain boundary energies are very close to each other. Unfortunately this term can not be neglected for Co nanotubes. Instead of using the GB energy in Ag-Co alloy the GB energy of Co was used for $\gamma_{b,alloy}$. To calculate the molar area of Ag atoms in the GBs, ω_{Ag} , following equation were used:

$$\omega_{Ag} = \frac{\delta_b d}{c_b} \quad (25)$$

With all these information, the hollowing rate $\frac{du}{dt}$ were calculated as 254 nm/s for Co and 0.8 nm/s for Au nanotubes. The hollowing rate of Co nanotubes is found to be much higher than that of Au nanotubes.

If the first term were neglected as it was in the case of Au nanotubes, still the rate would be positive because of the entropy term, which is the driving force for hollowing. Thus the hollowing would still occur, but the rate (0.01 nm/s) would be lower than in the case of Au nanotubes. To obtain the same rate with the Au nanotubes, the GB energy of the alloy should be 0.377 J/m², which is almost same as the GB energy of Ag.

On the other hand, if the GB energy of the alloy in Ag-Au material system was not neglected and the GB energy of Au would be used instead, then the hollowing rate for Au nanotubes would be 222 nm/s, almost same as the one for Co.

If the diffusion coefficient of Ag in the Co-carbon interface were considered different (lets assume two orders of magnitude) than in the Co, the rate would change as well but still would be positive.

Depending on the GB energy of the alloy or the diffusivity in Co-carbon interface, the rate would change. But in any of these cases, the hollowing rate of Co nanotubes is positive and comparable with the hollowing rate of Au nanotubes.

The Ag-Pd nanowhiskers were annealed at 170⁰ C for 30 min, and the HRSEM images with the corresponding EDX spectrum are presented in the Figure 48. The strong contrast differences between the two parts of the nanowhiskers can be easily seen. The darker part is the Ag free part whereas the lighter part is the filled part. The EDX spectrum also confirms the hollowing process. The hollowed part marked as “1” and the corresponding EDX spectrum shows the Ag decrease. The mark “2” shows the filled part which can be confirmed by EDX spectra. According to the HRSEM images with the corresponding EDX data, it was observed that Co and Pd nanotubes were successfully produced by employing the same diffusion based method, which was developed for the Ag-Au system.

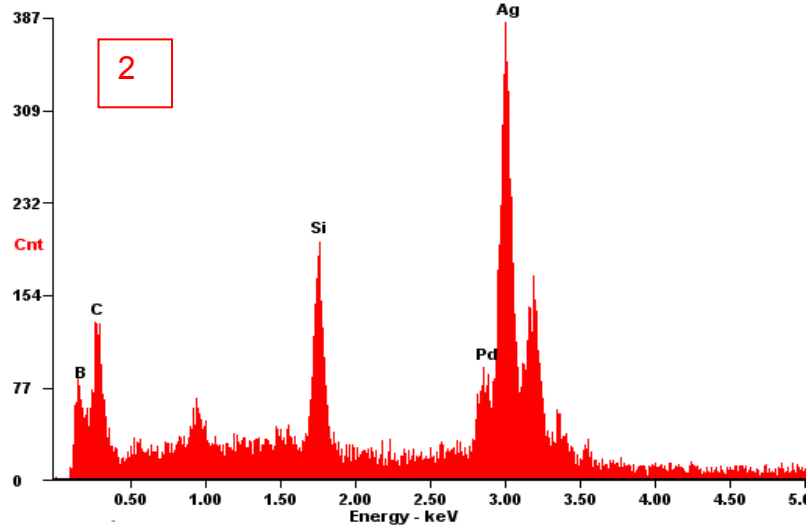
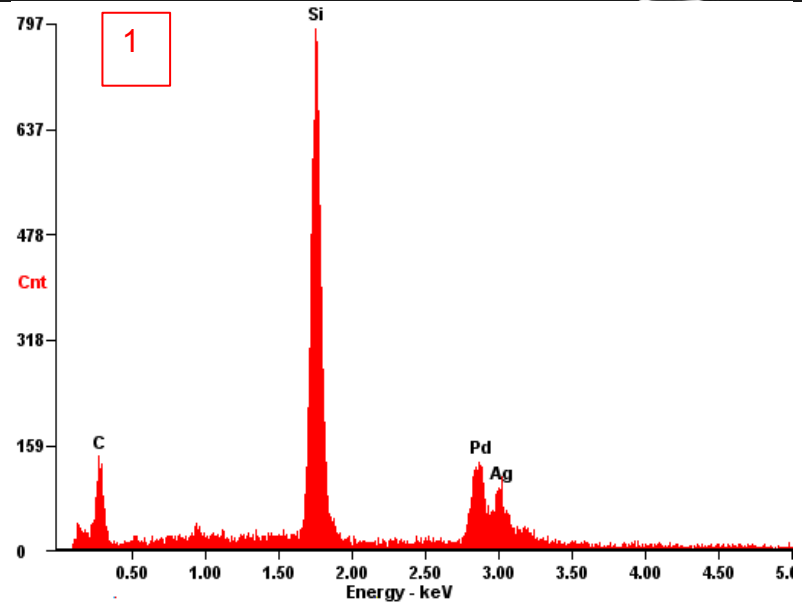
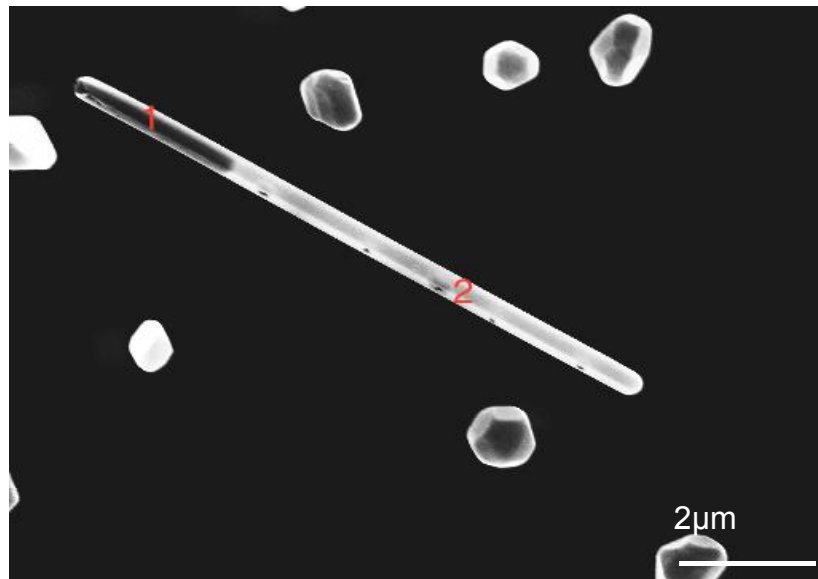


Figure 48: The SEM image and the EDX spectra of the hollowed Ag-Pd nanowhisker

4.6 Characterization of Cu-Ni core-shell nanowhiskers

Cu-Ni core-shell structures were produced employing the same method as in the case of Ag-Au with Cu first grown as template. The typical HRSEM image is shown in Figure 49 and the features which are present in the sample are similar with the other systems; whiskers, islands and platelets. The diameter of the whiskers is approximately 200 nm. The Ni film on the substrate is polycrystalline. The nanowhiskers do not exhibit any compositional contrast along their length, and the corresponding Cu content varies in the range of 70-75 at. %.

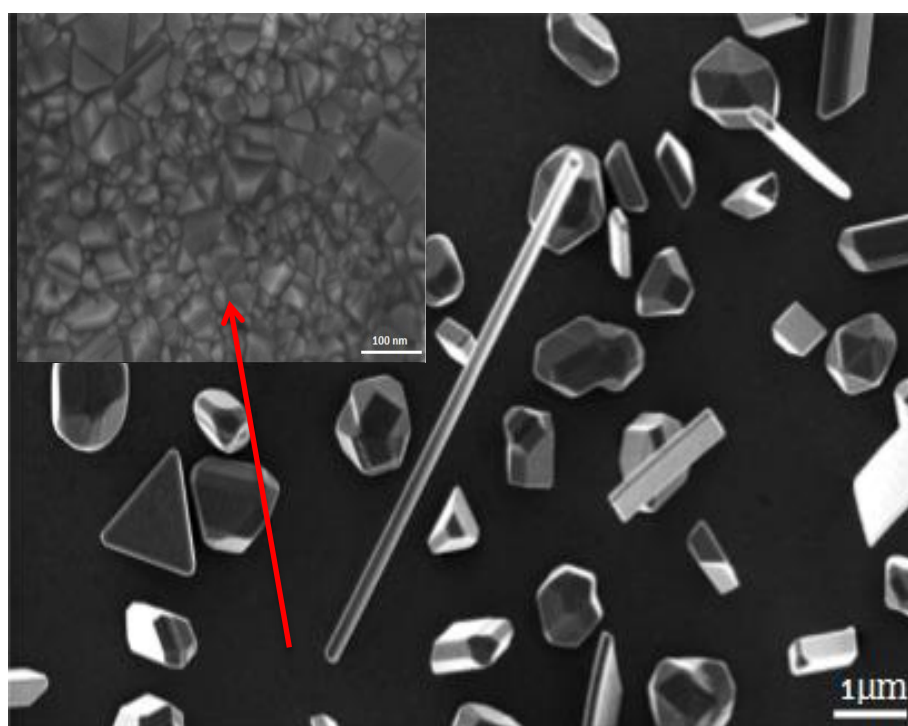


Figure 49: HRSEM image of the Cu-Ni core-shell nanowhiskers and the Ni film

The as-prepared Cu-Ni core-shell nanowhiskers were further characterized by TEM to investigate their morphology and crystal structure. The TEM image of the nanowhisker is shown in the Figure 50. The diameter of the nanowhisker is uniform and is around 200 nm as determined from the image. The nanowhiskers are straight and the surface of the whisker is smooth. The SAED diffraction pattern of the whisker shown in the same figure demonstrates that the nanowhiskers have a single crystalline structure corresponding to fcc Cu and Ni in [111] zone axis.

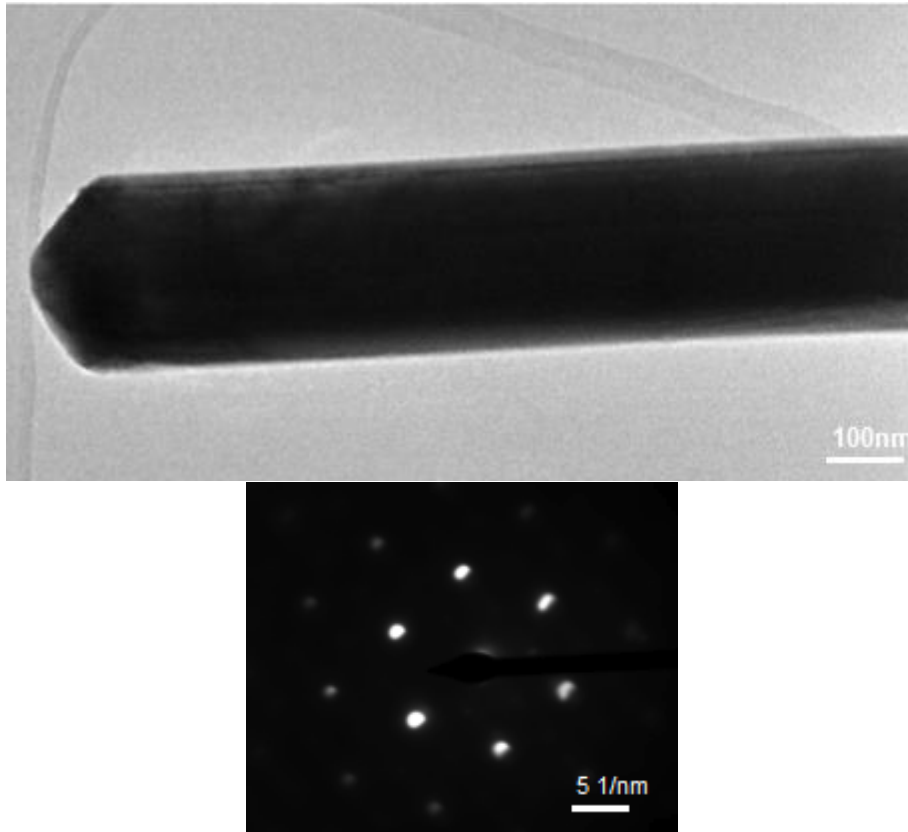


Figure 50: TEM image and the SAED diffraction pattern of the Cu-Ni core-shell nanowhisker

The Cu-Ni core-shell nanowhiskers were annealed at different temperatures in order to obtain Ni nanotubes. In spite of the similarity of microstructure of the Cu-Ni core-shell nanowhiskers and the other studied core-shell nanowhiskers, the hollowing was not observed.

Typical HRSEM image of the nanowhisker annealed at 375°C for 120 min is shown Figure 51. No contrast difference along the whisker could be observed. The Cu contents in the whisker were determined from the EDS spectra acquired at 12 kV. There is no significant decrease of the Cu content after the annealing.

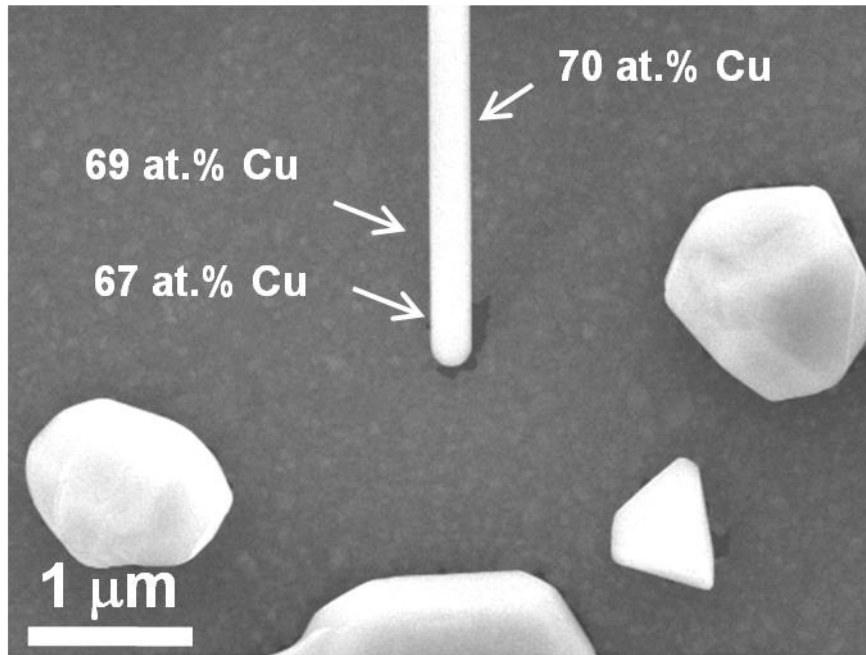


Figure 51: The HRSEM image of annealed Cu-Ni core-shell nanowhisker

The composition of the polycrystalline film in the close vicinity of the whisker was determined from the EDX analysis in 4 different samples; an as grown one and three samples which were annealed at different temperatures. The EDX spectra were acquired at 12 keV and 3 keV, and the corresponding data are shown in the Table 1.

Table 1: Experimental Cu K-ratios for as-grown and differently annealed samples acquired at 3 and 12 keV. K ratios were calculated as a ratio of measured intensities of Cu L_{α} signal from the studied sample and the Cu bulk standard.

Sample	$k_{\text{ratio}}^{\text{-Cu}}$	$k_{\text{ratio}}^{\text{-Cu}}$
	at 3 KV	at 12 KV
As-grown	not detected	0.009±0.001
350°C-30m	0.04 ± 0.01	0.007 ± 0.001
375°C-15 m	0.66 ± 0.06	0.009 ± 0.001
375°C-120 m	0.96 ± 0.11	0.011 ± 0.001

The measurement performed on as grown sample yielded different results for the different accelerating voltages used. The Cu signal can be detected during the measurement at 12 keV, but not at 3 keV. The interaction volume of the incident beam in EDX is an important parameter. When the e-beam is accelerated towards to the sample, the electrons strike the specimen, penetrate inside and interact both

elastically and inelastically. They form an interaction volume from which some information emerges as it is described in 3.4.1. This interaction volume gets increased with increasing acceleration voltage. Therefore, getting Cu signals at 12 keV but not at 3 keV demonstrates that the interface between Ni and the substrate is enriched in Cu. This is due to the deposition parameters during MBE Cu deposition. The substrate temperature is probably not high enough for the surface diffusion. According to the explanations in section 2.1, the substrate temperature should be $0.65T_m$. This yields around 700 °C for Cu. Since the actual deposition temperature is lower than that, the adatoms might be stuck at their arrival site on the substrate because of the low diffusivity. Therefore, Cu is present underneath the Ni layer. Changing the deposition parameter could prevent this, but we haven't tried due to the time limitation.

In the annealed samples, the Cu signal acquired at 3 keV has increased. The Cu signal was increasing with increasing temperature or increasing annealing time for the same temperature. This increase of Cu signal indicates the diffusion of Cu into the upper Ni layer during the thermal treatment.

No hollowing of the Cu-Ni nanowiskers was observed after annealing at the temperature of 375 °C and annealing times ranging from 15 to 120 min. The lack of hollowing in the Cu-Ni system is related to the presence of Cu at the Ni film-substrate interface. Annealing of such bi-layer film results in Cu diffusion along the grain boundaries of the Ni film and their saturation with Cu. This Cu enrichment prevents the possible hollowing of Cu-Ni nanowiskers, since the grain boundaries in Ni layer become saturated with Cu before any Cu atoms from the whisker core can arrive there. This, according to our hollowing model, means that the entropy related driving force for hollowing is missing, and the process does not occur.

5 CONCLUSIONS

The Au, Co and Pd nanotubes were successfully produced through the fabrication of metal (Ag-Au, Ag-Co and Ag-Pd) core-shell nanowhiskers. The core-shell nanowhiskers on the Si/SiO₂/Si₃N₄ substrate coated by 30 nm amorphous C were grown by employing the molecular beam epitaxy deposition technique. The effect of the deposition parameter on the whisker growth was explored.

The core-shell nanowhiskers were characterized by transmission and scanning electron microscopies. The characterization of the samples showed that the synthesized Ag nanowhiskers were perfectly single crystalline and the metal shells on the whiskers (Au, Pd and Co) have grown epitaxially. Despite the large lattice mismatch between the Ag and Co, the epitaxial growth of Co on the Ag was also confirmed.

The metal film on top of the C layer for Ag-Au, Ag-Co and Ag-Pd systems were characterized by EDX and it was observed that the films is only composed of the shell metal. There was no Ag signals acquired from the film and the film was polycrystalline.

The core-shell nanowhiskers (Ag-Au, Ag-Co and Ag-Pd) were partly or fully hollowed after annealing at a temperature at which the short-circuit diffusion of the core material is activated. The annealing temperature resulting in hollowing for Ag-Au and Ag-Pd was 170 °C and 350 °C for Ag-Co. The nanotubes were characterized by SEM and TEM.

A kinetic study of the hollowing process in the Ag-Au system was performed by using 23 nanowhisiker. The Ag-Au core-shell nanowhiskers were annealed at 170 °C for annealing times ranging from 5 to 30 min. After the annealing, Ag enrichment was observed in the Au film in the vicinity of hollowed nanowhiskers. The Ag diffusion into the Au films was also confirmed by the changing grain size in Au film. The grains in the area close to the whisker root showed comparable size to that of as-deposited Au film, while the grains in thin Au film outside of this zone significantly increased in size. The cross-sectional TEM studies revealed a weaker enrichment in Ag at the Au-carbon interface and on the Au surface. This indicates Ag diffusion

along the Au-carbon interface and on the Au surface. An inverse relationship between the hollowing rate and the internal radius of the hollow nanowhiskers was established.

The Cu-Ni core-shell nanowhiskers were also successfully fabricated on the Si/SiO₂/Si₃N₄ substrate coated by 30 nm amorphous C by molecular beam epitaxy. The epitaxial growth of Ni on the single crystalline Cu was also achieved. However, the hollowing for the Cu-Ni core-shell nanowhiskers could not be observed. This was correlated with the presence of Cu at the Ni film-substrate interface in the as-grown samples.

In summary, we demonstrated that metal nanotubes (Au, Pd, and Co) could be synthesized from the Ag core-shell nanowhisker by draining the Ag atoms from the core into the solid solution in the grain boundaries and on the surface of polycrystalline thin film. This process is controlled by several types of short-circuit diffusion. It was proven that the formation of two-dimensional GB phase provided the driving force for the hollowing process.

REFERENCES

- [1] D.B. Harden, D. Whitehouse, K.S. Painter, H. Hellenkemper, *Glass of the Caesars*, Olivetti, 1987.
- [2] S. Iijima, Helical microtubules of graphitic carbon, *nature*, 354 (1991) 56-58.
- [3] J. Guo, X. Zhang, T. Zhang, T. Zhou, X. Zhang, Z. Quan, Self-template synthesis of magnetic cobalt nanotube based on Kirkendall effect, *Materials Letters*, 141 (2015) 288-290.
- [4] H. Hu, Z. Jiao, J. Ye, G. Lu, Y. Bi, Highly efficient hydrogen production from alkaline aldehyde solutions facilitated by palladium nanotubes, *Nano Energy*, 8 (2014) 103-109.
- [5] J.-J. Feng, D.-L. Zhou, H.-X. Xi, J.-R. Chen, A.-J. Wang, Facile synthesis of porous worm-like Pd nanotubes with high electrocatalytic activity and stability towards ethylene glycol oxidation, *Nanoscale*, 5 (2013) 6754-6757.
- [6] C.R. Bridges, T.B. Schon, P.M. DiCarmine, D.S. Seferos, Template Directed Synthesis of Plasmonic Gold Nanotubes with Tunable IR Absorbance, *Journal of visualized experiments: JoVE*, (2013).
- [7] W. Hendren, A. Murphy, P. Evans, D. O'Connor, G. Wurtz, A. Zayats, R. Atkinson, R. Pollard, Fabrication and optical properties of gold nanotube arrays, *Journal of Physics: Condensed Matter*, 20 (2008) 362203.
- [8] T. Narayanan, M. Shaijumon, P. Ajayan, M. Anantharaman, Synthesis of high coercivity cobalt nanotubes with acetate precursors and elucidation of the mechanism of growth, *The Journal of Physical Chemistry C*, 112 (2008) 14281-14285.
- [9] C.R. Bridges, P.M. DiCarmine, A. Fokina, D. Huesmann, D.S. Seferos, Synthesis of gold nanotubes with variable wall thicknesses, *Journal of Materials Chemistry A*, 1 (2013) 1127-1133.
- [10] K. An, T. Hyeon, Synthesis and biomedical applications of hollow nanostructures, *Nano Today*, 4 (2009) 359-373.
- [11] X. Huang, I.H. El-Sayed, W. Qian, M.A. El-Sayed, Cancer cell imaging and photothermal therapy in the near-infrared region by using gold nanorods, *Journal of the American Chemical Society*, 128 (2006) 2115-2120.
- [12] K.K. Nanda, F.E. Krus, H. Fissan, Energy levels in embedded semiconductor nanoparticles and nanowires, *Nano Letters*, 1 (2001) 605-611.
- [13] Y. Yin, R.M. Rioux, C.K. Erdonmez, S. Hughes, G.A. Somorjai, A.P. Alivisatos, Formation of Hollow Nanocrystals Through the Nanoscale Kirkendall Effect, *Science*, 304 (2004) 711-714.
- [14] K. Tu, U. Gösele, Hollow nanostructures based on the Kirkendall effect: design and stability considerations, *Applied Physics Letters*, 86 (2005) 093111.
- [15] Z. TV., Thermodynamics and Multiscale Modeling of Diffusion Processes in Multiphase Nanosystems, D.Sc. Thesis, Cherkassy, Ukraine, (2014).
- [16] A. Gusak, K. Tu, Interaction between the Kirkendall effect and the inverse Kirkendall effect in nanoscale particles, *Acta Materialia*, 57 (2009) 3367-3373.
- [17] G. Richter, Fabrication of freestanding gold nanotubes, *Scripta Materialia*, 63 (2010) 933-936.
- [18] H. Tanaka, *Handbook of Crystal Growth: Thin Films and Epitaxy*, Elsevier, 2014.
- [19] M. Einollahzadeh-Samadi, R. Dariani, Effect of substrate temperature and deposition rate on the morphology and optical properties of Ti films, *Applied Surface Science*, 280 (2013) 263-267.
- [20] C. Bishop, *Vacuum deposition onto webs, films and foils*, William Andrew, 2011.

- [21] M. Ohring, *Materials science of thin films*, Academic press, 2001.
- [22] D. Mattox, Particle bombardment effects on thin- film deposition: A review, *Journal of Vacuum Science & Technology A*, 7 (1989) 1105-1114.
- [23] A. Subramaniam, Critical thickness of equilibrium epitaxial thin films using finite element method, *Journal of Applied Physics*, 95 (2004) 8472-8474.
- [24] X. Tian, J. Cui, C. Zhang, Z. Ma, R. Wan, Q. Zhang, Investigations on the deformation mechanisms of single-crystalline Cu nanowires under bending and torsion, *Computational Materials Science*, 83 (2014) 250-254.
- [25] L. Kraus, A. Lynnyk, D. Azamat, J. Drahoukoupil, J. Kopeček, M. Rameš, Multi-peak ferromagnetic resonance in Co nanowires array, *Journal of Magnetism and Magnetic Materials*, 421 (2017) 241-249.
- [26] H. Ditlbacher, A. Hohenau, D. Wagner, U. Kreibig, M. Rogers, F. Hofer, F.R. Aussenegg, J.R. Krenn, Silver nanowires as surface plasmon resonators, *Physical review letters*, 95 (2005) 257403.
- [27] G. Sears, Mercury whiskers, *Acta metallurgica*, 1 (1953) 457-459.
- [28] F. Frank, F.F. Disc, *Faraday Soc.*, 5 (1949), *Disc. Faraday Soc.*, 5 (1949) 67.
- [29] W.-K. Burton, N. Cabrera, F. Frank, The growth of crystals and the equilibrium structure of their surfaces, *Philosophical Transactions of the Royal Society of London A: Mathematical, Physical and Engineering Sciences*, 243 (1951) 299-358.
- [30] R. Wagner, W. Ellis, Vapor- liquid- solid mechanism of single crystal growth, *Applied Physics Letters*, 4 (1964) 89-90.
- [31] G. Sears, A mechanism of whisker growth, *Acta metallurgica*, 3 (1955) 367-369.
- [32] S.S. Brenner, The growth of whiskers by the reduction of metal salts, *Acta metallurgica*, 4 (1956) 62-74.
- [33] R. Doremus, B. Roberts, D. Turnbull, *Growth and perfection of crystals*, (1958).
- [34] M. Hasan, M.F. Huq, Z.H. Mahmood, A review on electronic and optical properties of silicon nanowire and its different growth techniques, *SpringerPlus*, 2 (2013) 1.
- [35] G. Richter, K. Hillerich, D.S. Gianola, R. Monig, O. Kraft, C.A. Volkert, Ultrahigh strength single crystalline nanowhiskers grown by physical vapor deposition, *Nano Letters*, 9 (2009) 3048-3052.
- [36] V. Ruth, J. Hirth, Kinetics of Diffusion- Controlled Whisker Growth, *The Journal of Chemical Physics*, 41 (1964) 3139-3149.
- [37] M. Schamel, C. Schopf, D. Linsler, S.T. Haag, L. Hofacker, C. Kappel, H.P. Strunk, G. Richter, The filamentary growth of metals, *International Journal of Materials Research*, 102 (2011) 828-836.
- [38] K.N. Tu, Interdiffusion in Thin Films, *Annual Review of Materials Science*, 15 (1985) 147-176.
- [39] W.C. Roberts-Austen, Bakerian Lecture: On the Diffusion of Metals, *Philosophical Transactions of the Royal Society of London. Series A, Containing Papers of a Mathematical or Physical Character*, 187 (1896) 383-415.
- [40] H. Nakajima, The discovery and acceptance of the Kirkendall Effect: The result of a short research career, *JOM*, 49 (1997) 15-19.
- [41] E. Kirkendall, Diffusion of zinc in alpha brass, *Aime Trans*, 147 (1942) 104-109.
- [42] A.-A. El Mel, R. Nakamura, C. Bittencourt, The Kirkendall effect and nanoscience: hollow nanospheres and nanotubes, *Beilstein journal of nanotechnology*, 6 (2015) 1348-1361.
- [43] R. Nakamura, J.-G. Lee, H. Mori, H. Nakajima, Oxidation behaviour of Ni nanoparticles and formation process of hollow NiO, *Philosophical Magazine*, 88 (2008) 257-264.

- [44] B.D. Anderson, J.B. Tracy, Nanoparticle conversion chemistry: Kirkendall effect, galvanic exchange, and anion exchange, *Nanoscale*, 6 (2014) 12195-12216.
- [45] J.G. Railsback, A.C. Johnston-Peck, J. Wang, J.B. Tracy, Size-dependent nanoscale Kirkendall effect during the oxidation of nickel nanoparticles, *ACS nano*, 4 (2010) 1913-1920.
- [46] K.-Y. Niu, J. Park, H. Zheng, A.P. Alivisatos, Revealing bismuth oxide hollow nanoparticle formation by the Kirkendall effect, *Nano letters*, 13 (2013) 5715-5719.
- [47] Q. Li, R.M. Penner, Photoconductive cadmium sulfide hemicylindrical shell nanowire ensembles, *Nano Letters*, 5 (2005) 1720-1725.
- [48] M. Knez, R. Scholz, K. Nielsch, E. Pippel, D. Hesse, M. Zacharias, U. Gösele, Monocrystalline spinel nanotube fabrication based on the Kirkendall effect, *Nature materials*, 5 (2006) 627-631.
- [49] G. Glodán, C. Cserhádi, I. Beszedá, D.L. Beke, Production of hollow hemisphere shells by pure Kirkendall porosity formation in Au/Ag system, *Applied Physics Letters*, 97 (2010) 113109.
- [50] E. González, J. Arbiol, V.F. Puntes, Carving at the nanoscale: sequential galvanic exchange and Kirkendall growth at room temperature, *Science*, 334 (2011) 1377-1380.
- [51] A. Gusak, T. Zaporozhets, K. Tu, U. Gösele, Kinetic analysis of the instability of hollow nanoparticles, *Philosophical Magazine*, 85 (2005) 4445-4464.
- [52] M. Faraday, The Bakerian lecture: experimental relations of gold (and other metals) to light, *Philosophical Transactions of the Royal Society of London*, 147 (1857) 145-181.
- [53] C. Castro, R. Sanjines, C. Pulgarin, P. Osorio, S.A. Giraldo, J. Kiwi, Structure-reactivity relations for DC-magnetron sputtered Cu-layers during E. coli inactivation in the dark and under light, *Journal of Photochemistry and Photobiology*, 216 (2010) 295-302.
- [54] P. Kelly, R. Arnell, Magnetron sputtering: a review of recent developments and applications, *Vacuum*, 56 (2000) 159-172.
- [55] B. Gaedike, BSc Thesis, Mikrostruktur von Kohlenstoffschichten und Wachstum von Kupferwhiskern, University of Stuttgart, (2012).
- [56] B.A. Joyce, R.R. Bradley, A study of nucleation in chemically grown epitaxial silicon films using molecular beam techniques I.—experimental methods, *Philosophical Magazine*, 14 (1966) 289-299.
- [57] S. Franchi, Molecular beam epitaxy: fundamental, historical background and future prospects, *Molecular Beam Epitaxy From Research to Mass Production*, Elsevier Science, Amsterdam, Oxford, (2013) 1-46.
- [58] G. Bauer, G. Springholz, Molecular beam epitaxy—aspects and applications, *Vacuum*, 43 (1992) 357-365.
- [59] <https://www.purdue.edu/ehps/rem/rs/sem.htm>, accessed on September 2016.
- [60] <https://www2.warwick.ac.uk/fac/sci/physics/current/postgraduate/regs/mpags/ex5/techniques/structural/tem/>, accessed on September 2016.
- [61] D.B. Williams, C.B. Carter, The transmission electron microscope, in: *Transmission electron microscopy*, Springer Us, 1996, pp. 3-17.
- [62] F.-R. Fan, D.-Y. Liu, Y.-F. Wu, S. Duan, Z.-X. Xie, Z.-Y. Jiang, Z.-Q. Tian, Epitaxial growth of heterogeneous metal nanocrystals: from gold nano-octahedra to palladium and silver nanocubes, *Journal of the American Chemical Society*, 130 (2008) 6949-6951.

- [63] S. Baylan, G. Richter, M. Beregovsky, D. Amram, E. Rabkin, The kinetics of hollowing of Ag–Au core–shell nanowhiskers controlled by short-circuit diffusion, *Acta Materialia*, 82 (2015) 145-154.
- [64] I. Karakaya, W.T. Thompson, The Ag–C (Silver-Carbon) system, *Bulletin of Alloy Phase Diagrams*, 9 (1988) 226-227.
- [65] L.G. Harrison, Influence of dislocations on diffusion kinetics in solids with particular reference to the alkali halides, *Transactions of the Faraday Society*, 57 (1961) 1191-1199.
- [66] J.W. Cahn, The impurity-drag effect in grain boundary motion, *Acta Metallurgica*, 10 (1962) 789-798.
- [67] G. Gottstein, L. Shvindlerman, *Grain Boundary Migration in Metals: Thermodynamics, Kinetics, Applications* (FL: CRC), (1999).
- [68] I. Kaur, Y. Mishin, W. Gust, *Fundamentals of grain and interphase boundary diffusion*, John Wiley, 1995.
- [69] W.C. Carter, A.R. Roosen, J.W. Cahn, J.E. Taylor, Shape evolution by surface diffusion and surface attachment limited kinetics on completely faceted surfaces, *Acta metallurgica et materialia*, 43 (1995) 4309-4323.
- [70] L. Klinger, E. Rabkin, Effects of Surface Anisotropy on Grain Boundary Grooving, *Interface Science*, 9 (2001) 55-63.
- [71] D. Udler, D. Seidman, Grain boundary and surface energies of fcc metals, *Physical Review B*, 54 (1996) R11133.
- [72] A.R. Miedema, F.J.A. den Broeder, ON THE INTERFACIAL ENERGY IN SOLID-LIQUID AND SOLID-SOLID METAL COMBINATIONS, *Zeitschrift fuer Metallkunde/Materials Research and Advanced Techniques*, 70 (1979) 14-20.
- [73] H.P. Bonzel, M. Nowicki, Absolute surface free energies of perfect low-index orientations of metals and semiconductors, *Physical Review B*, 70 (2004) 245430.
- [74] H.R. Gong, The work function and electronic structure of coherent Ag–Au interfaces, *Solid State Communications*, 149 (2009) 2143-2145.
- [75] S. Klotsman, N. Arkhipova, A. Timofeev, I.S. Trakhtenberg, Diffusion of Silver in Polycrystalline Gold, *PHYS METALS METALLOGR*, 20 (1965) 70-75.
- [76] D. Gan, P.S. Ho, Y. Pang, R. Huang, J. Leu, J. Maiz, T. Scherban, Effect of passivation on stress relaxation in electroplated copper films, *Journal of Materials Research*, 21 (2006) 1512-1518.
- [77] D. Amram, L. Klinger, N. Gazit, H. Gluska, E. Rabkin, Grain boundary grooving in thin films revisited: The role of interface diffusion, *Acta Materialia*, 69 (2014) 386-396.
- [78] H.S. Carslaw, J.C. Jaeger, *Conduction of heat in solids*, Oxford: Clarendon Press, 1959, 2nd ed., (1959).
- [79] Y. Yang, F. Güder, M. Zacharias, Diffusion-Induced Void Evolution in Core–Shell Nanowires: Elaborated View on the Nanoscale Kirkendall Effect, *Israel Journal of Chemistry*, 50 (2010) 439-448.
- [80] L. Klinger, E. Rabkin, Theory of the Kirkendall effect during grain boundary interdiffusion, *Acta Materialia*, 59 (2011) 1389-1399.
- [81] L. Klinger, E. Rabkin, Grain boundary interdiffusion and stresses in thin polycrystalline films, *Journal of Materials Science*, 46 (2011) 4343-4348.
- [82] H. Gao, L. Zhang, W.D. Nix, C.V. Thompson, E. Arzt, Crack-like grain-boundary diffusion wedges in thin metal films, *Acta Materialia*, 47 (1999) 2865-2878.
- [83] D. Bufford, H. Wang, X. Zhang, High strength, epitaxial nanotwinned Ag films, *Acta Materialia*, 59 (2011) 93-101.

- [84] F. LeGoues, M. Liehr, M. Renier, W. Krakow, Microstructure of epitaxial Ag/Si (111) and Ag/Si (100) interfaces, *Philosophical Magazine B*, 57 (1988) 179-189.
- [85] Y. Fukano, Particles of γ -iron quenched at room temperature, *Japanese Journal of Applied Physics*, 13 (1974) 1001.
- [86] E. Owen, D.M. Jones, Effect of grain size on the crystal structure of cobalt, *Proceedings of the Physical Society. Section B*, 67 (1954) 456.
- [87] E. Anno, Optical absorption of fcc Co particles: Properties of conduction electrons of fcc Co, *Physical Review B*, 50 (1994) 17502.
- [88] L. Vitos, A. Ruban, H.L. Skriver, J. Kollar, The surface energy of metals, *Surface Science*, 411 (1998) 186-202.
- [89] Y. Lee, I. Choi, K. Lim, K. Jeong, C. Whang, H. Choe, Y. Lee, Grain boundary diffusion effects on the sputter depth profiles of Co–Ag bilayers, *Journal of applied physics*, 79 (1996) 3534-3540.
- [90] C. Zimmermann, M. Yeadon, K. Nordlund, J. Gibson, R. Averback, U. Herr, K. Samwer, Burrowing of Co nanoparticles on clean Cu and Ag surfaces, *Physical review letters*, 83 (1999) 1163.

ABBREVIATION AND SYMBOLS

List of Most Used Abbreviations

NT: Nanotube

NW: Nanowhisker

MBE: Molecular beam epitaxy

SEM: Scanning electron microscope

TEM: Transmission electron microscope

HRSEM: High resolution scanning electron microscope

EDX: Eenergy-dispersive X-ray spectrometer

GB: Grain boundary

VLS: Vapor liquid solid model

UHV: Ultra high vacuum

STEM: Scanning transmission electron microscope

PVD: Physical vapor deposition

CVD: Chemical vapor deposition

AFM: Atomic force microscopy

RHEED: Reflection high electron diffraction

QMS: Quadrupole mass spectrometry

SE: Secondary electron

FIB: Focused ion beam

SAED: Selected area electron diffraction

fcc: Face centered cubic

hcp: Hexagonal close packed

List of of Most Used Symbols

τ_s : The residence time of the adatom on the surface

ν : Vibrational frequency of the adatom

E_{des} : Desorption energy

X : Diffusion length

R : Depositon rate

D_s : Surface diffusion coefficient

E_s : Activation energy of surface diffusion

a_0 : Distance of a jump

k : Boltzman constant
 T : Substrate temperature
 T_m : Melting point
 σ_F : Surface energy of the droplet
 σ_s : Surface energy of the substrate
 σ_{FS} : Interface energy between the droplet and the substrate
 f_m : Lattice mismatch between the film and the substrate
 a_f : Lattice constant of the film
 a_{sub} : Lattice constant of the substrate
 D_A^1 : Diffusion coefficient of the material A
 D_B^1 : Diffusion coefficient of the material B
 $J_{A/B}$: Flux of the atoms from A to B
 $J_{B/A}$: Flux of the atoms from B to A
 L : True length of the hollowed part of the nanowhisker
 R_0 : Radius of the fine grain zone
 μ_1 : Chemical potential of the Ag atoms located on the meniscus
 μ_{Ag}^0 : Standard chemical potential of Ag in the bulk
 γ_{Au} : Surface energy of Au
 γ_{int} : Interface energy of Au-Ag
 Ω : Atomic volume of Ag
 r : Internal radius of the Au nanotube
 μ_2 : Chemical potential of Ag atoms at the Au-carbon interface
 $\mu_{b,Ag}^0$: Standard chemical potential of Ag in the Au GB
 c_b : Concentration of Ag atoms in the GB
 ω_{Ag} : The molar area of Ag atoms in the GB
 u : Height of the hollowed part of the nanowhisker
 δ_b : Thickness of the GBs in Au film
 d : Average grain size in Au film
 h : Thickness of the grain
 δ_s : Thickness of the surface segregation layer
 c_s : Ag concentration in the surface segregation layer
 J : Total flux of Ag atoms along the Au-carbon interface
 D_i : Diffusion coefficient of Ag atoms along the Au-carbon interface

δ : Grain boundary width

l : Diffusion distance along the Au-carbon interface

$\gamma_{b,Ag}$: GB energy in pure Ag

$\gamma_{b,Au}$: GB energy in pure Au

$\gamma_{b,alloy}$: Energy of Ag dopes GB between two grains of pure Au

D_{eff} : Effective diffusivity

γ_{Co} : Surface energy of Co

INDEX OF FIGURES

FIGURE 1: THE LYCURGUS CUP MADE BY ROMANS [1].....	1
FIGURE 2: ISLAND GROWTH MODE [21]	7
FIGURE 3: LAYER GROWTH MODE [21]	7
FIGURE 4: STANSKI-KRASTANOV GROWTH MODE [21]	8
FIGURE 5: SCHEMATIC ILLUSTRATION OF THE LIQUID DROP MODEL [22].....	8
FIGURE 6: SCHEMATIC ILLUSTRATION OF THE STRUCTURE DEPENDING ON THE LATTICE PARAMETERS [21].....	10
FIGURE 7: CALCULATION OF THE CRITICAL THICKNESS FOR THE CO/CU SYSTEM BY FEM SIMULATION [23].....	11
FIGURE 8: EMERGING SCREW DISLOCATION PROPOSED BY FRANK [29]	12
FIGURE 9: SCHEMATIC OF THE VLS GROWTH MECHANISM (A) CATALYTIC LIQUID ALLOY (B, C) WHISKER GROWTH [34].....	13
FIGURE 10: SEM IMAGES OF CU NANOWHISKERS. NOMINAL THICKNESSES OF A) 45NM CU AND B) 200 NM CU [35]	14
FIGURE 11: A) DARK-FIELD TEM IMAGE B) ENERGY FILTERED TEM MICROGRAPHS C) THE WHISKER SHOWN IN (B) IS ROTATED BY 30° ALONG THE WHISKER AXIS D) IDEAL WHISKER SHAPE CALCULATED BY CU FREE SURFACE ENERGIES USING THE WULFF PLOT E) CU WHISKER SHAPE MODEL BASED ON WULFF PLOT F) HIGH RESOLUTION TEM IN [111] ZONE AXIS [35]	15
FIGURE 12: ATOMIC DIFFUSION MECHANISM: A) DIRECT EXCHANGE MECHANISM; B) RING MECHANISM; C) VACANCY MECHANISM [40]	16
FIGURE 13: THE INTERFACE BETWEEN THE METALS ACCORDING TO THE KIRKENDALL EFFECT A) BEFORE ANNEALING B) FORMATION OF SMALL VOIDS C) FORMATION OF LARGE VOIDS [42].....	18
FIGURE 14: SCHEMATIC ILLUSTRATION OF MAGNETRON SPUTTERING [53]	22
FIGURE 15: AFM IMAGE OF THE C DEPOSITED SI/SIO ₂ /SI ₃ N ₄ SUBSTRATE	24
FIGURE 16: SCHEMATIC ILLUSTRATION OF AN MBE GROWTH CHAMBER [57].....	25
FIGURE 17: THE SCHEMATIC ILLUSTRATION OF THE FABRICATION PROCESS FOR THE NANOWHISKER GROWTH.....	27
FIGURE 18: SEM IMAGES OF AG NANOWHISKERS PRODUCED AT DIFFERENT TEMPERATURES AND RATES; A) 800°C, 0.25NM/S B) 650°C, 0.05NM/S C) 650°C, 0.25NM/S.....	28
FIGURE 19: SCHEMATIC ILLUSTRATION OF THE FABRICATION PROCESS FOR THE CORE-SHELL NANOWHISKERS	29
FIGURE 20: SCHEMATIC ILLUSTRATION OF SEM [59].....	31
FIGURE 21: THE SIGNALS GENERATED BY ELECTRON SAMPLE INTERACTIONS IN SEM [21]....	32
FIGURE 22: SCHEMATIC ILLUSTRATION OF TEM [60]	33
FIGURE 23: THE SIGNALS GENERATED FROM THE ELECTRON SAMPLE INTERACTIONS [61] ...	34
FIGURE 24: SEM IMAGES OF AG-AU CORE-SHELL NANOWHISKERS	37

FIGURE 25: HRSEM IMAGES OF TWO TYPICAL AG-AU CORE-SHELL NANOWHISKERS WITH THE AVERAGE AG CONTENTS, WHICH WERE DETERMINED FROM EDS SPECTRA.....	38
FIGURE 26: TEM IMAGES AND THE SAED DIFFRACTION PATTERN OF THE AG-AU CORE SHELL NANOWHISKER.....	40
FIGURE 27: EDX SPECTRUM OF THE AG-AU CORE-SHELL NANOWHISKER IN FIGURE 26	41
FIGURE 28: A) HRSEM IMAGE OF THE AG-AU NANOWHISKER AFTER ANNEALING B) THE AG CONTENTS IN THE FILM, DETERMINED FROM THE EDS SPECTRA ACQUIRED AT 10 KV.....	42
FIGURE 29: EDS CONCENTRATION PROFILE OF THE PARTIALLY HOLLOWED NANOWHISKER SHOWN IN.....	43
FIGURE 30: A) HRSEM IMAGE OF AG-AU NANOWHISKER AFTER ANNEALING AT 170°C FOR 30 MIN B) EDS LINE PROFILE TAKEN ALONG THE NANOWHISKER AT 10 KV.....	44
FIGURE 31: A) HRSEM IMAGE OF PARTLY HOLLOWED NANOWHISKER AFTER ANNEALLING AT 170°C FOR 20 MIN, AND THE EDS ELEMENTAL DISTRIBUTION MAPS ACQUIRED WITH B) AUM _{A1} , C) CK _{A1} , AND D) AGL _{A1} X-RAY RADIATION	45
FIGURE 32: A) HRSEM IMAGE AND EDS ELEMENTAL MAPS ACQUIRED WITH B) AUM _{A1} , C) SIK _{A1} , AND D) AGL _{A1} RADIATION FOR THE HOLLOWED SECTION OF THE NANOWHISKER ANNEALED AT 170°C FOR 30 MIN.: 1 – SE (A) AND EDS (B-C) PROJECTION OF THE NANOWHISKER, 2 – SHADOWS OF THE NANOWHISKER FORMED DURING AU DEPOSITION BY MBE, 3 – X-RAYS SHADOWS FORMED DUE TO A NANOWHISKER SHADOWING EFFECT ON THE X RAY RADIATION EMITTED BY THE SUBSTRATE.....	46
FIGURE 33: SCHEMATIC ILLUSTRATING FOR THE CALCULATION OF THE INCLINATION ANGLE, A, OF THE AG-AU NANOWHISKER WITH RESPECT TO THE SURFACE NORMAL BASED ON AUM _{A1} EDS MAPPING: OD IS A PARTIALLY HOLLOW NANOWHISKER WITH THE INCLINATION ANGLE A WITH RESPECT TO THE SURFACE NORMAL AD; OA ITS PROJECTED IMAGE ACQUIRED BY BACKSCATTERED ELECTRONS; OB IS THE NANOWHISKER SHADOW IN AUM _{A1} -RADIATION EMITTED BY THE FILM TOWARDS THE EDS DETECTOR; AB IS A SUBSTRATE PROJECTION OF THE X-RAYS EMITTED FROM THE FILM TOWARDS THE EDS DETECTOR (D).....	47
FIGURE 34: THE DEPENDENCE OF THE LENGTH OF THE HOLLOWED REGION AND THE WHISKER RADIUS OF THE PRODUCT ON ANNEALING TIME.....	48
FIGURE 35: CROSS-SECTIONAL HIGH ANGLE ANNULAR DARK FIELD (HAADF) STEM IMAGE OF THE PARTIALLY HOLLOWED NANOWHISKER AND OF THE NEARBY REGION OF AU THIN FILM.....	49
FIGURE 36: CROSS-SECTIONAL HAADF STEM IMAGE OF THE HOLLOWED NANOWHISKER SHOWN IN FIGURE 35: 1-HOLLOW AG-FREE INTERNAL PART OF THE NANOWHISKER, 2 – AU ALL-AROUND SHELL	50
FIGURE 37: CROSS-SECTIONAL BRIGHT FIELD STEM IMAGE OF THE AU FILM IN THE VICINITY OF THE NANOWHISKER SHOWN IN FIG. 9.....	51

FIGURE 38: DEPTH PROFILES OF $AG_{L_{A1}}$ AND $AU_{L_{A1}}$ INTENSITY RATIOS BASED ON STEM MEASUREMENTS OF THE AU FILM AT THE DISTANCES OF A) 1.5MM, B) 2.5 MM, AND C) 3.5 MM FROM THE NANOWHISKER.....	52
FIGURE 39: SCHEMATIC ILLUSTRATION OF THE AG DIFFUSION FLUXES DURING THE HOLLOWING PROCESS. THE AG ATOMS LEAVE THE MENISCUS OF THE AG CORE, DIFFUSE ALONG THE INTERNAL WALLS OF THE GROWING AU NANOTUBE, THEN DIFFUSE ALONG THE AU-CARBON INTERFACE AND FINALLY ENTER THE GBS IN THE THIN AU FILM. THE GB DIFFUSION OF AG IS ASSISTED BY THE DIFFUSION ALONG THE FILM SURFACE	55
FIGURE 40: SEM IMAGES OF A) AG-CO AND B) AG-PD CORE-SHELL NANOWHISKERS	62
FIGURE 41: TEM IMAGES OF THE AG-CO CORE SHELL NANOWHISKER.....	63
FIGURE 42: THE SAED DIFFRACTION PATTERN AND CORRESPONDING INDEXING OF THE AG-CO CORE-SHELL NANOWHISKER	64
FIGURE 43: EDX SPECTRUM OF AG-CO CORE-SHELL NANOWHISKER.....	64
FIGURE 44: THE TEM IMAGE AND THE DIFFRACTION PATTERN OF THE CO FILM.....	66
FIGURE 45: TEM IMAGES AND THE SAED DIFFRACTION PATTERN OF THE AG-PD CORE SHELL NANOWHISKER.....	67
FIGURE 46: EDX SPECTRUM OF AG-PD CORE-SHELL NANOWHISKER.....	68
FIGURE 47: THE SEM IMAGES OF THE HOLLOWED AG-CO NANOWHISKER.....	69
FIGURE 48: THE SEM IMAGE AND THE EDX SPECTRUMS OF THE HOLLOWED AG-PD NANOWHISKER.....	72
FIGURE 49: HRSEM IMAGE OF THE CU-NI CORE-SHELL NANOWHISKERS AND THE NI FILM.....	73
FIGURE 50: TEM IMAGE AND THE SAED DIFFRACTION PATTERN OF THE CU-NI CORE-SHELL NANOWHISKER.....	74
FIGURE 51: THE HRSEM IMAGE OF ANNEALED CU-NI CORE-SHELL NANOWHISKER.....	75

ACKNOWLEDGEMENTS

I would like to start by expressing my sincere gratitude to Prof. Dr. Guido Schmitz for accepting to be my first supervisor, for his kindness, supports and helps.

Deeply gratitude goes to my direct supervisor Dr. Gunther Richter, with whom I had the pleasure to work every day during my Ph.D. I would like to thank to him for giving me the chance of working in such a great group, for the continuous support of my Ph.D study and related research, for his patience, motivation, and immense knowledge.

Special thanks must go to Prof. Dr. Eugen Rabkin with whom I had the chance of working in this project, for all his help, his precious discussions, and his great hospitality in Israel. His guidance helped me in all the time of research. His constructive suggestions and discussions improved enormously the quality of this dissertation.

I would like to thank Prof. Dr. Peer Fischer accepting of being part of my Ph.D. exam committee.

I gratefully thank to Dr. Michael Beregovsky and Dr. Dor Amram for their precious help, discussions and hospitality in Israel.

I gratefully thank to Ilse Lakemeyer and Reinhart Völker for their enormous technical help and once again to them and to Frank Thiele for their nice daily conversations. I also thank to my colleagues Wenting Huang and Christian Kappel for our discussions and our nice times in the group.

I would like to thank to Ioanis Grigoriadis, Ute Salzberger and Marion Kelsch for their technical help.

I deeply want to thank some of my friends. They became like the family I was missing in Stuttgart. I have all different kind of reasons to thank each of them. Ekin, Umut, Yeliz and Sinem; thank you so much for making my life easier and joyful in Stuttgart.

A special thanks goes to Frances for his patience and continues support.

Last but not the least, I would like to thank to my family for their presence, unconditional love, and great support during the period of my Ph.D and all my life. I wouldn't manage it without them being there for me.

Curriculum Vitae

Name:	Semanur Baylan
Date / place of birth:	22.02.1985 / Kelkit, Turkey
January 2013 - present	Ph.D. Candidate in Chemistry Max Planck Institute for Intelligent Systems, Stuttgart, Germany Thesis: "Diffusion assisted synthesis of metal nanotubes"
September 2012 – December 2012	Visiting Scientist in Max Planck Institute for Intelligent System, StEM, Stuttgart, Germany
September 2010 – July 2012	Teaching Assistant, Department of Physics, Isik University, Istanbul, Turkey
September 2009 – July 2011	MSc in Materials Science & Engineering Istanbul Technical University, Istanbul, Turkey Thesis: "Preparation of $TO_{2-x}N_x$ Nanotube Films by Anodic Oxidation of TiN Coatings "
September 2004 – July 2008	BSc in Physics Istanbul University, Istanbul, Turkey
September 2000 – June 2003	High School Gebze Neset Yalcin High School

Publications

1. Baylan, S., Richter, G. Beregovsky, M. , Amram, D., Rabkin, E. The kinetics of hollowing of Ag-Au core-shell nanowhiskers controlled by short-circuit diffusion. *Acta Materilia*, 2014, 82, 145-154.
2. Ajay Vikram Singh*, Semanur Baylan* (equal contribution), Byung-Wook Park, Gunther Richter, Metin Sitti, Hydrophobic pinning with copper nanowhiskers leads to bactericidal properties, 2017, Plos ONE 12(4):e0175428.